5-2008

Interlaminar Subgrain Refinement in Ultrasonic Consolidation

Kenneth E. Johnson
Olivet Nazarene University, kejohnson@olivet.edu

INTERLAMINAR SUBGRAIN REFINEMENT IN ULTRASONIC CONSOLIDATION

Kenneth Johnson
Loughborough University

PhD. Thesis
February, 2008

Acknowledgements

I would first like to thank Solidica, Inc., for supporting and encouraging the completion of this work through the provision of facilities and finances. I would also like to sincerely thank all of my cross-Atlantic friends and advisors who have made this entire experience both possible, and extremely rewarding. To Dr. Phill Dickens, who painstakingly mentored me through the process and execution of meaningful and quality research. To Rebecca Higginson, whose keen technical insights served as a clarifying force throughout my experimentation.

I would further like to thank both the Wolfson School of Engineering and the Materials Department at Loughborough (IPTME) for the provision of research facilities. I would like to specifically acknowledge the special contributions of Dr. Geoff West, without whom many of the most exciting insights of this research would not have been possible.

Finally, I would like to thank the loving support of my family. With special thanks to my wife Jen who selflessly enabled me to spend extensive amounts of time in England over the past 4 years to complete this dream.

TABLE OF CONTENTS

LIST OF FIGURES

LIST OF TABLES

1. Abstract

This research presents microscopic evidence of dislocation propagation and sub-grain refinement in 3003-T0 aluminium undergoing high frequency fully reversed loading conditions during the Ultrasonic Consolidation process. Dual Beam Focused Ion Beam etching techniques and Transmission Electron Microscopy were used to characterize sub-grain morphology and dislocation structure in regions that were subjected to high levels of multi-axial ultrasonic micro-strain and resultant plastic deformation. This Deformation Affected Zone is characterized by regions of reduced sub-grain sizes that form a gradual transition into larger equiaxed, grains well below the interface.

While ultrasonic welding has been explored for some time, there has been little agreement on the specific softening mechanisms that allow an ultrasonic weld to occur. Usually, the unexplained effect is vaguely referred to as "acoustic softening," or "ultrasonic softening" -- generic terms that do not identify a specific mechanism. This uncertainty has led to many disparate theories as to the specific nature of ultrasonic welding. The presented interface characterization discoveries challenge many of these ideas and prescribes a fundamental operative "ultrasonic softening" mechanism that is similar in character to the Bauschinger Effect.

2. Background

2.1. Metal Additive Manufacturing

Over the past two decades, there has been a flood of innovative fabrication methods developed which, at their root, involve the aggregate layer by layer fabrication of a three dimensional shape. Known synonymously as "additive manufacturing," "solid freeform fabrication," "rapid prototyping," among others, this technology family has seen increased growth and commercial adoption. While initially dominated by the use of polymeric fabrication methods such as Stereolithography and Fused Deposition Modeling, the end of the 1990's saw the rapid emergence of additive metal systems. The following outlines three common metal process segments: Direct Metal Fabrication, Indirect Metal Fabrication, and 3 Dimensional Printing.

- Direct Metal Fabrication (DMF) – These processes (commercialized by Optomec-US, POM-US, MCP/F&S-Germany, EOS – Germany, Trumpf – Germany, National Research Council - Canada, and Concept Laser-Germany) are characterized by the use of a laser, or similar high intensity heating aid, to melt metal (commonly in powder form) within the focal point and subsequent "drawing" of the part. The process proceeds line by line in two dimensions in a raster fashion, and then repeating the process on subsequent layers to create the desired 3D shape. The methods within this family include processes known as direct metal deposition[1], shape deposition manufacturing[2], shape melting[3], three dimensional welding[4], additive electron beam manufacturing[5], additive gas metal arc welding[6], among others. The primary benefits of this approach are that extremely hard metals can be deposited. However, the relatively slow deposition rates, combined with only a near-net shape surface that usually requires additional finishing operations for tooling applications,

has limited their use. In addition to this, with the exception of the EOS system, the DMF processes are line of sight and do not have support material capability (inhibiting the ability of the process to fabricate overhang features.) One unique member of the DMF family is the Fast4M laminate metal fabrication method which bonds entire layers of metal to fabricate a tool or prototype[7]. This method bonds the layers through the use of a molten braze interlayer.

- Indirect Metal Fabrication (IMF) – This process (commercialized by 3D Systems - US) uses a laser to cure a powder, but unlike DMF, the powder is not directly metal, but a polymer coated metal[8]. The part is produced in a stationary bed (as opposed to most DMF approaches where it is sprayed into the focal point of a laser.) The polymer linked metal powders are then sintered as a whole. The bed provides a useful support material structure but many of the parts are porous and materials such as aluminium are very difficult to utilize. This process is useful for certain prototype needs but is not a practical rapid tooling method due to its accuracy limitation and surface porosity.
- 3 Dimensional Printing (3DP)[9] – Licensed from MIT, 3DP by ExOne, is the only manufacturer of this technology for metal. The primary approach is related to the bonding of metal powders by depositing a polymer binder via "inkjet" technology. The binder is then removed and the metal particles are sintered. Due to the relative difficulty in producing high quality metal parts however, the technology has been increasingly used to produce investment sand casting molds.

While several applications exist where these methods solved specific engineering challenges, many have been limited in their ultimate utility due to the inherent challenges of the molten solidification or infiltration stages of their processes. Some of the more common challenges relate to the existence of high levels of porosity and inclusions as well as anisotropic material properties due to process induced surface embrittlement.

Out of these initial developments emerged a new method of non thermal, metallic additive fabrication technology called Ultrasonic Consolidation (UC)[10]. This novel approach, most similar to DMF, leverages solid state welding techniques to eliminate the molten bonding stage entirely and served as the focus for the current research.

2.2. Solid State Welding

The field of solid state welding is broadly represented by a variety of processes which produces bonds effectively at temperatures below the melting point of the base materials being joined, without the addition of any additive filler metal. While in many cases the solid state bonds are driven through the use of pressure, it is not always a requirement. Currently, several prominent processes in the solid state welding category include: cold welding, diffusion welding, explosion welding, forge welding, friction welding, hot pressure welding, roll welding, and ultrasonic welding. Solid state welding falls prominently within the official listing of processes within the American Welding Society (AWS) Master Chart of Welding and Allied Processes (Figure 1). The welding society formulated process definitions from the operational instead of the metallurgical point of view and as a result, they prescribe the significant

elements of operation instead of the specific metallurgical characteristics of the resulting bonds.

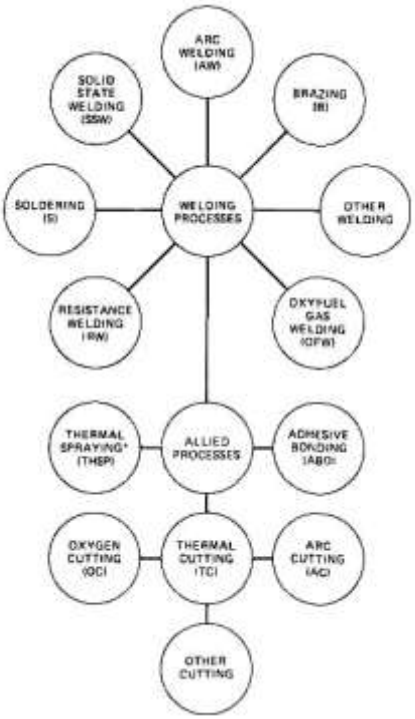

Figure 1 AWS Master Chart of Welding and Allied Processes.[14]

Within the field of solid state welding are many of the oldest, as well as several of the newest welding processes. Solid state welding is highly advantageous for many applications in that it provides true metallic bonds, free from the limitations of the multitude of molten joining processes. Among the key benefits are the limited effects of oxidation during the weld process, the ability to bond dissimilar metals with highly varying thermal and mechanical properties, as well as a frequently superior bond strength compared to those found in traditional weld affected zones. A brief overview of the major solid state welding methods is provided in the following sections[11].

2.2.1. Cold Welding

Cold welding uses extremely high pressure at room temperature to produce metallic bonds between extremely clean interfaces. In many cases, the high pressures necessary can be obtained with simple hand tools when very thin materials are being joined. If thicker sections are to be welded, industrial presses may be utilized to achieve the required contact stresses at the surface. This rapid impact process is particularly suited to common ductile materials such as aluminium and copper.

2.2.2. Diffusion Welding

Diffusion welding is similar to conventional cold welding with the addition of elevated temperatures. Diffusion welding combines the application of pressure with assistance from increased work-piece temperature to produce coalescence of the faying surfaces, that is, the surfaces that are in contact with each other and joined or are about to be joined. The process does not involve microscopic deformation melting or relative motion of the parts. Filler metal may or may not be used to enhance the bond quality.

The process is used for joining refractory metals such as molybdenum, tantalum and tungsten at temperatures that do not affect their metallurgical properties. Dissimilar joining is also possible. Heating is usually accomplished by resistance, induction, or a furnace, with process temperatures at normally half of the material melting temperature. Similar to conventional cold welding, close tolerances in joint preparation are required and a vacuum or inert atmosphere is used. The process is considered diffusion brazing when a layer of filler material is placed between the faying surfaces.

2.2.3. Explosion Welding

Explosion welding is a process in which bonding is accomplished by the initiation of high-velocity movement between the parts to be joined by a controlled detonation. Heat is not applied in making an explosion weld, however, the metal at the interface is molten during welding as a result of the shock wave associated with impact and from the energy expended in collision. Plastic deformation also occurs and is critical to the creation of a quality weld as the area of contact between the mating members increases greatly.

Explosion welding has been shown to create a strong weld between almost all metals, including dissimilar metals that are not readily weldable by arc processes. Of equal importance, the weld does not greatly disturb all of the effects of cold work or other forms of mechanical or thermal treatment that were made prior to the process. As a result, the strength of the weld joint is equal to or greater than the strength of the weaker of the two metals joined. However, this process is limited by the required part geometries and process conditions.

2.2.4. Forge Welding

Forge welding, known in past centuries as hammer welding, produces coalescence of metals by heating them in a forge and by applying pressure or blows sufficient to cause permanent deformation at the interface. This process is of minor industrial significance today.

2.2.5. Friction Welding

Friction welding produces coalescence of materials by the heat obtained from mechanically-induced sliding motion between rubbing surfaces as the work parts are held together under pressure. This process usually involves rotating one part against

another to generate frictional heat at the junction. When a suitable high temperature has been reached, rotational motion ceases and additional pressure is applied and coalescence occurs. A rapidly expanding branch of friction welding is known as friction stir welding in which the frictional motion is induced by a rotating pin that is forced between two stationary surfaces to be joined.

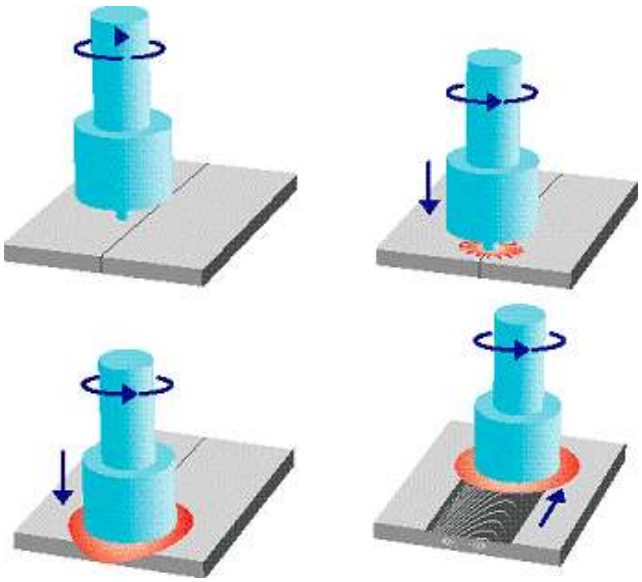

Figure 2 Schematic drawing of friction stir welding.

2.2.6. Hot Pressure Welding

In this process bonding occurs at the interface between the parts to be joined as a result of the direct application of pressure and heat which is accompanied by noticeable deformation. The high degree of deformation differentiates this process from diffusion welding where there is no macro deformation and extremely tight interface tolerances are maintained. The local contact forces crack the surface oxide film and increases the areas of clean metal in contact. Welding this metal to the clean metal of the abutting part is accomplished by diffusion across the interface so that coalescence of the faying surface occurs. A variation is the hot isostatic pressure

welding method where the pressure is applied by means of a hot inert gas in a pressure vessel.

2.2.7. Roll Welding

Roll welding produces coalescence of metals by heating and by applying pressure with rolls sufficient to cause deformation at the faying surfaces. This process is similar to forge welding except that pressure is applied by means of rollers rather than hammer blows. Coalescence occurs at the interface between the two parts by means of diffusion at the faying surfaces.

2.2.8. Ultrasonic Welding

Ultrasonic welding produces coalescence by the local application of high-frequency vibratory energy as the work parts are held together under pressure. Welding occurs when the ultrasonic tip or sonotrode (the energy coupling device) is clamped against the work pieces and is made to oscillate in a plane parallel to the weld interface (or normal to the interface in plastic ultrasonic welding). The combined clamping pressure (~500N) and oscillating motion (~10μm amplitude) introduce dynamic stresses in the base metal which produces interlaminar deformations which are believed to create a moderate temperature rise in the base metal at the weld zone. This coupled with the clamping pressure and the potential break-up of the surface oxides, provides for coalescence across the interface to produce the weld. The main parameters used within ultrasonic welding processes are as follows:

- Amplitude: Peak to peak vibration amplitude – typically 5-30μm.
- Frequency: The set operating frequency of any ultrasonic welding system. Typical systems operate at 20 kHz, 40 kHz, and 60 kHz.

- Clamping Force: The normal force added to the sonotrode to aid in welding. Forces can range from a few Newton's to several kilo-Newtons.
- Dwell Time: Time of welding generally in the millisecond regime.
- Speed: In Ultrasonic Consolidation this is the rolling speed of the sonotrode
- Power: The power sent to the transducer necessary to vibrate the sonotrode at the given amplitude setting (~2.0-4.0 kW)..

2.3. General Ultrasonics and Ultrasonic Joining Research

Ultrasonics research began over 150 years ago as scientist Rudolph Koenig attempted to discover the highest pitch sound that humans could hear. This pursuit quickly led to the creation of sonic and ultrasonic devices of increasing magnitude and complexity by a wide range of researchers. Over time (and driven significantly by military applications for World War I and World War II,) implementations of ultrasonics continued to develop. Ultrasonic engineering in general has been loosely categorized into higher power industrial applications that accomplish some form of mechanical work (such as in the UC process) and lower power applications that are commonly used for applications such as non destructive inspection[12].

As late as 1965 it was still thought that metal could only be ultrasonically joined if one of the members to be joined was a wire[13]. Since that time there has been a relative proliferation of ultrasonic metal welding devices that are typically related to spot, or seam welding. Currently, the American Welding Society[14] publishes the matrix in Figure 3 to highlight the known materials that can be joined via ultrasonic methods.

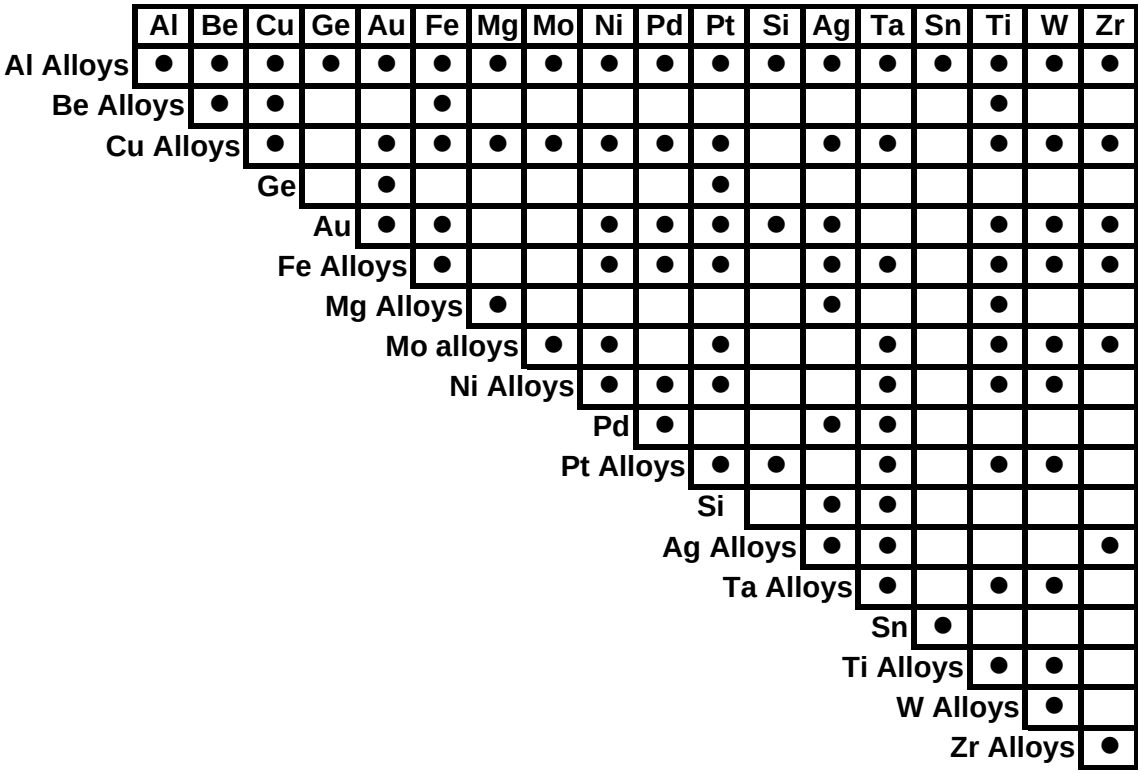

Figure 3 Ultrasonic joining material compatibility matrix[14].

At its earliest, the exact mechanisms of ultrasonic metallic bonding were not well understood. Over time, researchers began to form a generally agreed basis for the mechanisms to help explain the observed joining results[15]. First, there had to be a general explanation for how the non-metallic barriers on the surface of the metals to be joined were overcome. For this point, the agreed explanation is that there was rapid displacement of the oxide layers via the high frequency, low amplitude motion of the faying surfaces under an applied load. The oxide layers were thought to be broken into fragments and displaced into the local bulk material. This would result in atomically clean metal surfaces being placed in intimate contact and thus the formation of a bond, in what could be thought to have similarities to an ultrasonically promoted diffusion bond. Secondly, it is agreed that a small zone at the interface is formed in which large amounts of plastic flow occur, creating the weld. This has been

noted to be analogous to producing a micro-friction weld, due to the very small amplitude of motion involved, typically on the order of 10 microns.

An additional common observation has been the activation of dislocations through the use of ultrasonic energy in general[16], specifically, the perceived transmission of dislocations at and across the faying surfaces, as well as the belief that ultrasound by itself, often in the form of acoustic softening or hardening, somehow alters the internal structure of metals[16,17,18,19]. In the case of metals with conventional grain structures, whether relatively coarse, or more refined, Joshi conjectured that the dislocation density clearly plays a role in the relative ease of producing an ultrasonic metal bond[20]. He additionally noted that the commonly postulated concept of localized melting does not apply since the dissimilar bonds that he had analyzed were found to be practically diffusionless and intermetallic compounds were not detected where they may have been expected.

2.3.1. Decreased Flow Stresses

A key portion of the early research regarding ultrasonic bonding was related to the decrease in the flow stress observed in metals during ultrasonic excitation. Langenecker[16] observed that during ultrasonic excitation, the flow stress of metals can be reduced dramatically, similar to the yield stress depression observed during heating, as shown in Figure 4.

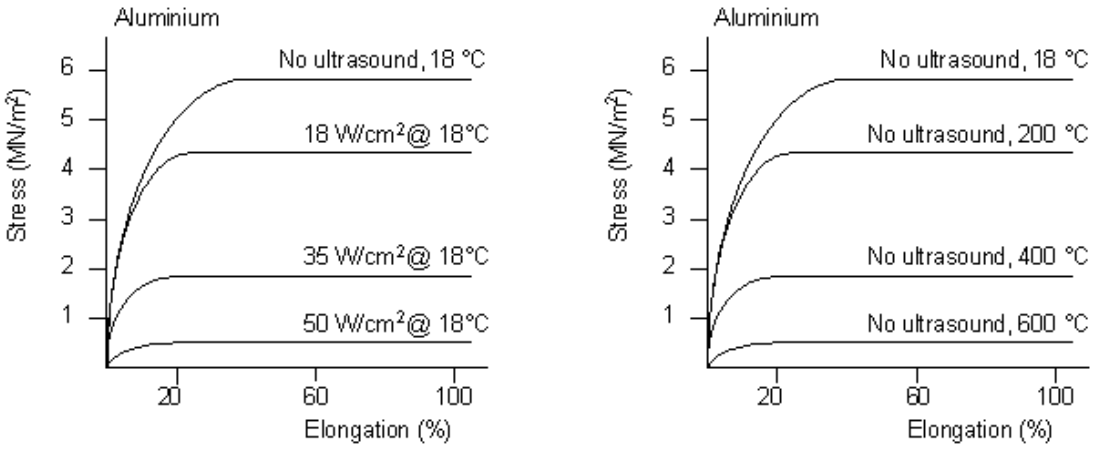

Figure 4 Effect of ultrasonic excitation on the mechanical properties of aluminium. The figure on the left shows the impact of adding ultrasonic energy to the system and the figure on the right illustrates a similar effect upon the addition of heat.

When the ultrasonic excitation is removed, the mechanical properties appear to be instantaneously recoverable. Another interesting aspect of this data is that both thermal energy and ultrasonic energy could be combined to have an additive effect.

While there is currently no clearly accepted answer to the specific joining mechanism in ultrasonic bonding, there have been many prominent theories that have developed from research in the past 50 years[21,22,23,24]. Many of the theories specifically relate to the softening effect that is at the heart of the joining process. Theories proposed by Rhines, et al.[25] related to the transitory dislocation energy transport were of closest correlation to the focus of this present research. Rhines proposed that ultrasonic energy facilitates a large amount of dislocations, which have a transitory existence, thus providing a temporary source of energy for metal transport that could be directed to create the bond.

2.3.2. Transmission Electron Microscopy of Ultrasonic Welds

One of the chief contributors to the lack of clarity as to the nature of ultrasonic welding is that very few studies to date have been able to usefully employ techniques

such as Transmission Electron Microscopy (TEM) to analyze the dislocation structure and topology of ultrasonic welds. Common tools such as the use of Scanning Electron Microscopes (SEM) are unable to provide significant insight relating to dislocation and grain structure. A primary challenge for researchers has been the inability to successfully isolate a known portion of an ultrasonic weld interface due to the TEM sample preparation process. Of the few TEM studies that exist, virtually all of the useful data have been from ultrasonic spot, or wire welding with suspect location identification (ie. confirmed proximity to a known interface).

While rare, there are examples of TEM samples that appear to successfully identify the interface. One such study included the examination of a sample from an aluminium wire bonded to aluminium foil[26]. Results from this experiment showed that in contrast to the common belief of there being diffusion or even melting across the interface, there was no evidence of either when viewed with the TEM. Additionally, the author's examination of the interfaces using the TEM revealed that there was a high degree of inconsistency at the interface where they noted some areas of metal to metal contact next to other areas of debris, oxides, and surface contaminants.

More recent TEM studies have utilized the DBFIB to more accurately identify and extract samples from the bond interface[27]. While Allameh's work had some interesting results related to the transference of sonotrode geometry to interlaminar flow patterns, they had limited success with their TEM analysis. Specifically, they noted that due to the thickness of their TEM samples they were unable to resolve any dislocations inside or at the cell boundaries. However, they did document crystal defects that appeared to be dislocation-like at the cell interfaces (Figure 5).

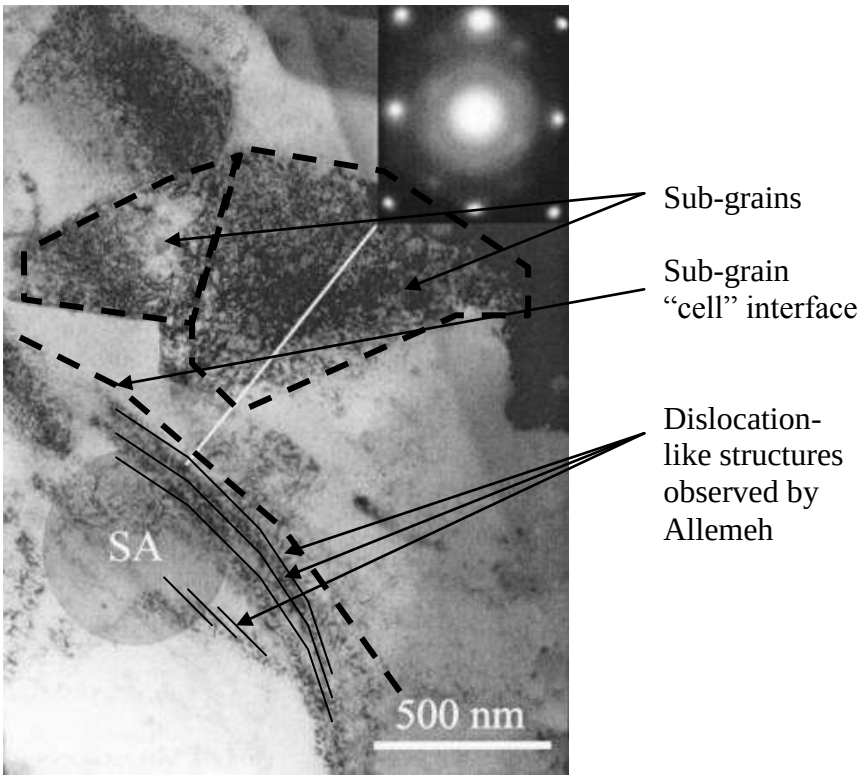

Figure 5 TEM electron micrograph from an aluminium 6111 T4 sample produced from a DBFIB[27]. This is one of the very few examples of ultrasonic sample TEM electron micrographs and provides limited insight.

2.4. Ultrasonic Consolidation

Ultrasonic Consolidation (UC) was invented by Dr. Dawn White[10] (USA,) for fabrication of laminar metal and metal matrix composite structures having highly anisotropic microstructures and high energy absorption capacity, which has been shown to be readily applicable to a wide variety of industries. UC has been initially commercialized as a Rapid Tooling (RT) and Rapid Prototyping (RP) process by Solidica, Inc. which was founded by Dr. White and is located in Ann Arbor, Michigan, USA. Currently, the only commercial form of the UC technology is the Formation™ product offered by Solidica.

UC applies the science of ultrasonic welding to produce bonds between thin layers of material (~120-300 μm thick) without involving the formation of molten metal. However, whereas in nearly all ultrasonic welding processes the output is a

spot weld, in UC, the output is a continuous two dimensional weld "area" made from "continuous spot welds" which are 2.5 cm in width and 150 μm in length. In essence, UC has been described by Solidica, Inc. on their public website as being similar to a micro-friction, metal tape lay-up process, the general mechanics of which are schematically illustrated in Figure 6.

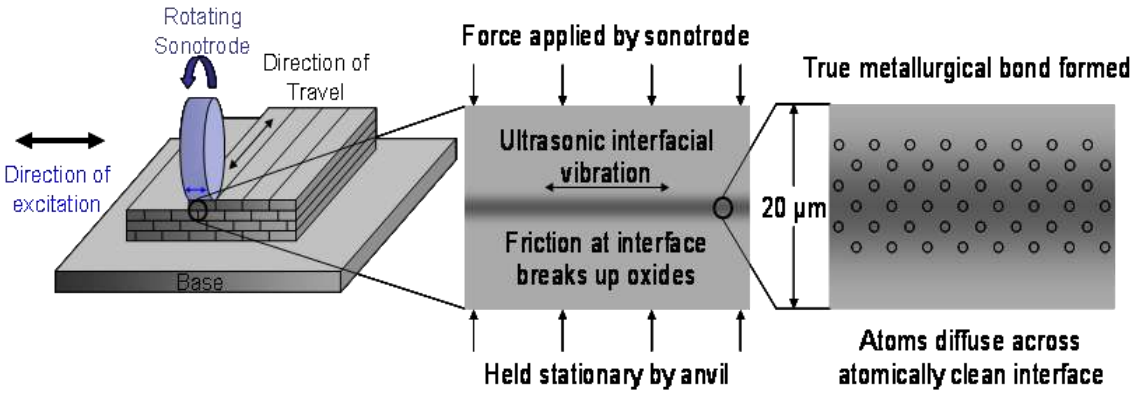

Figure 6 Schematic illustration of Ultrasonic Consolidation process and currently accepted interface mechanisms proposed as diffusion driven.

2.4.1. UC Process Overview

During UC, the material being deposited is translated against the previously built volume, or substrate, at very high frequency and low amplitude, consistent with other ultrasonic welding approaches. It has been theorized that as this occurs, surface contaminants such as oxides are fractured and displaced, and atomically clean surfaces are brought into intimate contact under modest pressures at temperatures that typically are not believed to exceed half of the melting point of the native material (although recent claims of a nano-melt region have emerged[28].) Plastic flow occurs in an interfacial zone believed to be on the order of 10-20 microns in depth and new grains are believed to grow across the interface. A strong, featureless bond zone results, without the coarse, re-melted zones characteristic of liquid phase direct metal additive processes.

From a theoretical standpoint, if the UC process were truly to result in clean identical metals being brought into intimate metal to metal contact under a load, then the strength of the bond would be roughly equal to the bulk material. However, similar to polymeric laminar composites, this metal laminated structure has highly directional properties: in shear, properties 60-70% of wrought materials can be achieved. In tension along the lamination direction, the properties exceed monolithic by about 25-30%. Figure 7 shows the general appearance as seen using a Scanning Electron Microscope across an interlaminar boundary following UC during a part build.

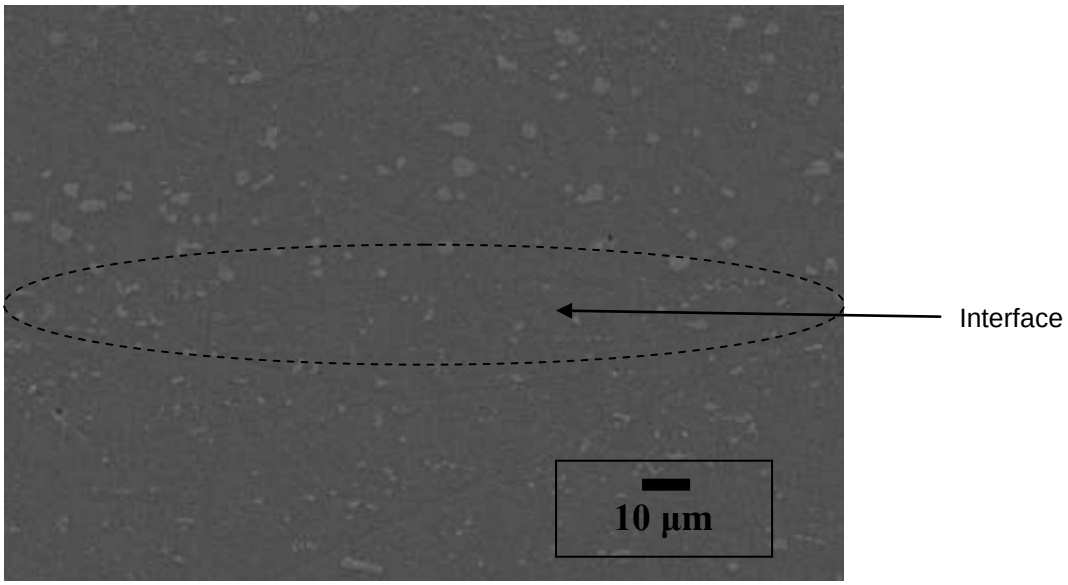

Figure 7 SEM electron micrograph of UC bond zone showing minimal inclusion refinement in weld zone[29].

A recent Charpy test study conducted by Solidica, Inc.[30] illustrates the anisotropic nature of UC in Figure 8. This result demonstrates a significant increase in strength versus wrought material that is similar to strength gains obtained from conventional polymer composite tape lay-up systems.

Specimen type	Result
monolithic	
100 % laminar	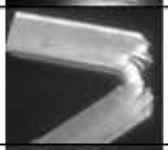
50% laminar, 50% solid, notch in laminate	
50% laminar, 50% solid, notch in solid	

Figure 8 Charpy results for monolithic and UC laminates illustrating directional composite effect of a UC material sample.

UC has been shown however, to be capable of providing up to 99% dense parts for certain geometries and soft metal alloys. Additionally, components produced from standard aluminium alloys with engineering, aerospace and defence applications – such as 3003, 3005, 6061 and 7075 have been produced. Since no infiltrants are required, the properties of the finished part have been believed to be predominantly those of the design intent alloy. Interlaminar voids, a cause for commercial concern for certain applications, seem to be driven at this time primarily by the degree of plastic flow, the operating parameters (ie. horn translation speed, sonotrode force, ultrasonic amplitude) and by the texture of the sonotrode itself (which leaves a residual surface texture on the top of the deposited layer that serves as the substrate texture for the subsequent layer.) A lack of fundamental interfacial mechanism understanding has proved a key limiting factor in eliminating these undesirable features. Figure 9 illustrates a five layer region where all operational parameters were held constant other than the sonotrode amplitude which was reduced

from 20 microns to 10 microns. Note the increase in void volume between the top and bottom SEM electron micrographs in this figure with this single change.

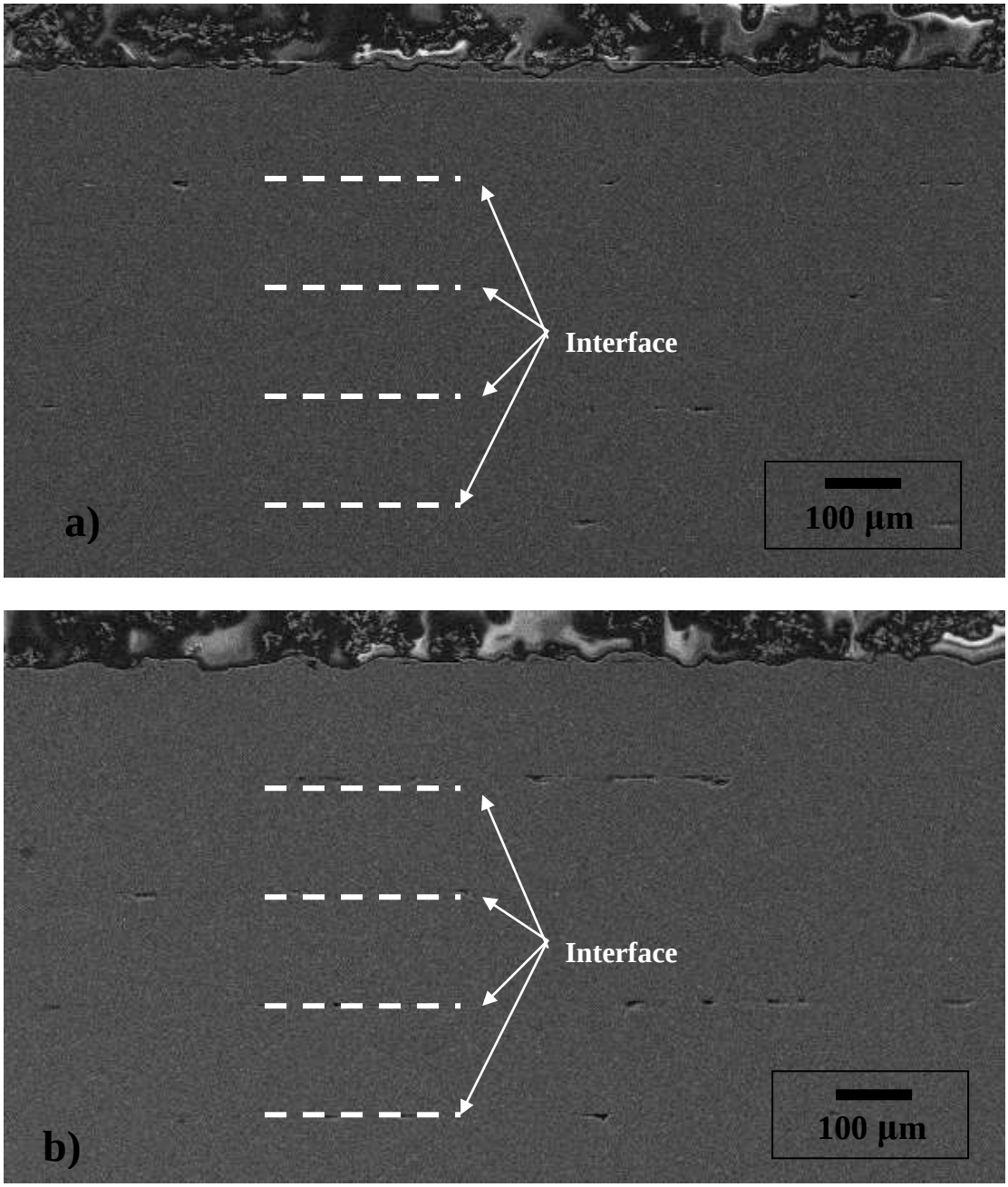

Figure 9 Figure (a) is a five layer UC stack produced with 20 micron amplitude, while an amplitude of 10 microns was used in (b). This one change has had a noticeable impact on the volume fraction of interlaminar voids.

As a solid state processing technology, the UC process has a number of important general benefits in direct manufacture of metal tooling and parts.

- No safety hazards associated with the formation of liquid metal, metal fume, powder handling, dust or other molten metal handling problems.
- No atmosphere control is required to address molten metal oxidation issues.
- Low energy consumption, due to the low temperatures involved and small volumes of material actually affected.
- Reduced residual stresses and distortion.
- Higher deposition rate because lower heat input per deposited volume means less time is required for heat dissipation.

Additionally, UC possesses the desirable ability to bond dissimilar materials together to form multi-metallic laminates. An example of a recent sample produced by Solidica, Inc. is shown, Figure 10[31].

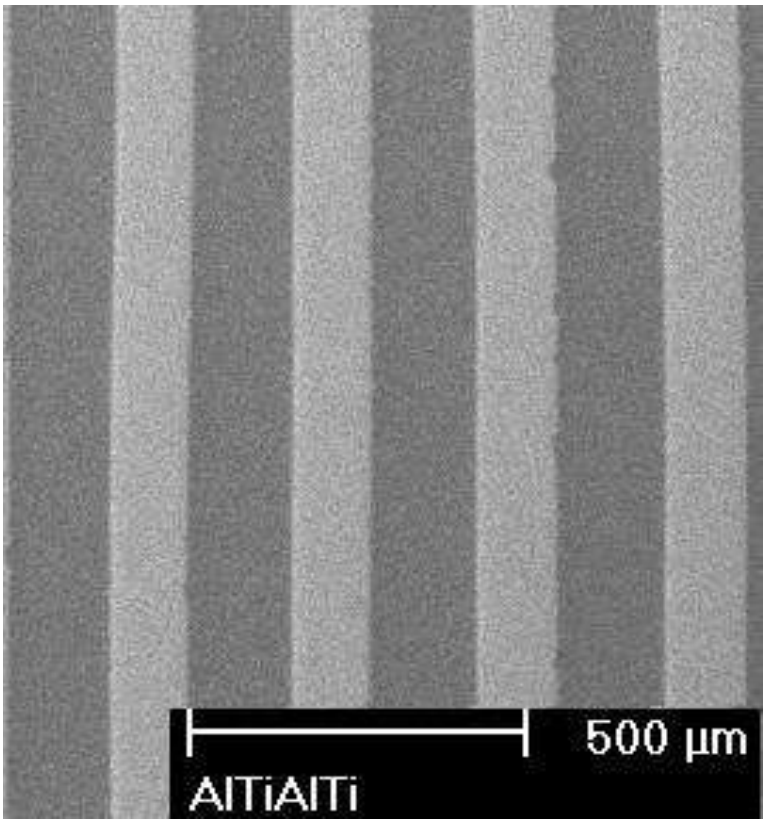

Figure 10 Recent titanium/aluminium dissimilar material weld sample fabricated using UC process. Note that the titanium is the darker of the two regions.

2.4.2. Current Production Equipment

Solidica is currently the only manufacturer of UC equipment worldwide. Their first production machine, called Formation™, incorporates a base CNC machining centre with the ultrasonic deposition module and the necessary hybrid software that they refer to as RPCam™. The software is necessary to manage the material deposition and removal stages, as normal CNC Computer Aided Machining (CAM) software has only removal capabilities. The software instructs the machine when, and how many layers, to deposit, and then when, and how much material to remove via machining (and at what accuracy.) The current UC machine and an illustration of the major components are shown in Figure 11.

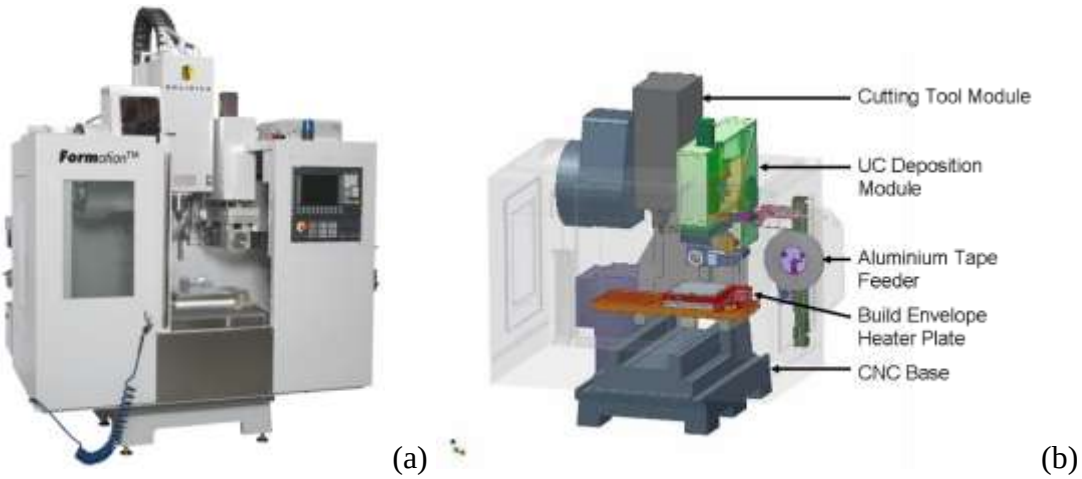

Figure 11 Current commercial ultrasonic consolidation equipment where (a) is the commercial Formation machine and (b) provides an overview of the key system components.

2.4.3. Ultrasonic Consolidation

The field of research surrounding the ultrasonic consolidation process is currently experiencing a near exponential increase. Following the commercial release of the first UC machine in late 2004, several research minded early adopters quickly

purchased a machine and began their respective exploration. To date, research has begun and is continuing at the following international research sites:

- Loughborough University (Alpha UC system in house)
- Clemson University (UC in house)
- University of Michigan
- Utah State University (UC in house)
- Michigan Technological University
- Saginaw Valley State University (UC in house)
- EWI (UC in house)
- Army Research Laboratory

Unfortunately, the primary focus of the initial research has primarily been on the applied side, yielding little in the form of fundamental mechanism analysis. Regardless of this fact, it is clear that there will be a great surge of published work in the area of UC over the next 3-10 years. A summary of the key research activities that have been concluded are provided in the following sections and are broken into the following focus areas.

- Process characterisation
- Plastic flow
- Fibre embedment
- Support material
- TEM electron microscopy of UC welds
- Surface free energy

2.4.3.1. Process Characterisation

Kong, Soar, and Dickens have recently published several papers reporting on studies related to the characterisation of the process parameters of UC, specifically for aluminium 6061 and aluminium 3003[32,33]. These two materials are commonly used in the UC process and offer an interesting contrast due to their very different surface oxide and bulk mechanical properties. While the focus of the study on 3003 was on general processing optimisation, the study of 6061 began to address initial surface roughness. Kong et al. noted that weld quality improved when the surface was cleaned, lending credence to the generally accepted observations that the bonding mechanisms in UC can only advance once the initial oxide layers are either removed or fractured and displaced[34]. In addition to this, Kong et al. showed that the bond efficiency changed significantly when the bulk process parameters of amplitude, contact force, and weld speed were modified. This outcome would be expected when one considers the various dislocation and friction theories that have been put forth in general for ultrasonic bonding, as all three of these factors would contribute to friction, dislocation and slip. Figure 12 illustrates an example of the characterisation results developed during these studies.

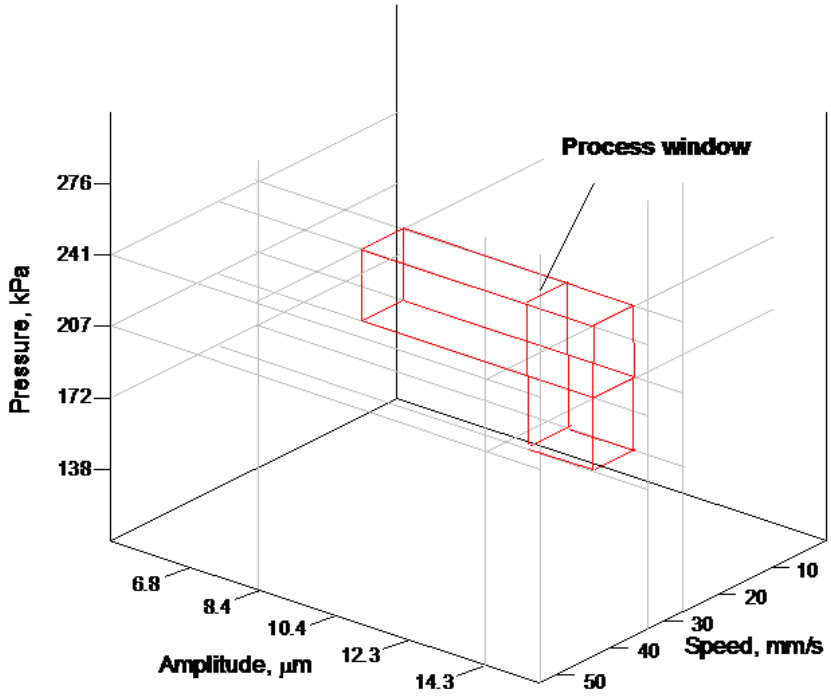

Figure 12 Characterization results from Kong, et al.[32] for aluminium 3003 illustrating the collective influence of the three major processing parameters of speed, amplitude, and pressure.

2.4.3.2. Plastic Flow

In structures under a multidirectional load such as in the UC process, the stress state is not a simple uniaxial state but a more complex tri-axial state of stress. Plastic deformation (also called plastic flow) will occur in a material when the effective stress, σ_{eff} exceeds the uniaxial yield stress. The equation for the effective stress when a tri-axial state of stress exists and σ_1, σ_2, and σ_3 are the principal stresses in the three orthogonal directions is provided below. This relation is also known as the distortion energy theory, or the Von Mises stress equation, named after its originator[35].

$$\sigma_{eff} = (\sqrt{2}/2)\,[(\sigma_1 - \sigma_2)^2 + (\sigma_2 - \sigma_3)^2 + (\sigma_3 - \sigma_1)^2]^{1/2} \text{ ----------[2.1]}$$

Observing this equation from a UC perspective, one can see some interesting concepts. If there is no tension, but sufficient biaxial compression in the other two

directions, then there could be axial yielding in extension in the third direction. (This is like squeezing a cylinder of putty in your hand and having it extrude out each end). The ability of the UC process to produce this form of movement has been previously documented by C. Yen, et al.[32], and is shown in Figure 13.

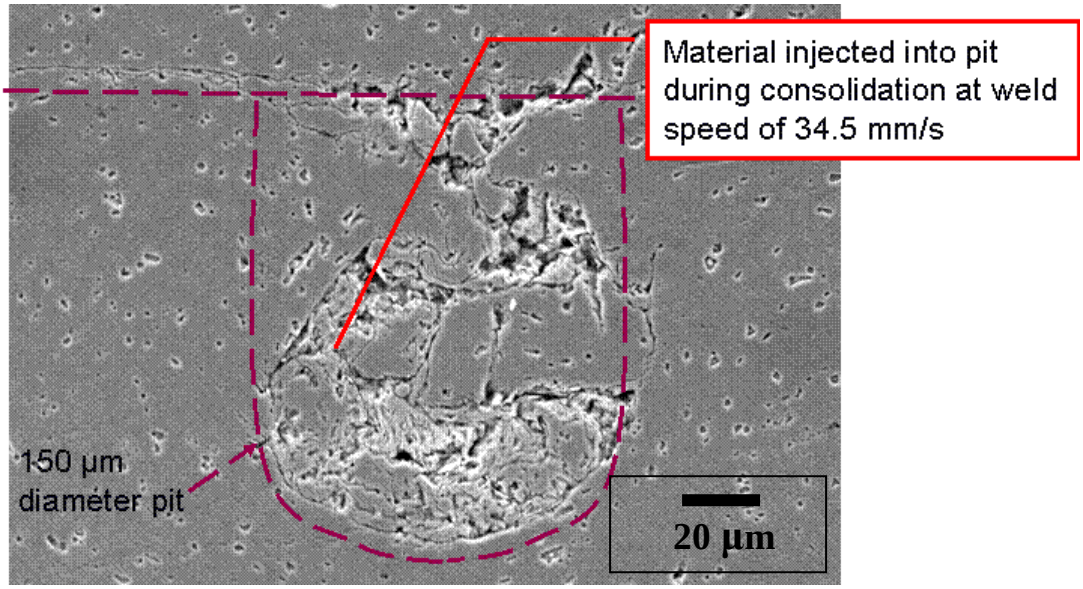

Figure 13 Observation of plastic flow caused by tri-axial stress state conditions that led to the "filling" of a 150 micron pit within the substrate following a subsequent foil deposition.

What is particularly interesting is how this result seems to be at odds to a degree with conventional mechanics of materials when variable "hole widths" are used. To illustrate this concept, consider the conventional beam mechanics system as illustrated in Figure 14. In this case when a force is applied to a beam, the well supported beam in Figure 14a would see little deformation as illustrated by the red dashed line (due to a minimal bending moment). Meanwhile, the same force applied to the more broadly supported beam would experience a much more significant displacement as in Figure 14b.

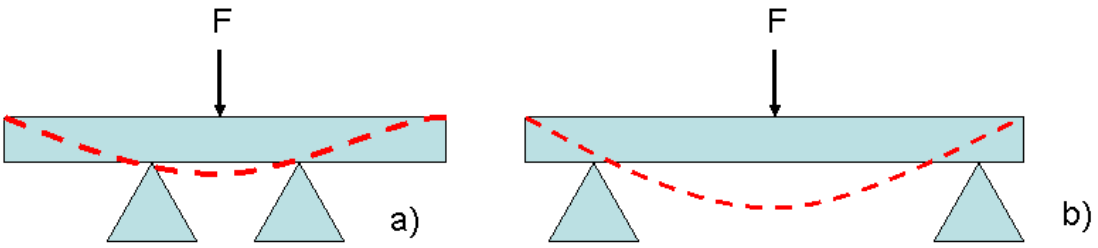

Figure 14 Illustration of conventional force deflection mechanics. a) Minimal displacement of well supported beam under force F, b) greater displacement under same force under less supported scenario.

In the UC process the phenomena that is observed is the exact opposite. In UC, it has been demonstrated again by C. Yen, et. al. that the wider the hole diameter, the less observed plastic flow and subsequent material displacement. Figure 15 illustrates two examples of this observed behaviour where the operating conditions were all consistently maintained and only the width of the hole was varied from 30 µm to 400 µm. In this case and others like it, the ability of the deposited layer to "fill" the hole was increased as the gap was narrowed.

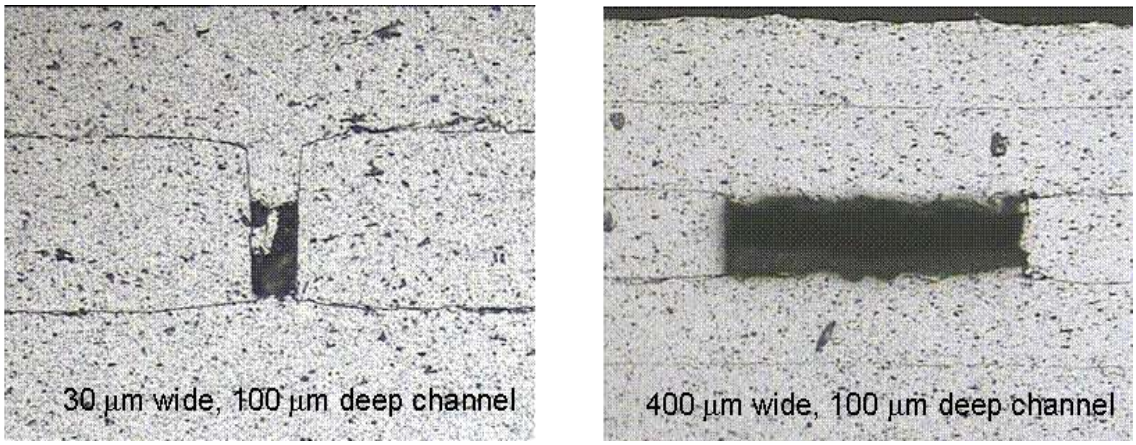

Figure 15 Evidence of contact driven softening dynamics within UC interface. The micrograph on the left illustrates how a smaller gap leads to increased material compliance when compared to the large gap on the right.

This observed behaviour would seem to indicate that the perpendicular force being applied by the sonotrode is not the governing force in the UC process. What is inferred is that softening effects are dominated by interfacial contact and the resultant affect on the materials local plasticity. Imagine the region affected by the interfacial softening effect is called the "deformation affected zone" (DAZ). In the case of the smaller diameter hole, this region would be able to "span the gap", overlap and propagate downward due to its softened state and reduced flow stress. An illustration of this possibility is show in Figure 16.

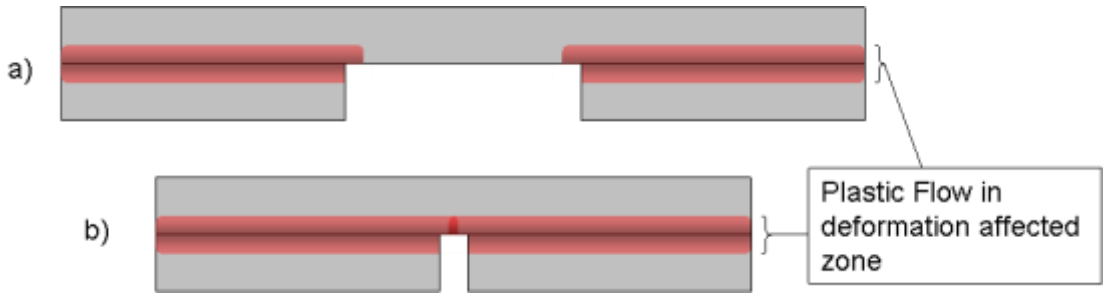

Figure 16 Theorized overlap of deformation affected zone (DAZ) (a) with example of case where the plastic work region resulting from UC is within close proximity to additional DAZ regions (b).

2.4.3.3. Fibre Embedment

Another intriguing element of the UC process stemming from the decreased flow stress is the ability to embed a wide range of secondary materials and articles in between the aluminium "matrix" layers during UC without damage, particularly in cases where one might expect such damage due to sonotrode normal forces alone. For example, hollow glass fibres with crush strength of 100N/in[36] can survive the process, well below that caused by the 500N normal force applied over a fraction of an inch). Some other examples of embeddable fibre elements include:

- Optical fibres

- Thermocouples
- Shape memory alloy (SMA) fibres
- Piezoelectric fibres
- Sensors
- Antennas

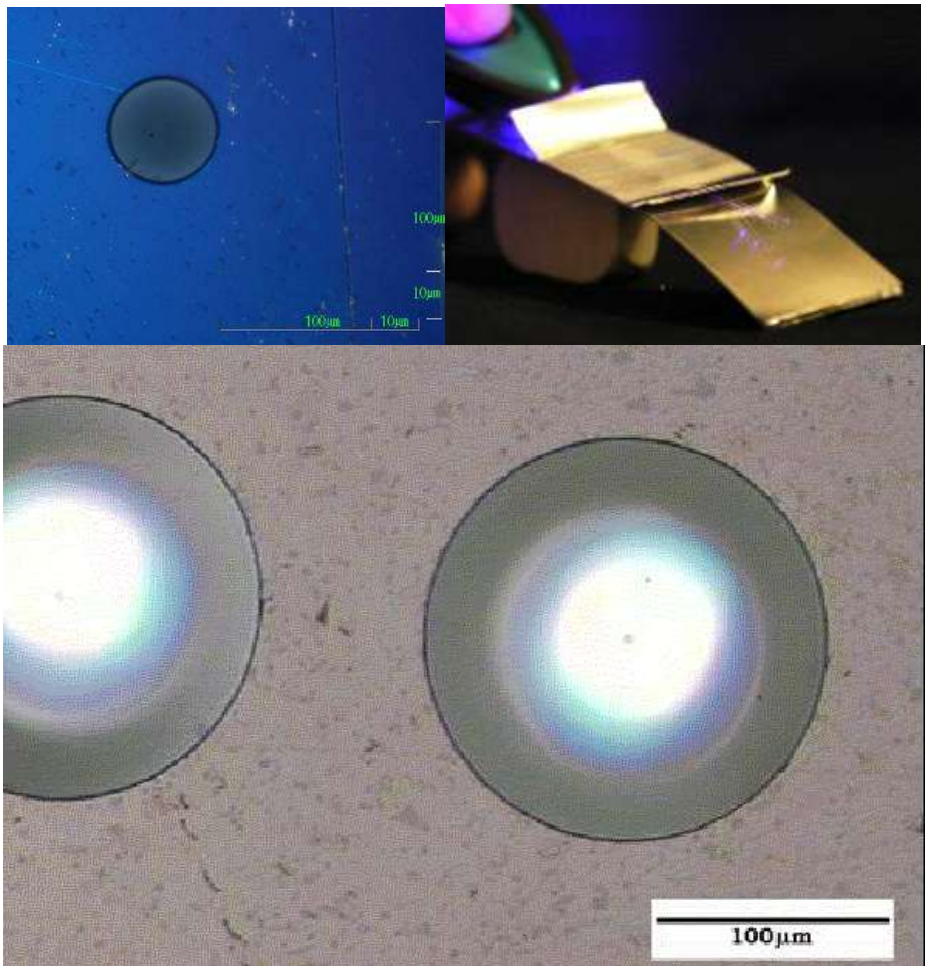

Figure 17 Optical fibres embedded via ultrasonic consolidation.

Similar to optical fibres (Figure 17), other materials such as shape memory fibres, structural fibres, piezoceramic fibres, and thermocouples can be embedded in a metal matrix via UC. An example of SMA fibres embedded in an aluminium matrix via UC is shown in Figure 18[37]. Recent experimentation by the University of Michigan and Loughborough University[38] has shown that heating produces the

characteristic actuation response, even after the SMA fibre has undergone the UC process. This has been initially explained by the fact that the low UC processing temperatures are well below the recrystallisation temperatures of the SMA fibres, thus maintaining their desired memory behaviour.

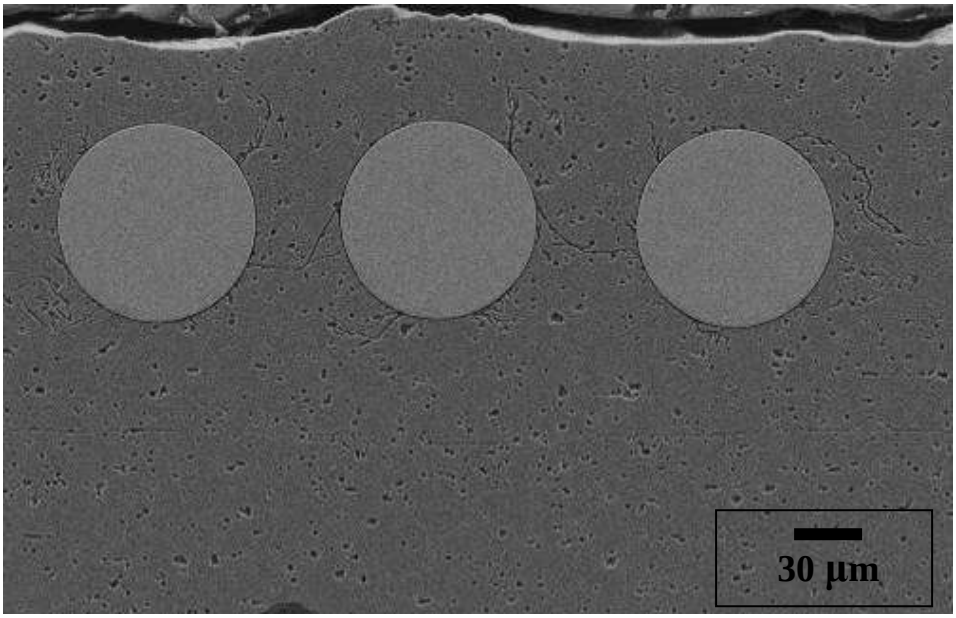

Figure 18 Shape memory alloy embedded via ultrasonic consolidation into an aluminium matrix[37].

It is clearly intriguing that the material in Figure 18 was able to soften to the point of forming around the fibre elements given their relative hardness and surface smoothness. One might infer that a high degree of surface texture is either not required, or that the fibres themselves served as incredibly large surface features that initiated and propagated the plastic flow and may also serve as local heat sinks to enhance local thermal retention.

2.4.3.4. Support Material

Ongoing unpublished work at Solidica that was initiated in 2004 has been focused in the area of developing an automated support material system for the UC process. The

driver for this work relates to the need to expand the free form fabrication geometries that can be made with the UC equipment being offered by Solidica. For example, a support material system would conceivably allow for the fabrication of cantilevers, large internal geometries, and high aspect ratio features. While the bulk of the research in this area is not of direct relevance to this research proposal, the driving factors related to the need to immobilize the substrate is of special importance.

It would seem at this time that the driving factor behind poor weld quality on features such as those with high aspect ratios, is influenced by the inability of the current system to establish sufficient interfacial bonding dynamics (such as adequate relative motion between the new foil layer, and the subsequently deposited layers that make up the substrate shown in Figure 19). Poor relative interfacial motion would theoretically prevent the development of highly plastic flow within the interlayer region. Without this flow, mating surfaces would not come under significant contact with one another and bonding across the bond line would not progress.

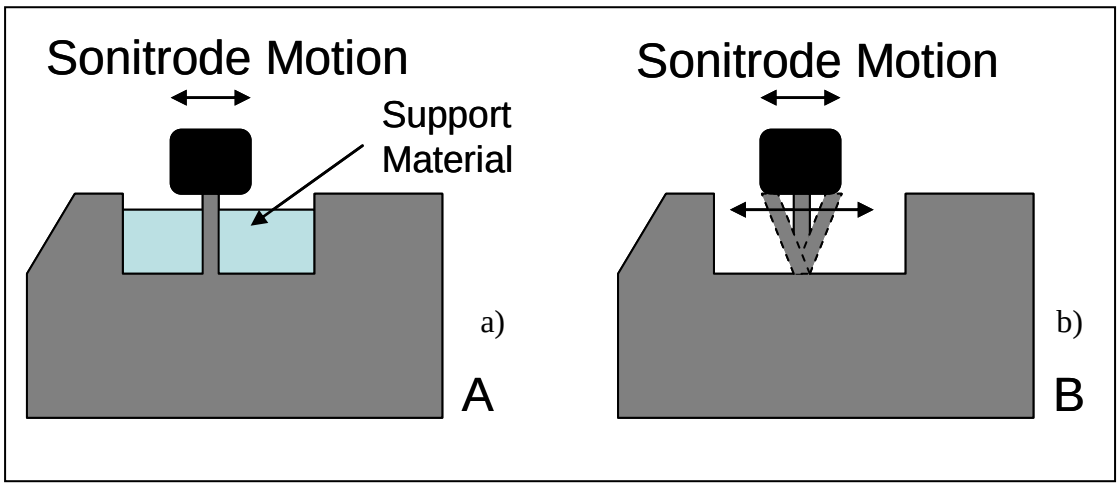

Figure 19 Illustration of the need for support material to drive interlaminar relative motion. (a) high aspect ratio feature immobilized by rigid support material, (b) movement of unsupported high aspect ratio feature geometry.

2.4.3.5. Transmission Electron Microscopy of UC Welds

As noted earlier, essentially all of the successful studies in the field of ultrasonic welding that have employed TEM in the analysis of the nature of their bonds have been conducted on ultrasonic spot, or wire welding. There has not been any success with UC samples when utilizing TEM due to the difficulty in conventional TEM sample preparation methods. Specifically, the challenge has always been due to the fact that a ~3 mm diameter sample is required, and to fabricate such a sample in UC would require at least 20 separate 150 μm layers in a stack. While this is quite easy to accomplish with the UC process, the interlaminar regions fail to survive the TEM thinning preparation process. This is less of a challenge in conventional spot welding where the welds are far more robust and the layers being bonded are typically 3-8 mm thick.

2.4.3.6. Surface Free Energy

An intrinsic material property that has recently been suggested by Solidica to influence bond formation with the UC process is the surface free energy (γ) shown in Table 1. The ratio γ/σ_y is the ratio of free energy vs. yield strength of the material. Although the units of this ratio are in units of distance, it is a good indication of the galling potential of a material. The larger the ratio, the more susceptible it will be to galling and adhesion[39]. Surface free energy is however, a function of the yield stress and as will be shown in the Chapter 7, the yield stress within a UC bond is highly variable and transient in nature.

Table 1 Table of soft materials, and the ratio of surface free energies to their yield strengths[40].

Metals	γ, erg/cm^2 (mj/m^2)	σ_y, N/m^2	γ/σ_y, mm
Indium	630	3	210×10^{-6}
Lead	450	13	34
Aluminum	900	70	13
Copper	1100	130	8
Nickel	1700	250	7

3. Dislocation Mechanics and Aluminium Cubic Structure

Hansson and Tholen conducted several static and dynamic strain tests in the mid 1970's in an attempt to further clarify the effect of ultrasonic excitation on metals[41]. In their experiments they applied a static tensile load to a specimen and then added an ultrasonic stimulation to the sample using an amplitude setting of 50 μm. Similar to other experiments during that time, they observed an effect in the form of a drop in the strength and ductility of the material. After conducting TEM tests on the samples, that were statically stressed only, dynamically stressed only, and both statically and dynamically stressed, they observed that the superposition of ultrasound on an ordinary tensile test of aluminium resulted in regions with relatively low dislocation density in a matrix of high dislocation density. This result was essentially a hybrid of the high dislocation densities observed in an ordinary tensile test sample (without ultrasound), and the lower dislocation densities observed in a cell structure where only dynamic stresses were applied. The results contributed significantly to the generally accepted idea that there existed a relationship between the application of ultrasonics in metals and dislocation mechanics.

3.1. Slip

The usual method of plastic deformation in metals is by the sliding of blocks of the crystal over one another along definite crystallographic planes, called slip planes[35] (Dieter, p. 114). Line defects, or dislocations, are the structural defect responsible for the phenomenon of slip. In the absence of obstacles, such as particulates and grain boundaries, a dislocation can move easily on the application of only a small force, allowing real crystals to deform much more readily than would be expected for a

crystal with a perfect lattice (ie. a lattice free of any internal obstacles, lattice flaws, with consistent spacing between all lattice atoms).

There are two basic types of dislocations which lead to slip: edge dislocations, and the screw dislocation. Figure 20 shows the atomic arrangement in a plane normal to an edge dislocation. There is one more vertical row of atoms above the slip plane than below it which results in a compressive stress above the slip plane and a tensile stress below it. The notation ⊥ indicates a positive edge dislocation.

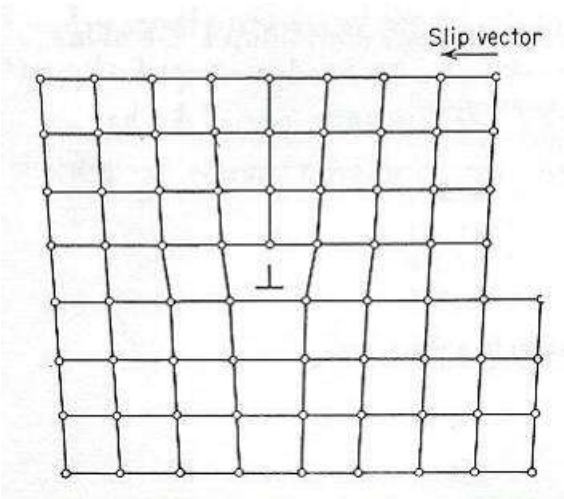

Figure 20 Atomic arrangement in a plane normal to an edge dislocation.

Slip occurs in the close packed planes of all lattice structures. Aluminium, as with certain other metals, show additional slip systems with increased temperature[35]. On an atomic level, slip involves the sliding of the close-packed atoms one over another. These atoms are sheared over each other and produce a displacement in the slip direction but as opposed to taking a direct route to their new location, they move in a zig-zag motion (as the atoms themselves do not deform). Figure 21 represents a classical illustration[42] of this motion illustrating how the bottom of the top left atom moves up and over the central atom (B) to move from being to the upper left of B to the upper right of B.

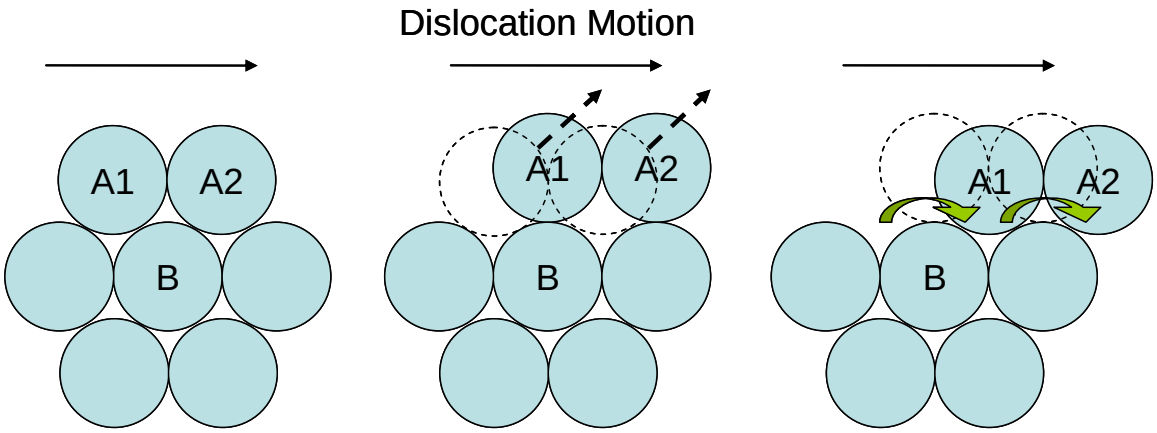

Figure 21 Slip in face-centred cubic crystals showing one atomic slip movement.

3.2. Face Centred Cubic Structure

Most commercial applications of ultrasonic metal welding involve face-centred cubic (fcc) materials due their superior ultrasonic weldability. One theory as to why this is the case is believed to be related to the relatively large number of slip systems available (12) within an fcc lattice structure and the fact that relatively low shear stresses can produce slip. Hexagonal close packed (hcp) materials, such as titanium, have only 3 slip systems, and are generally relatively brittle, although more slip systems become available at elevated temperatures for some hcp materials due to the fact that the lattice structure transforms into a body centred cubic structure. In the case of body centred cubic (bcc) metals such as industrial steels, 12 slip systems are nominally operable. Unfortunately, the close packed structure of bcc materials as compared to fcc would potentially provide stronger resistance to dislocation propagation. The close-packed structure is the geometric arrangement in which the atoms of the unit cell may be packed together in a minimum total volume. Wireframe examples of fcc structured and bcc structured unit cell are shown in Figure 22.

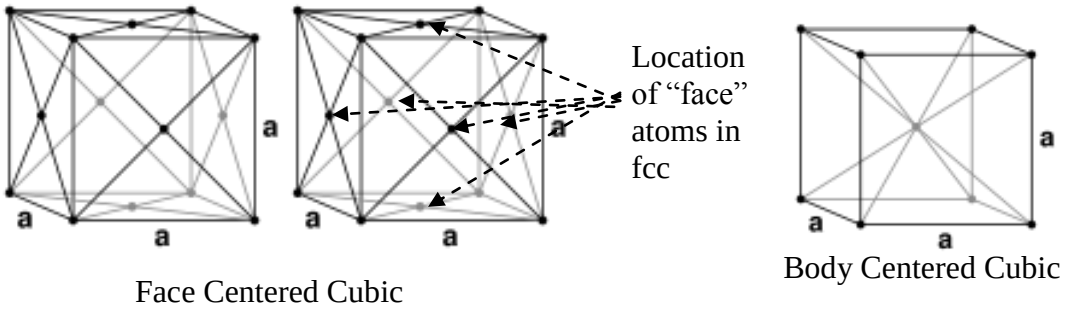

Figure 22 Example of fcc and bcc unit cell structures.

In fcc structures the atoms are positioned at the eight corners of a unit cell and at the centres of all the cube faces. Since these latter atoms belong to two unit cells, there are four atoms per structure cell in the fcc lattice. Seventy-four percent of the volume of the unit cell in an fcc crystal is occupied by atoms in contrast to sixty-eight percent packing for a body-centred cubic structure. As noted, the increased atomic "packing" in the fcc structure affords many more possible geometric slip planes which is often easier to visualize when three dimensional atomic representations are used as in Figure 23. Referring to this figure, imagine each atom is somewhat like a brick set in a pile, and that the energy required to slide two bricks against each other is far less than the energy to shear a brick itself. The fcc, possessing more bricks, and thus more weak brick to brick interfaces, would be easier to disrupt than the bcc brick pile given the bcc pile would have fewer brick to brick interfaces. Additionally, given the higher number of brick to brick interfaces in the fcc structure (slip planes), there are many more possible angles by which a slip in the brick stack may occur.

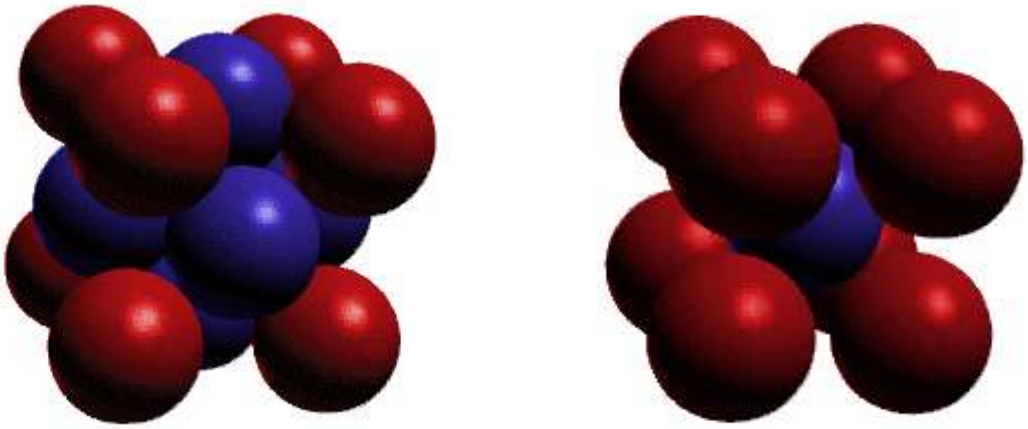

a) b)

Figure 23 Three dimensional representation of the fcc atomic lattice structure (a) and the bcc atomic lattice structure (b)[43].

Aluminium, copper, gold, lead, silver, and nickel are common fcc materials and are frequently used in ultrasonic welding processes.

3.3. Critical Resolved Shear Stress for Slip

In the UC process, external loads produce a shearing stress at the interface which is translated into the mating materials. Slip will begin when the shearing stress on the slip plane in the slip direction reaches a threshold value called the critical resolved shear stress. This value can be considered the single-crystal yield stress equivalent and depends chiefly on composition and temperature. The magnitude of the critical resolved shear stress of a crystal is determined by the interaction of its population of dislocations with each other and with defects such as vacancies, interstitials, and impurity atoms[35].

3.4. Stacking Faults

The UC process utilizes rolled foil as the layered building blocks to fabricate the part layer by layer. These rolled materials have thus already undergone extensive plastic

deformation. Faults in the stacking sequence of fcc crystals can be produced by this plastic deformation[44]. It has been noted by Dieter that the differences in the deformation behaviour of fcc metals are due to the differences in stacking-fault behaviour. In general, the lower the stacking-fault energy the greater the separation between the partial dislocations and the wider the stacking fault[45]. Table 2 displays typical values of stacking-fault energy for certain metals.

Table 2 Typical values of stacking-fault energy

Metal	Stacking-fault energy, $mJ/m^2 = erg/cm^2$
Brass	<10
303 stainless steel	8
304 stainless steel	20
310 stainless steel	45
Silver	25
Gold	50
Copper	80
Nickel	150
Aluminium	200

3.5. Grain Size Effects

The operation of dislocation sources is also grain-size dependent as is shown by the Hall-Petch relationship where the yield stress is proportional to the inverse square root of the average grain size[46]. Therefore in the case of highly refined grain structures (such as seen in nano-grained materials) dislocation activity becomes very difficult. An alternative condition known as the inverse Hall-Petch behaviour argues that with increasing volume fraction of interfaces, the grain boundary processes might become more effective, resulting in a material becoming softer with a further decrease in grain size[47].

There are currently only two existing material samples that have been produced with the UC process that sheds any light on this topic from an experimental standpoint. Solidica, Inc., and the University of California - Davis collaborated in 2005 in an attempt to directly UC fabricate a small test sample of cryo-milled, nano-structured 5083 material. The initial results showed that while a moderate weld was achieved, it was characterized by high interlaminar void concentrations and readily delaminated under moderate to high impact force loads (Figure 24).

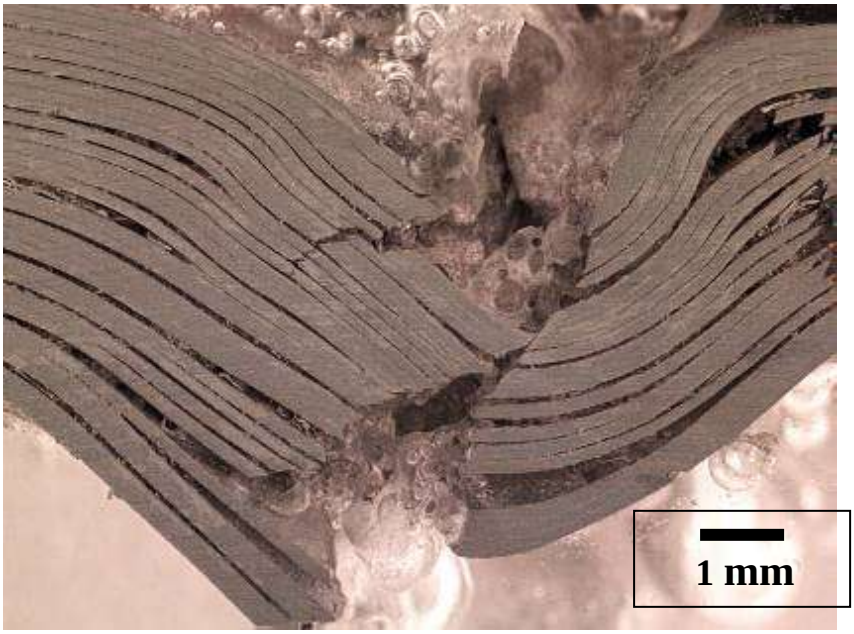

Figure 24 Nano-grained UC sample during impact test.[48]

A second attempt was made to bond the nano-grained material together through the incorporation of an 1100 aluminium interlayer[48] (Figure 25). These samples showed excellent weld quality with very low interlaminar void fractions. No further studies beyond this have been published to date.

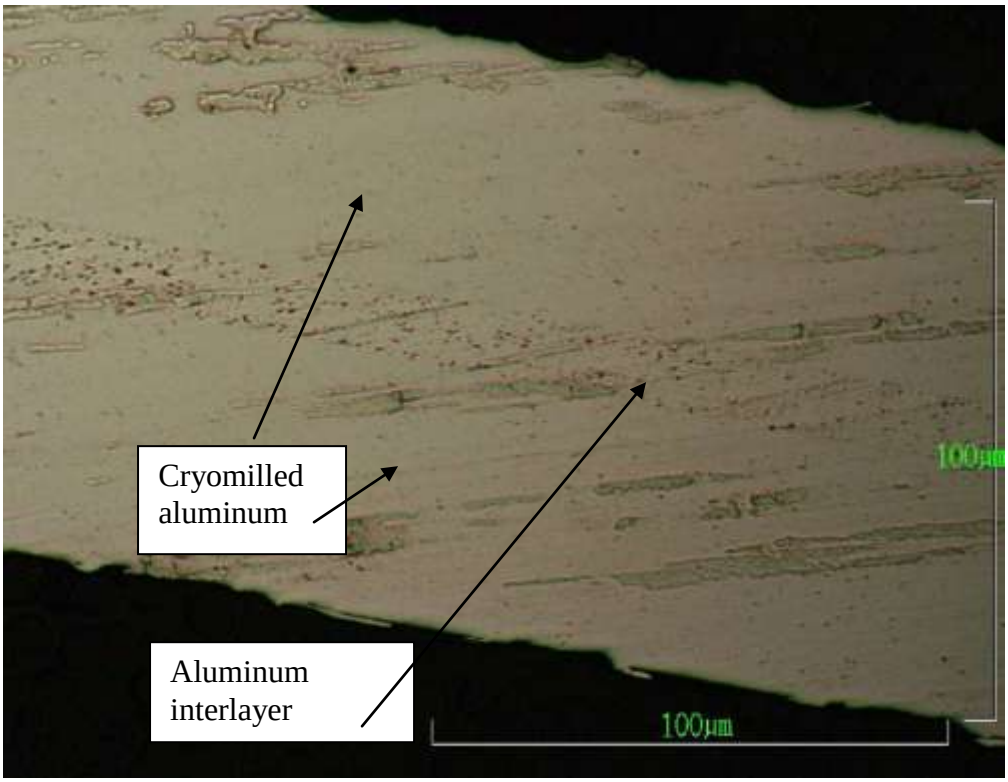

Figure 25 Two layers of cryo-milled nano-grained 5083 bonded using an 1100 interlayer.

During these experiments, no characterization of the bond zone was performed to determine what type of microstructure formed at the interface, and how it differed from one side to the other. As such, it is still unclear as to the exact character of the interfacial region of the ultrasonic bonds formed between nano-grained and conventionally microstructured aluminium foil pairs, and those produced between two nano-grained foils. Future efforts are planned to determine whether diffusion processes or dislocation motion processes dominate, so that techniques for production of bulk nano-grained material, and net shape direct article fabrication can be developed.

4. Bauschinger Effect and Mechanical Softening

The Bauschinger Effect[49] is a general phenomenon in polycrystalline metals and describes the mechanism in a specimen when it is deformed plastically beyond the yield stress in one direction and then after unloading to zero stress is reloaded in the opposite direction (Figure 26). The effect is summarized by the fact that the yield stress on reloading will be less than the original yield stress of the material and that subsequent loadings and reverse loadings will continue to reduce the materials yield strength.

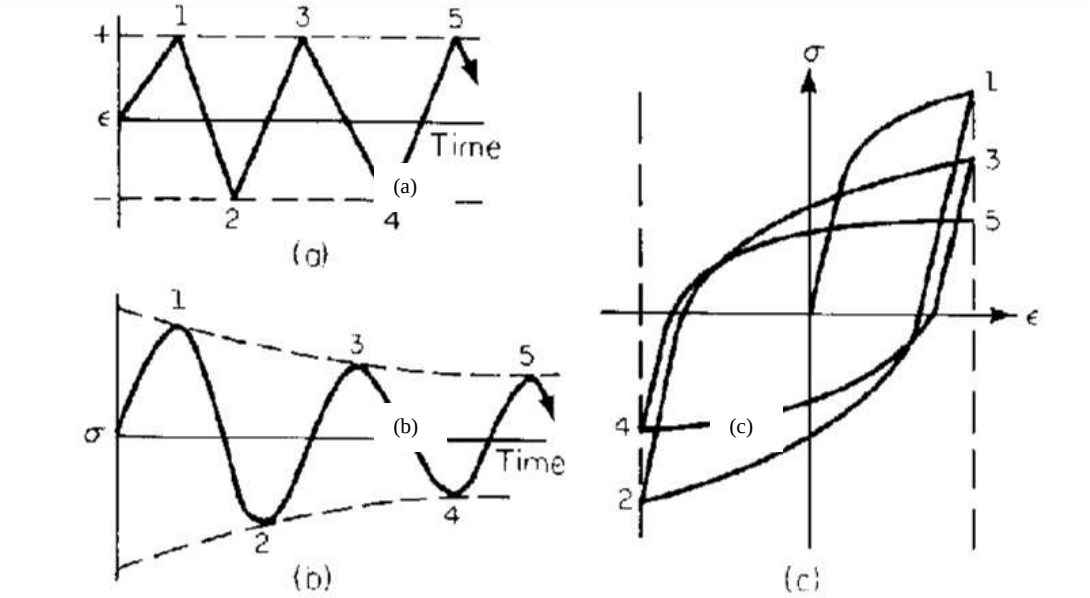

Figure 26 Cyclic softening: (a) constant strain amplitude; (b) stress response (decreasing stress level); (c) cyclic stress-strain response.[49]

A common representation of the Bauschinger Effect is shown in Figure 27. The Bauschinger Effect has been shown to have important consequences in metal-forming applications. For example, it can play a major role in the bending of steel plates [50] and results in work-softening [51] when severely cold-worked metals are subjected to stresses of reversed sign.

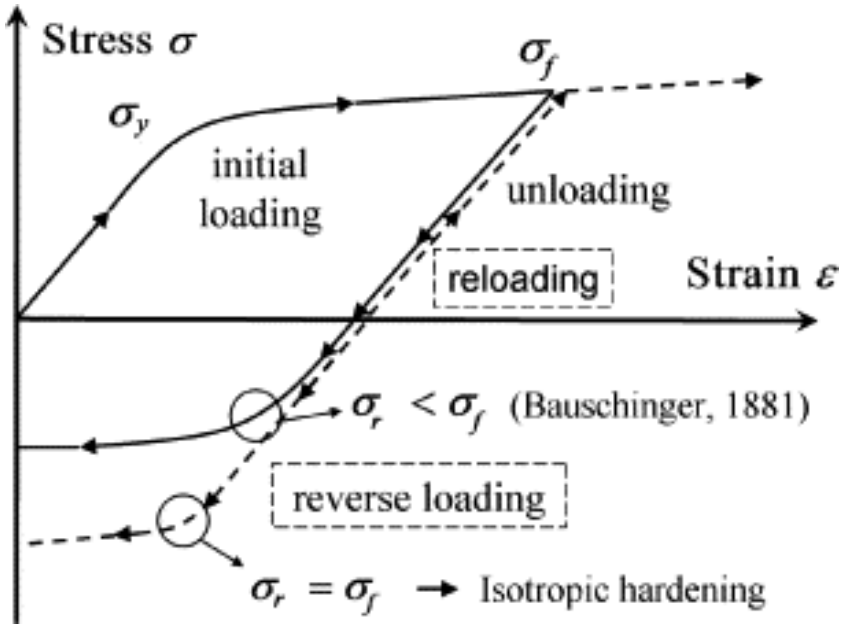

Figure 27 Stress-strain relationship of Bauschinger Effect.[52]

Many experimental and theoretical efforts have been devoted to studying the Bauschinger effect in bulk metals since the phenomenon was first reported[53,54,55,56,57,58,59,60,61,62]. The physical origins are generally ascribed to either long-range effects, such as internal stresses due to dislocation interactions[56,57], dislocation pile-ups at grain boundaries[58,59] or Orowan loops around strong precipitates[60,61,62] , or to short-range effects, such as the directionality of mobile dislocations and their resistance to motion or annihilation of the dislocations during reverse straining[60].

In a recent set of experiments on aluminium, sequences of simple shear followed by reverse loading were performed to investigate the behaviour of the material under forward loading followed by reverse loading. During Bauschinger experiments, the slip systems activated during the pre-strain are believed to be re-activated in the reverse direction during the reloading[63]. It was noted that with a

variety of aluminium alloys, the experiments generally lead to a lower yield strength, which were followed by a transient stage where the strain hardening rate ($d\sigma/d\varepsilon$) fluctuates, possibly reaching very low levels or becoming negative[64].

Orowan [65] discussed how dislocations will accumulate at barriers in tangles during plastic deformation. When the load in one direction is removed and an opposite load is applied, the initial dislocation lines make it effectively easier to achieve low shear stress movements in the new direction, creating persistent slip bands. Figure 28 shows a TEM sample of post Bauschinger tested Au samples displaying dislocation networks[66].

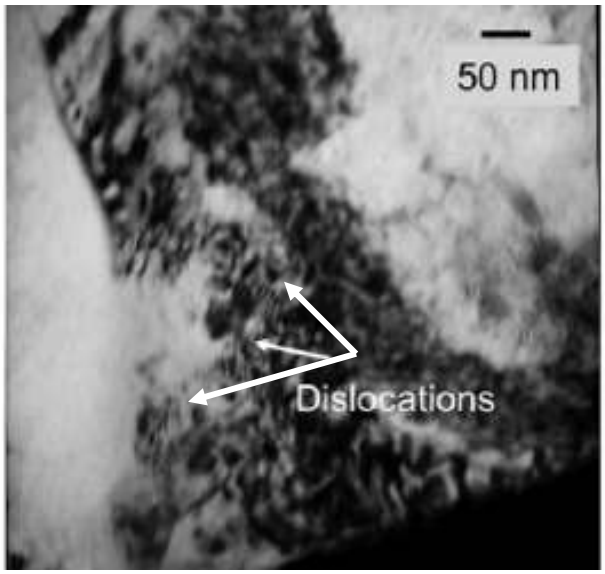

Figure 28 Dislocation network following the cyclic plastic activity of 0.3 μm thick Au films. The dislocations in this micrograph are generally identified by the dark "lines" often seen parallel to one another.

Another recent series of TEM-based analyses on drawn 6063 aluminium alloy (Figure 29) showed the development of dislocation rich formations and sub-grain refinement after only 20 cycles[67]. This result played a key role in the analysis of the final research results in that one of the general signs that the Bauschinger Effect occurred is a decrease in sub-grain size. The term "sub-grain" is used in this case, as

well as through much of this present research, to differentiate between high angle boundary grains and low angle boundary sub-grains (that often occur as sub-structures in larger high angle boundary grains).

An additional attribute when the Bauschinger Effect is present is the pileup of dislocations and/or a decrease in sub-grain size in and around obstacles such as precipitates or particles as can be seen in Figure 29(a). It has been further shown that the presence of such obstacles seems to limit the Bauschinger Effect in materials, possibly explaining why precipitation hardened materials such as 6061 aluminium are difficult materials to ultrasonically weld[63]. While the focus of the study was related to understanding the effects of manufacturing processes on the end material output, the TEM electron micrographs provide another example of the residual "fingerprints" of cyclic deformation.

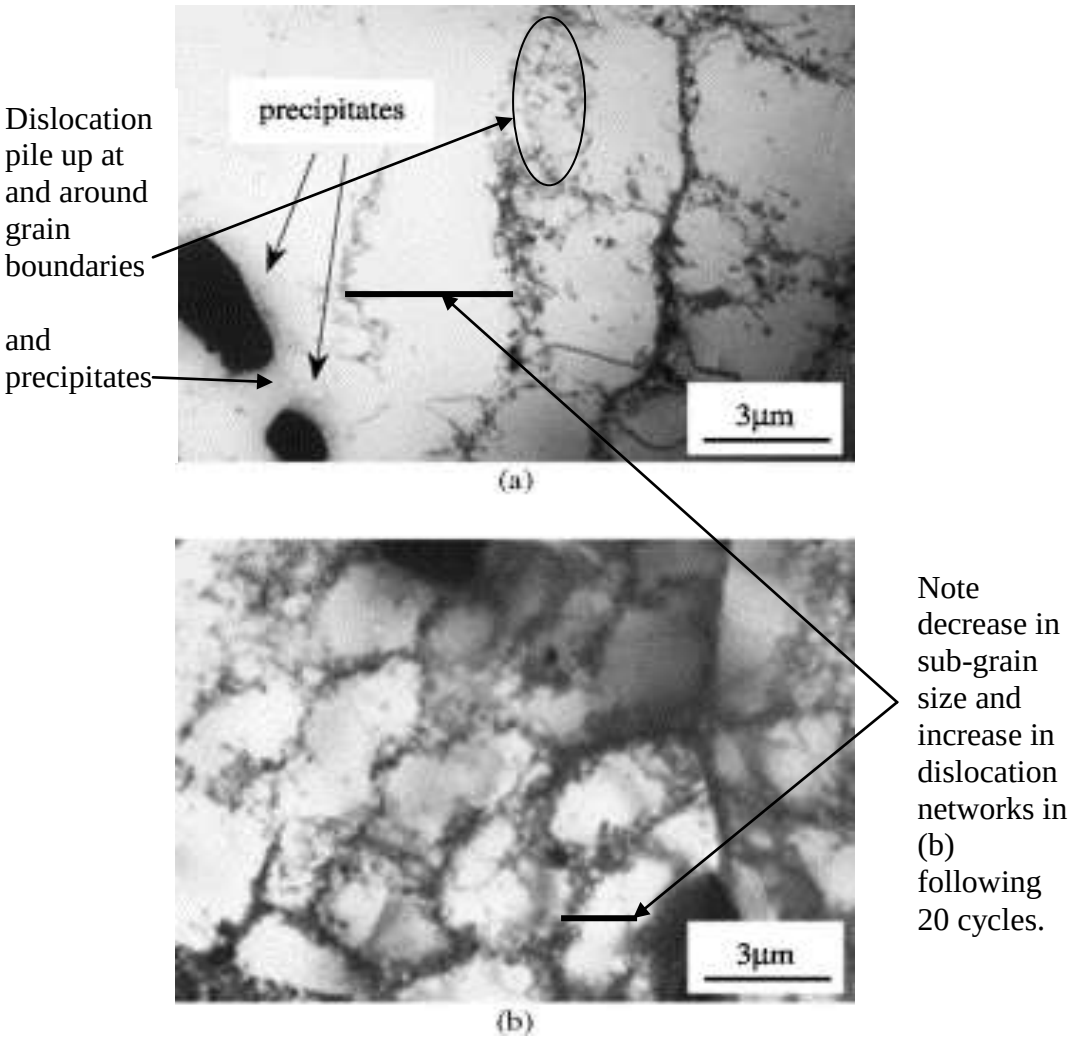

Figure 29 TEM electron micrograph of aluminium 6063 a) before, and b) after cyclic torsion, 20 cycles.

These results show that when the Bauschinger Effect occurs, there is possibly a net increase in stored energy within the material as suggested by dislocation density increases and sub-grain refinement. Within UC, the region that is affected can be referred to as the Deformation Affected Zone (DAZ) and its presence can be shown to exist through a detailed analysis of the reduction in sub-grain size and morphology around the bond interface. The governing equation for the stored energy, illustrating the influence of sub-grain size, is as follows:

$$E = \frac{\mu b^2}{10}\left[\rho_i\left(1-\ln\left(10b\rho_i^{1/2}\right)\right)+\frac{2\theta}{b\delta}\left(1-\ln\frac{\theta}{\theta_c}\right)\right] \text{----------[4.1]}^{68}$$

Where μ is the shear modulus, $\boldsymbol{b}$ is the Burgers vector, ρ_i is the internal dislocation density, θ is the sub-grain misorientation, θ_c is the critical sub-grain misorientation (typically 15º) and δ is the sub-boundary separation[69]. The primary focus of this work has been on careful measurement and exploration of the sub-grain and dislocation structures formed during the deformation phases of the UC process, which in turn influence the systems overall stored energy values. It is suggested that a significant decrease in sub-grain size per equation 4.1 would likely indicate an overall increase in stored energy as it would effectively marginalize the influence of the other variables in the equation.

A final critical point is important to stress before concluding this topic. It may be argued that the Bauschinger Effect cannot occur in the UC process as the UC process is not axial in nature. The vast majority of the Bauschinger literature is related to experiments that apply load in one then the other direction in a completely reversed way (ie. the exact opposite direction upon the original strain axis). Given that UC is a rolling process with the amplitude of motion perpendicular to the rolling direction, it is clear that no two cycles, however high of a frequency, or slow the rolling speed, follow the exact same path. Fortunately, there is growing evidence that this is not a requirement for the Bauschinger Effect to be at work[70].

An excellent example of this is discussed in a recent paper where the strain softening associated with the cyclic deformation of pre-strained metals was investigated[67]. In this study annealed and drawn 6063 aluminium alloy bars were subjected to cyclic torsion, instead of the more common cyclic axial deformation.

The structural aspects were analyzed and the author documented Bauschinger-like work softening that was believed to be caused by the restructuring of the dislocation arrangements due to the cyclic torsion. Additionally, the occurrence of deformation bands was shown to be associated with the subsequent mechanical behaviour of the material. Thus if the Bauschinger Effect progresses in the case of cyclic torsion, it is reasonable to assume that it may progress in the case of UC that is far closer to the classic axial conditions.

5. Hypothesis

Earlier studies on the effects of ultrasonic energy on metal joining resulted in a wide variety of mechanism theories noted earlier. These theories primarily attempted to explain the observed near instantaneous plastic flow state in ultrasonic welding from a macroscopic perspective and often contradicted one another. While a few of the theories attempted to associate the macro behaviour with micro dislocation mechanisms, none of the theories found in the literature explicitly explored the Bauschinger Effect, or cyclic softening, with sub-interface plasticity initiation and expansion. Another phrase that could be used to describe this region is the Deformation Affected Zone (DAZ). *The research hypothesis for this thesis was that there exists a non-thermal, cyclic-mechanical softening effect during the Ultrasonic Consolidation process that is the primary driver of interlaminar softening and solid state weld quality. This process occurs following initial oxide removal and frictional softening stages and is similar in character to the Bauschinger Effect. The hypothesis can be proven by microscopically analyzing UC samples for physical evidence that the Bauschinger Effect occurred and by ruling out thermal mechanisms as being solely responsible for the full extent of macroscopic interlaminar softening.*

The case for a Bauschinger Effect influence was driven in part by the fact that as early as 1960 it was noted that there existed a pronounced cyclic strain effect at sonic frequencies ("Langenecker Effect"). In these cases, there was reported to be an abrupt increase in the mechanical compliance of various materials when subjected to vibratory shear stresses[16]. Essentially, this hypothesis argued that these effects were one and the same. As discussed earlier, the Bauschinger Effect creates and utilizes dislocations within the matrix resulting in increased cyclic compliance, and thus the

previous, yet limited, observation of increased post-ultrasonic dislocation densities served as an additional key supporting element[71].

Additionally, there have been several recent unexplained physical observations within UC samples that seem to clearly point to a significant softening mechanism that cannot, at first analysis, be related to frictional heating or conventional metal forming mechanics alone. For example, there are common reports of material being "extruded out" of the interface during ultrasonic welding that are attributed to a highly plastic state of the material during the process[72].

More recently there has been a key physical observation using the UC process directly. The observation, reported by C. Yen at Loughborough University, relates to the embedding of very hard heterogeneous fibres between the layers during the UC process[38]. These results highlighted evidence of high degrees of plastic flow upon application of an aluminium layer on top of a copper layer with Sigma Fibres embedded in between. The copper substrate was selected to illustrate the pronounced flow effect due to its increased hardness over the aluminium. Results have repeatedly shown that high degrees of plastic flow are present, allowing the fibres to be fully encased (Figure 30). Further, these results would seemingly require interlaminar softness depths of at least 20-60 μm in order for such complete encasing and void filling to occur.

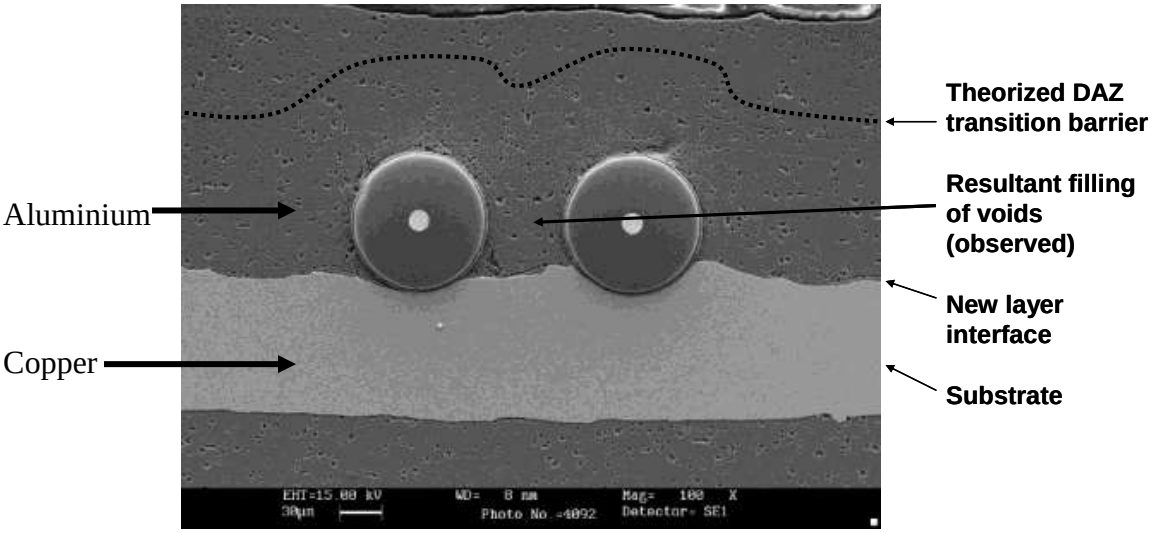

Figure 30 Embedded SiC fibres on top of a copper substrate within an aluminium matrix. A theoretical transition line of the DAZ in the Ultrasonic Consolidation process is shown above the embedded fibres.

If deep, sub-interface softening and plastic deformation was not occurring, it would be difficult to imagine how such complete encasing of these fibres would occur. Figure 31 shows the theorized case of where the flow propagation would end in the event there was only minimal sub-interface softening. In this illustration it is logical to assume that only minimal "filling" of the voids would be possible due to a largely rigid new foil layer that is experiencing only minimal sub-interface softening and deformation.

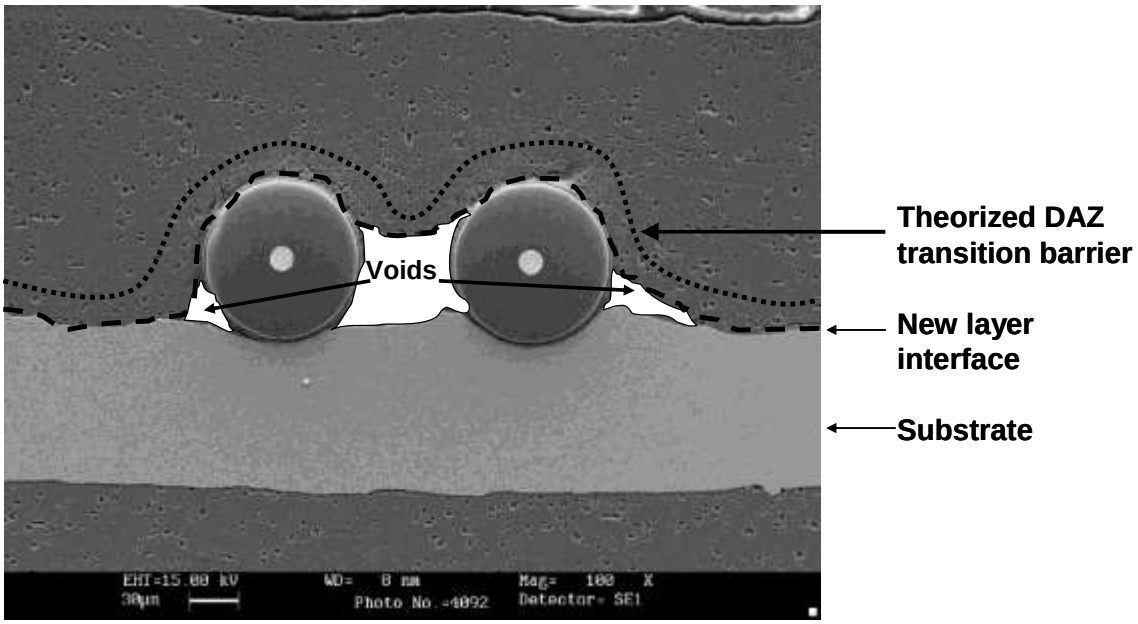

Figure 31 Theorized schematic of void creation in the case of 20 µm or less DAZ.

Secondly, additional experiments by C. Yen sought to observe the degree of plastic flow without an embedded fibre through the use of a substrate-based 150 µm etched pit. The expectation at the time of the experiment was that little of the added bonding foil layer would penetrate the pit, however, the results clearly demonstrated the presence of extremely high degrees of plastic flow, so much so that the entire 150 µm pit was essentially filled by the plastic deformation of both the new layer, and the substrate walls themselves (Figure 13). Additionally, the resultant void patterns within the pit seemed to be indicative of soft material movement, similar to what would be expected in an extrusion process with a very hot and ductile metal.

A key element to this hypothesis was that the Bauschinger Effect was believed to occur in regions ranging from mid asperity, to 2-60 µm below the asperity valley plane. Concurrent with initial oxide removal (5 nm in thickness,) the topmost regions would be plastically deformed or experience fretting via other deformation mechanisms in the initial UC cycles. Once sufficient contact area is achieved,

resulting in an increased coefficient of friction between the mating surfaces (and resultant adhesion and mild temperature increase,) the "cyclic tugging" beneath these fretted layers would begin to enable Bauschinger softening effects. These effects would progress well into the substrate layer up to approximately 40 μm deep depending upon initial surface texture and UC processing speeds.

When combined with the initial stages of surface oxide removal and frictional induced surface deformation, a theoretical propagation theory was put forth. The theory stated that interlaminar softening increases through three distinct stages:

- **Stage 1** – Oxide layer removal and near instantaneous fretting of the asperity peaks (5 nm depth)[73].
- **Stage 2** Rapidly increasing real area of contact, fretting, and resultant frictional heat generation, micro surface softening and local plastic deformation. This is also known as the stick-slip phenomena[74]. (1-6 μm in depth).
- **Stage 3 – (Core of Hypothesis):** Cyclic "volume effect" softening that propagates via dislocation transport deep below and above the bonding interface (2-60 μm). This region can be referred to as the DAZ and can be proven to exist through a detailed analysis of the gradient change in sub-grain size and morphology within the sample beneath the bond interface.

The graphical representation in Figure 32 presents the three softening stages of the propagation theory.

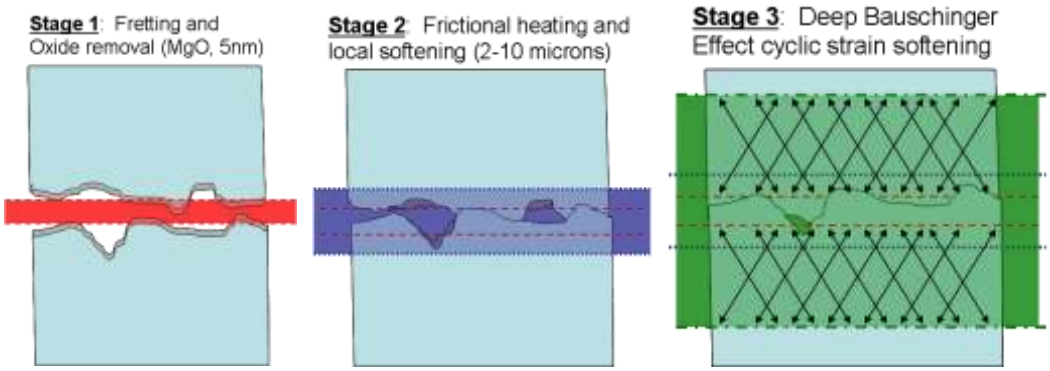

Figure 32 Theorized plastic deformation "stages" in UC process.

A key assumption was that the influence of each of the three stages is positively or negatively affected by the bulk material properties of the bonding materials and the processing parameters of the UC process. The following is a graphical representation of the three softening stages of the propagation theory as originally presented (Figure 33).

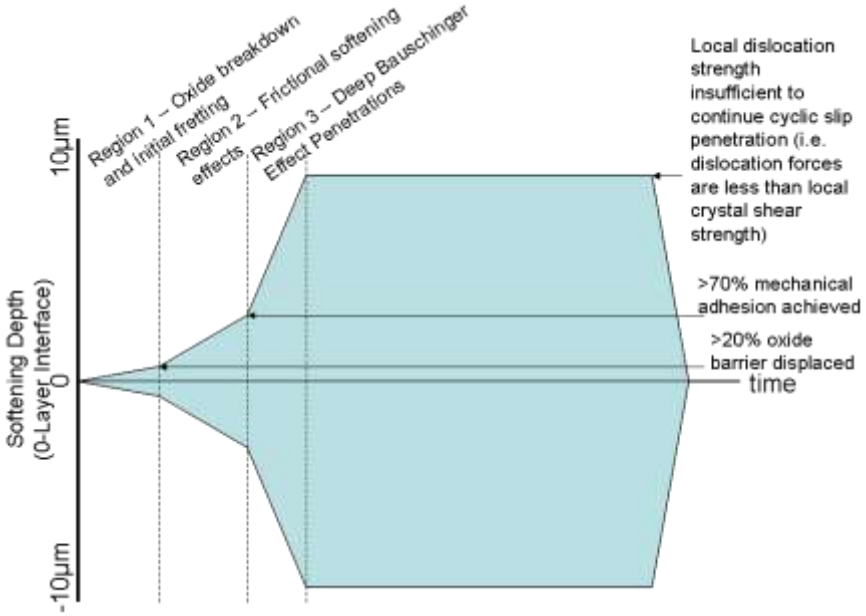

Figure 33 Time-state softening propagation during ultrasonic consolidation (typical surface roughness).

6. Experimental and Characterization Method

The core focus of this research was to prove the existence of a cyclic softening effect that propagates below and above the bonding interface (2-60 μm) following application of the UC additive manufacturing process. This region can be referred to as the UC induced DAZ and its existence could be shown through a detailed analysis of the change in sub-grain size within the lattice structure and by the presence of dislocation rich regions near the bond interface. If significant sub-grain refinement is present, the results would correlate with that of conventional Bauschinger-like cyclic softening research, indicating an overall cyclic-driven softening mechanism is at work within the UC process. Such results would also support the idea of an increase in stored energy within the entire system as a result of the ultrasonic cold work, another Bauschinger Effect attribute. The primary equation related to sub-grain size and its impact within the system is the equation for stored energy [4.1].

Thus the primary focus of the experimental method was on the careful characterization and comparison of the micro-structures formed during the deformation/weld phases of the UC process with those of Bauschinger tested samples. Simply stated, if there was shown to be either a quantifiable decrease in sub-grain size through a reduction in the sub-boundary separation (δ), or a quantifiable increase in dislocation density (ρ_i), then a change in stored energy would be proven. Such a change would confirm the UC induced cold work within the system and the extent of the cold work residual affect would define the size of the DAZ. If, in addition to this, the resultant sub-grain structure and general morphology showed a strong similarity to conventional Bauschinger tested samples, the basic tenants of the hypothesis would be advanced.

The experimental method to attempt to shed light on the nature and scope of the DAZ employed advanced and emerging materials science techniques at both the macroscopic and microscopic level. Specifically, new methods recently leveraged in the analysis of a similar DAZ regions related to the roll pass schedule within industrial rolling operations were utilized[75]. These studies were useful in establishing the rolling process effect on the stored energy within the material in a gradient fashion. And while the nature and material used in this research does not allow for a direct correlation with the research contained herein, the authors did conclude that there existed notable differences in the stored energy when the rolling was reversed in a cyclic fashion[76].

The three primary characterization tools that were utilized for this research included Scanning Electron Microscopy (SEM), a Dual Beam Focused Ion Beam (DBFIB) and Transmission Electron Microscopy (TEM). All of these methods were utilized in conjunction with multilayer UC laminate samples fabricated at Solidica, Inc. in the United States, as well as commercially produced foil that had not been processed by UC as a general material baseline. Each tool was used during this research for a specific segment of the characterization. The SEM was used primarily to assess macroscopic texture effects of the UC process while TEM microscopy was used to explore micro and nano-scale dislocation and sub-grain structure at known locations from the interface (utilizing in-situ lift out methods). Finally, the DBFIB, the primary tool utilized, was employed as an advanced etching method to quantify changes in the sub-grain size at known locations throughout a single foil thickness through a series of ion beam induced secondary electron micrographs.

The following experimental and characterization method progresses from a broad macroscopic assessment of the UC process to a high magnification microscopic

analysis. The macroscopic portion was designed to explore the potential impact of processing elements such as sonotrode texture on the overall system. These insights would then be correlated to the microscopic results to attempt to provide a more robust characterization of the mechanisms at work in the UC process.

6.1. Assess Macroscopic Effects of Sonotrode Texture

This task was designed to conduct transfer function experiments to determine how much of the sonotrode texture is transferred to a deposited material surface for a better understanding of interlaminar asperity formation. It is known that, following joining during layer-by-layer welding, the residual texture on the newly applied material has a certain asperity geometry associated with the sonotrode texture. The resulting asperity topography subsequently plays a likely role in the interlaminar bonding dynamics of the UC laminate. Further, this surface transfer can be drastically different with different materials and is generally related to the stiffness of the build and sonotrode materials. For example, the sonotrode may transfer nearly 100% of its surface texture to the aluminium material of focus in this research as aluminium's modulus and yield strength are very low as compared to the relatively hard titanium 6-4 sonotrode material. Two different engineered sonotrode textures were assessed for this task to provide a clear comparison of the results.

Conducting this task required 3 dimensional surface topography mapping software tools used in conjunction with optical and SEM microscopy. The key steps in this task were to:

1. Texture the surface of two different UC sonotrodes using both Electrical Discharge Machining (EDM) and Laser Etching (LE) methods.

2. Generate a 3 dimensional mapping of the sonotrode surface.
3. Weld a layer of new material utilizing the UC equipment with each of the engineered sonotrodes.
4. Generate a 3 dimensional mapping of the residual texture and calculate texture/asperity Ra values.
5. View the interface using SEM microscopy to determine macroscopic effect on interface region and interlaminar asperity formation.

6.1.1. Sonotrode Surface Preparation

This task involved the controlled surface modification of the contact area of the rolling sonotrode as shown in Figure 34. The intent was to create two distinct textures that would then in turn be used to fabricate UC samples with differing interlaminar properties. The two methods that were selected for this task included Electro Discharge Machining (EDM) and Laser Etching (LE). Due to the unique equipment required for this task the texturing treatment was conducted by external commercial vendors within their respective facilities. In both cases the specific texturing process that was used was deemed proprietary by the companies and thus the specific methods used were not disclosed to the author. Given the fact that the subsequent tasks in this section would begin with a 3D mapping of the surfaces to distinguish their topography as a starting point, it was not necessary to fully understand the texturing process itself.

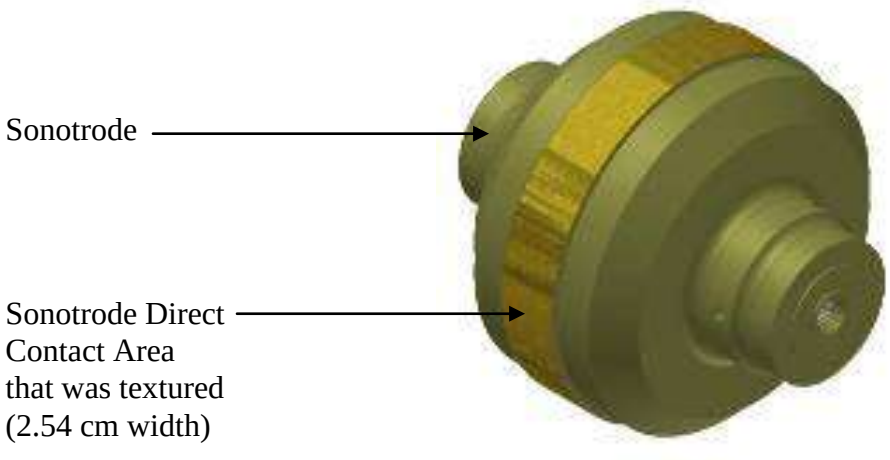

Figure 34 150mm diameter sonotrode used in UC system highlighting the sonotrode region (2.54 cm width) that is in direct contact with the UC laminate that was textured using EDM and laser etching methods.

6.1.2. 3D Mapping of Sonotrode Surfaces Using WYKO NT 8000

Once the EDM and the LE surface textures were established on the pair of test sonotrodes, the surfaces of both were scanned to calculate the Ra value. Due to the customized scanning apparatus necessary for this task, the sonotrodes were sent to an external commercial vendor to generate the scan data (Michigan Metrology Institute, USA). The system used for making the 3D measurements was a WYKO NT 8000[77] configured with a 5.1X objective system. The specific operational parameters that were used are listed in Table 3.

Table 3 WYKO NT 8000 scanning systems 5.1X objective system parameters

Measurement Attribute	**Nominal Value**
Magnification	5.1X
Measurement Array Size	640 x 480
Lateral Sampling	1.94 µm
Field of View	1.20 mm x 0.93mm
Height Resolution	<6nm
Terms Removed	Tilt/cylinder only
3D filter	Low Pass – Gaussian – 125 mm^{-1}
Stylus X λc/λs	1mm / 10 µm
Stylus Y λc/λs	0.8mm / 8µm
Stylus Filter Type	Gaussian

Figure 35 illustrates the orientation of the sample for measurement and the specific regions where the 3D scanning data was collected from the surface of the sonotrode. Note that measurements 1-3 are on the left edge, 4-6 are throughout the centre and 7-9 are on the right edge.

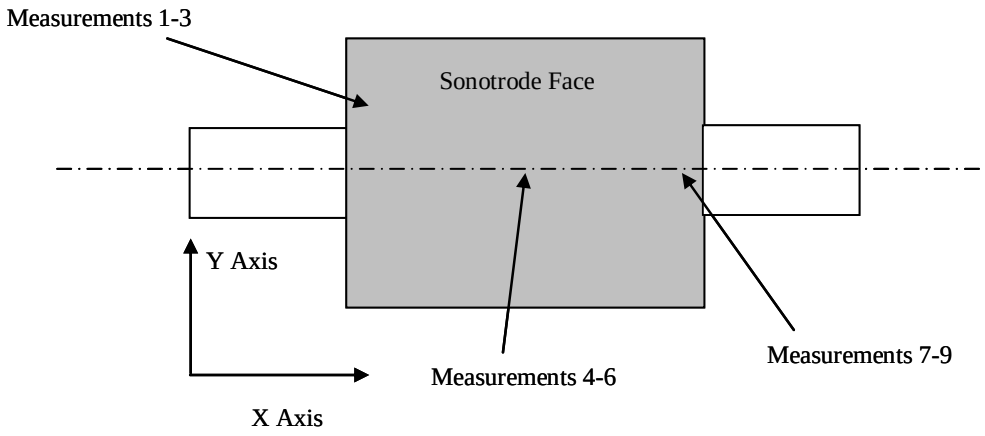

Figure 35 Locations of the 3D scanning regions used in calculating sonotrode surface texture (Ra) values.

The collected 3D data was then analyzed with WYKO Vision software (version 3.60). The 3D measurements of surface texture (Ra) correspond to measurements over the complete micrograph area of each sample region. The quantitative value for the sonotrode texture measurements were then specified as an average Ra value.

6.1.3. Optical Micrographs of Texture Imprint

Following the 3D mapping of the EDM and the LE sonotrode textures, several UC laminate stacks were produced from aluminium 3003 H13 foil with each of the sonotrodes to optically assess the texture imprint, or "transfer function" from the sonotrode surface to the top of the foil surface. The UC machine parameters that

were used for these samples were based upon the common parameters that are recommended by Solidica for the selected material and are identified in Table 4 (note that a pre weld "tacking" stage is necessary to hold the foil in place during the full weld cycle).

Table 4 UC weld parameters (at 149º C) for laminate samples used to determine sonotrode texture transfer.

	Force (N)	Amplitude (µm)	Feed rate (cm/min)
Weld	1400	19	254
Tack	300	16	254

Once micrographs were gathered from the top of the foil, an additional layer of tape was welded to each substrate to assess the impact of the transferred texture to the bottom of a smooth foil during subsequent bonding. Following the deposition of this additional foil a portion of the foil was removed and the underside of the foil was optically assessed.

6.1.4. SEM Electron Micrographs of Weld Cross Section

The final step in this segment of the research involved the cross sectioning of several multi-laminate samples to gather macroscopic evidence of the affect of the EDM and LE textures on the formation of voids at the interface. Standard SEM electron microscopy using equipment at the Loughborough Wolfson School of Mechanical and Manufacturing Engineering was utilized.

6.2. UC Sample Fabrication for DBFIB-etch and TEM Analysis

The focus of this task was on the fabrication of a UC aluminium stack sample to serve as the basis for the TEM and DBFIB-etch micrographs. The primary sample that was fabricated for this research was a three layer thick stack of aluminium 3003 T0, ultrasonically consolidated, utilizing the commercial Formation™ machine at Solidica facilities in Ann Arbor, MI utilising an EDM-etched sonotrode. The foil was commercially available aluminium 3003 T0 made in 2.5 cm width x 150 μm thick strips. Additionally, an unwelded, unrolled sample foil of commercially processed aluminium 3003 T0 foil was evaluated in parallel to establish a material baseline for comparison of the sub-grain size in the UC sample. The material composition of the aluminium 3003 T0 alloy that was used in this research is shown in Table 5.

Table 5 Chemical composition of aluminium 3003 T0

Aluminium	**Balance (at%)**
Copper	0.05 - 0.2
Iron	0.7 max
Manganese	1 - 1.5
Silicon	0.6 max
Zinc	0.1 max

3003 T0 aluminium was selected as the basis for this research in part due to the fact that it is the most widely used of all the aluminium alloys utilised in areas such as chemical plants, general sheet metal applications, cooking utensils, pressure vessels, garage doors, and heat exchangers. Importantly, the T0 treatment was ideal for a study of this nature as it removed most of the cold work that would have been

present in a non-annealed foil, such as the more commonly used aluminium 3003 H18. Aluminium 3003 T0 is an aluminium manganese alloy which increases the strength some 20% over the 1XXX grade. The presence of the manganese-containing particles also added additional insight into the focus of this research due to their theoretical ability to inhibit dislocation propagation. The following material characteristics for aluminium 3003 T0 are important to note:

- Aluminium 3003 is a non-heat treatable alloy and develops strengthening from cold working only. Thus the manganese remains as a separate particle and not a precipitate.
- Aluminium 3003 can be formed with a variety of common forming methods.
- Aluminium 3003 is easily machined.
- The hot working range is 200ºC (500F) to 510ºC (950F).
- Annealing is done at 413ºC (775F), followed by air cooling.
- At 24ºC (75F) the material properties of 3003-0 are:
    - Shear Modulus (G, μ) = 25.5 GPa
    - Shear strength for 0 temper = 75.8 MPa.
    - Tensile (ultimate) strength = 110MPa
    - Yield strength = 40MPa
    - Elongation = 30% (% in 50mm)
    - Brinell Hardness = 28
    - Density = 2.74×10^3 kg/m^3
    - Specific Gravity = 2.73
    - Melting Point = 643ºC (1190F)
    - Youngs Modulus (E) = 69 GPa
    - Poisson's ratio (υ) = 0.33

The UC processing parameters that were used in the fabrication of the three-layer aluminium 3003 T0 sample mirrored the current generally accepted commercial settings. The primary reason to utilise these common process values is due to the fact

that the focus of this research relates to the micromechanics of a typical weld and varying the parameters to abnormal levels may have produced unexplained anomalies in the sample. This would unnecessarily cast into question the utility of the results for the current UC user community. The exact UC processing parameters that were used are identified in Table 6.

Table 6 UC weld parameters (at 149° C) for laminate samples used in DBFIB, SEM, and TEM evaluation.

	Force (N)	Amplitude (μm)	Feed rate (cm/min)
Weld	1400	13	254
Tack	300	6	254

The basic fabrication approach and setup that was employed to make the three layer samples is illustrated in Figure 36.

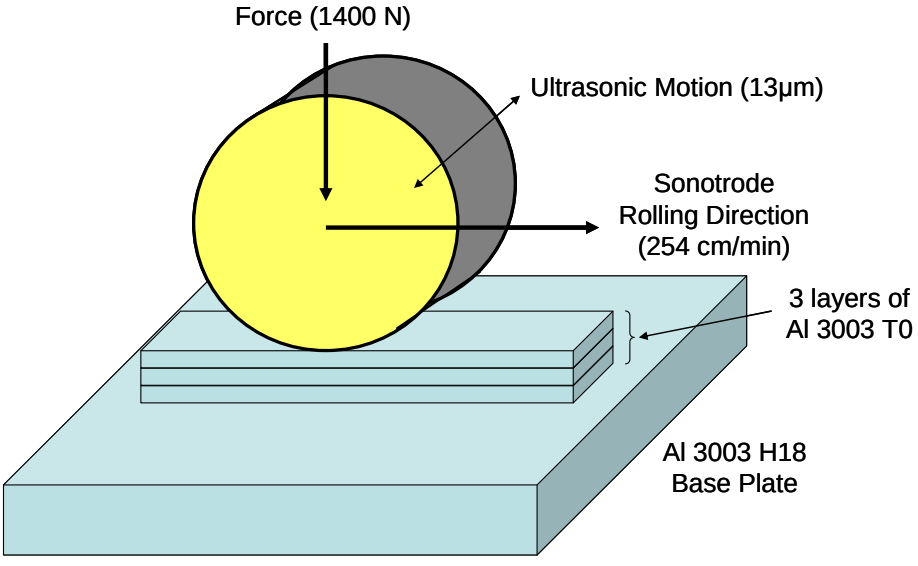

Figure 36 Illustration of the fabrication method of the 3 layer aluminium 3003 T0 UC stack that served as the basis for the microscopic analysis.

Following the fabrication of the three layer UC stack, the base plate was removed from the Formation™ machine and a small sample was cut away using a standard band saw. The samples were then further reduced in size to approximately 1.0 cm^3 and polished until an appropriate size and surface quality was reached for use in the DBFIB sample holding carriage. Due to the fact that there were only three full days between the fabrication of the sample and the analysis of the sample on the TEM and the DBFIB, and that the samples were kept at room temperature during this time, there are believed to be no aging issues that may have significantly influenced the analysis of the results.

6.3. DBFIB-etching of Primary Samples

6.3.1. Ion Beam Induced Secondary Electron Micrograph Capture

The DBFIB-etch process used to create the ion beam induced secondary electron micrographs represents a new material analysis technique that allows the user to generate a high quality material etch surface by utilising an ion beam to remove thin layers of the surface material. The key trait of this process that makes it an excellent etching and imaging tool is that the ion beam removes the surface material at different rates based upon the grain orientation of the sub-grains. The resulting variable rates of material removal can then be observed as different shades of grey when viewed, clearly identifying the presence and morphology of sub-grains within the sample of interest. Historically, such detail would only be viewable utilizing TEM microscopy. However, for certain materials (such as aluminium), the DBFIB-etch process provides clear sub-grain definition and yields far more micrographs than would be possible during the same period of time on TEM equipment. This time differential is simply due to the relative complexity of preparing a TEM specimen (1-2 hours per

specimen), versus the time to generate a comparable DBFIB-etch micrograph (10-20 minutes).

The ion beam induced secondary electron micrographs were generated in collaboration with the Materials Department at Loughborough University (IPTME) utilizing a Nova 600 NanoLab, UHR FEG-SEM/FIB machine (Figure 37). The Nova 600 NanoLab is a Dual Beam SEM / FIB for nano-scale prototyping, machining, characterization, and analysis of structures below 100nm. It combines ultra-high resolution field emission Scanning Electron Microscopy (SEM) and precise Dual Beam Focused Ion Beam (DBFIB) etch and deposition, the latter which was used specifically to create the ion beam induced secondary electron micrographs.

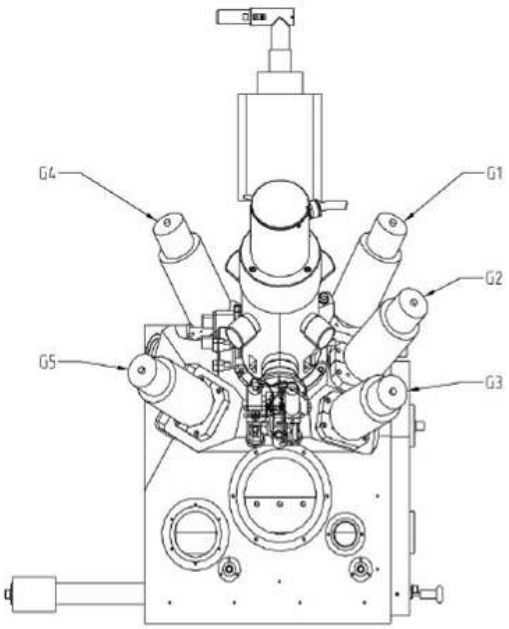

Figure 37 Nova 600 NanoLab, UHR FEG-SEM/FIB machine (courtesy of FEI Company™) used to create the ion beam induced secondary electron.

The ion beam induced secondary electron micrograph points were taken from the aluminium 3003 T0 stack in several carefully selected regions (Figure 38) using general DBFIB operating parameters of 50pA and a 90 second image acquisition time. The primary location in and around the second layer (shown as the "square of

squares") was selected to provide a high number of micrograph data points without potential "edge effects" that may be unique to the top, or bottom layer. The other two sample regions on the top foil and in between the bottom foil and the aluminium 3003 H18 base plate were subsequently taken to provide additional micrographs for comparative discussion related to the nature of any edge effects but were not essential for the proof of the hypothesis.

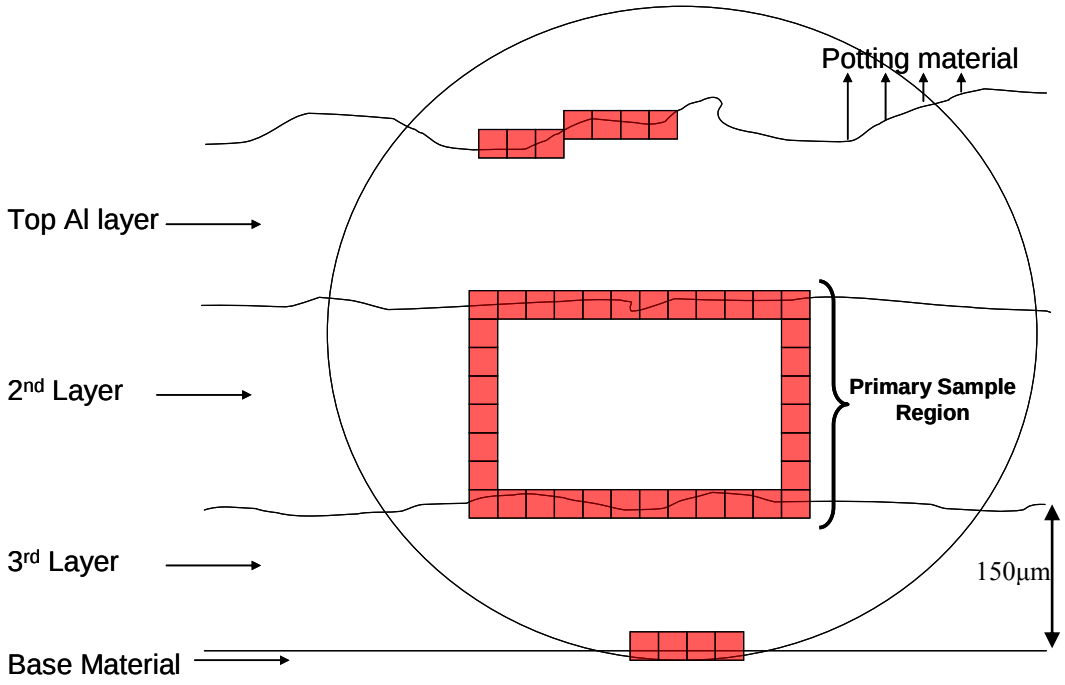

Figure 38 DBFIB-etch micrograph points for aluminium 3003 T0 sample.

The experimental effort focused on gathering a large number of ion beam induced secondary electron micrographs to characterize the sub-grain size distribution. The initial goal was to generate at least 36 quality micrographs and extract at least 6 grain analysis regions from each, for a total minimum sample set of 216. As noted, the primary benefit of utilizing the DBFIB-etch method as opposed to the TEM was that a much higher number of micrograph samples could be collected when compared to the relative few that would have been gathered using TEM alone.

For every one TEM micrograph that would have been usable in calculating sub-grain size, 5-10 ion beam induced secondary electron micrographs could presumably be analyzed to calculate a more precise sample characterisation.

6.3.2. Calculation of Average Sub-grain Size

Sub-grain size sample data was then calculated using the mean linear intercept method in nearly all of the ion beam induced secondary electron micrographs from the primary sample region (in and around the second foil layer). The mean linear intercept method provides an estimated average size within a group of sub-grains for a given sample (discussed further below). The general equation that was utilized for the calculation of the average distance between grain boundaries was as follows:

$$\bar{L} = \frac{\sum L}{M \times \sum x} \quad \text{----------[6.1]}^{78}$$

Where $\sum L$ is the total length of the traverses and M is the magnification and $\sum x$ is the sum of the intercept points. For this research a circle was utilized as a single traverse instead of linear traverses due to the presence of nano-grain colonies. If linear traverses had been used, the traverse would cross both regular sub-grains and nano-grain regions alike, resulting in potentially confusing results (ie. if a linear intercept happened to cross a nano-grain region it would easily multiply the number of intercepts by a factor of 5, skewing the results for the entire region). Utilising a circular traverse allowed for the isolation and quantification of the nano-grain regions and resulted in a more useful analysis. Thus, the traverse length was equal to the circumference of the circles that were used. The intercept points were counted as all of the specific points at which a sub-grain boundary crossed the circular traverse.

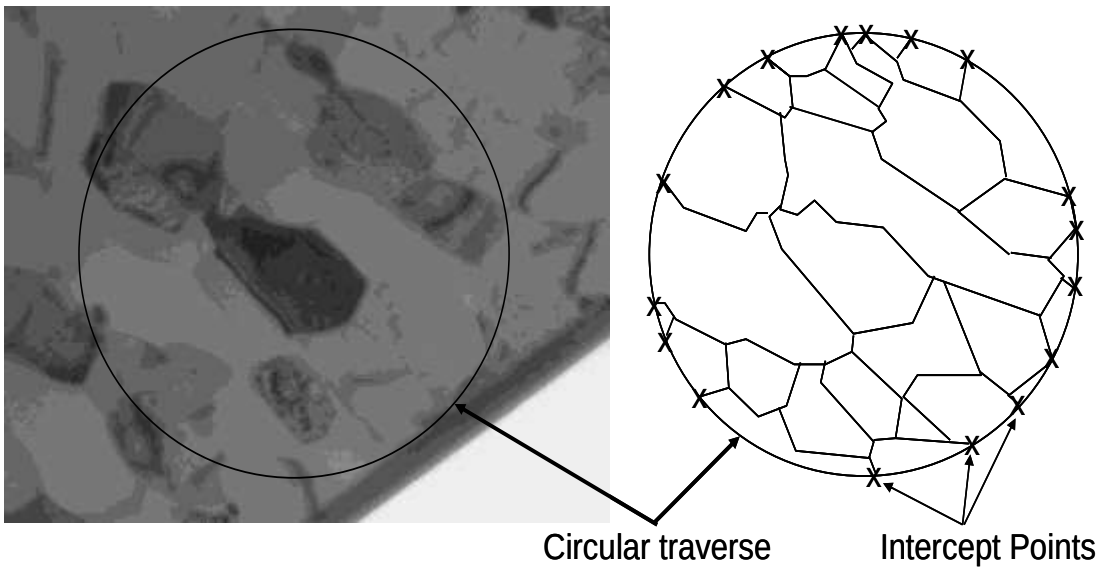

Figure 39 Illustration of the linear intercept method utilizing circular traverses. The "x" marks represent the intercept points where a grain boundary crossed the traverse line.

The circle diameter that was used for all of the sample regions was 25 mm (following printing of the micrographs in their full resolution on separate individual pages of A4 paper). This diameter was chosen due to the fact that it provided adequate grain boundary intersection data points, necessary for the calculations. The magnification was 8000x throughout all of the ion beam induced secondary electron micrographs used in the sub-grain size analysis.

Sub-grain sizes were then averaged for eight different regions defined by their general proximity to the interface and whether or not they were taken directly from a nano-grain colony. The average and standard deviation of all of the samples were then calculated and graphically plotted. The eight sampling regions are identified in Figure 40.

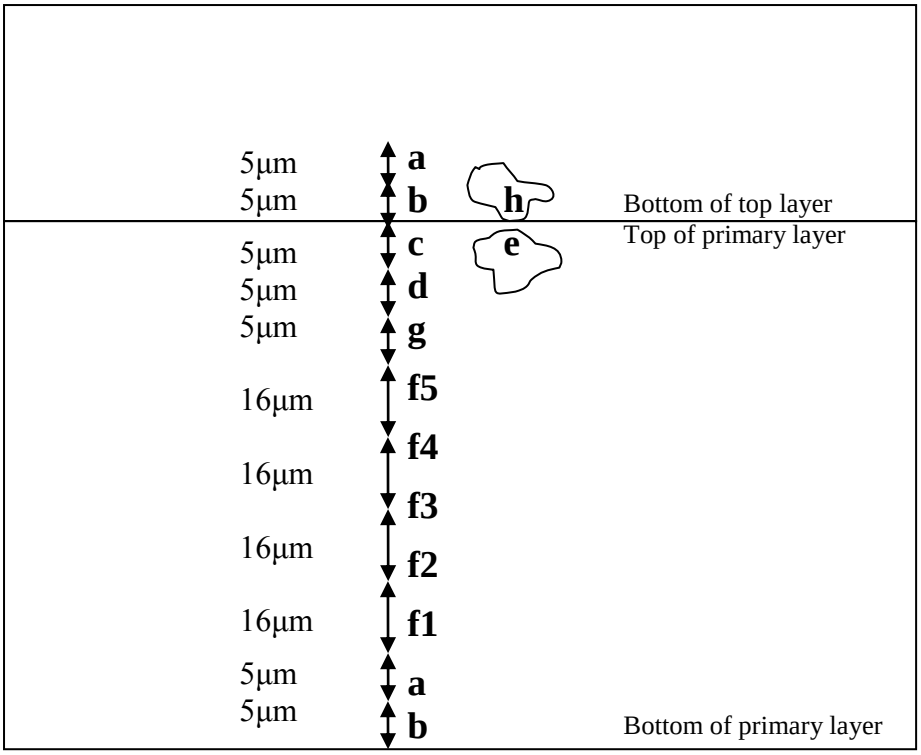

Figure 40 Sub-grain size sample region identification. The primary layer represents the second layer of the three-layer UC laminate stack.

- Region a – ~ 5-10 µm on top of interface
- Region b – ~ 0-5 µm on top of interface
- Region c – ~ 0-5 µm below interface
- Region d – ~ 5-10 µm below interface
- Region g – ~ 10-15µm below interface
- Region f1-f5 – ~ 16µm regions through the foil middle section
- Region e – nano-grained region below interface
- Region h – nano-grained region above interface

Multiple sub-grain measurements were taken where possible within each of these regions to maximise the overall sample set. Care was taken to not have the same sub-grain be used in more than one linear intercept imaging region. A schematic of the sampling method is shown in Figure 41.

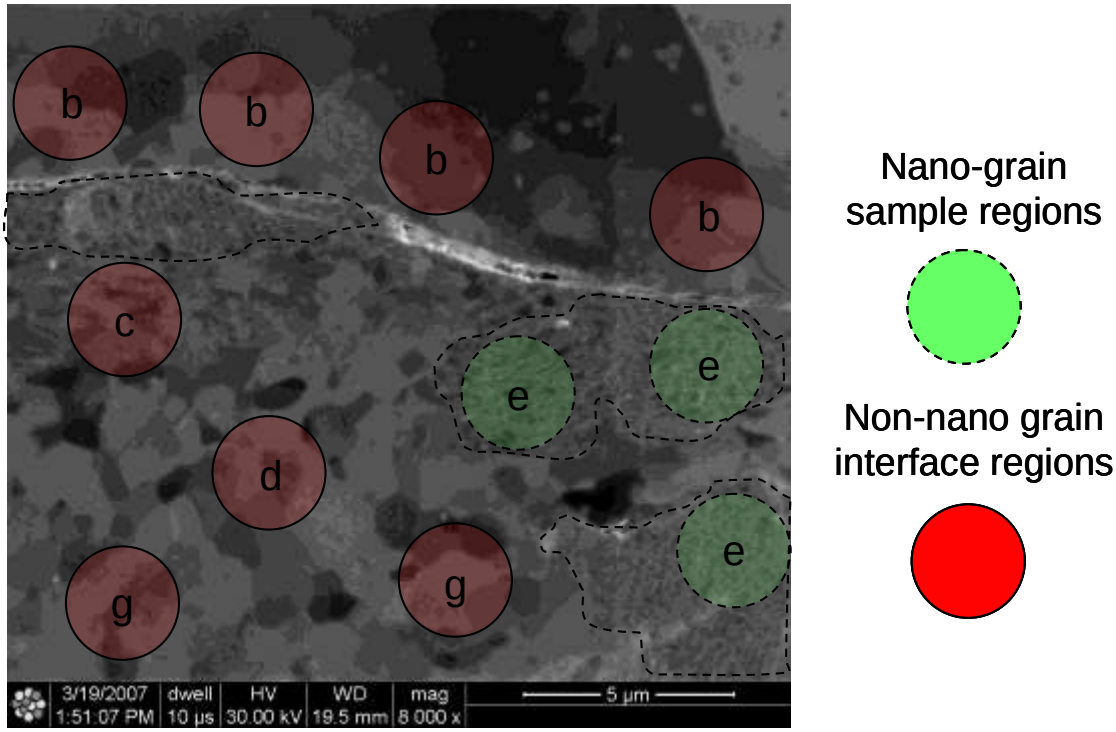

Figure 41 Sub-grain size calculation sample method illustrating general selection method of regions of interest within a known proximity to the interface.

6.3.3. Calculation of 95% Confidence Limit

Next the 95% confidence limit for each of the regions was calculated to provide a statistical confidence perspective on the results. The standard error of the sample mean ($S(\bar{x})$) is related to the standard deviation of the various regions as follows:

$$S(\bar{x}) = t_c \frac{s}{\sqrt{n}} \quad \text{----------[6.2]}^{78}$$

Where t_c is the t value for the 95% confidence limit (a function of the number of degrees of freedom), s is the standard deviation for the sample set and n is the total samples taken within a regional group.

Finally, for use as a general visual comparison, several DBFIB-etch micrograph samples were then also taken from the very top and the very bottom of the three layer stack. These micrographs were analyzed to ensure there were no unique

edge effects that may be of interest to the understanding of the general research results.

6.3.4. DBFIB-etch Combined with High Magnification SEM

Finally, additional SEM electron micrographs were then gathered from the primary sample using a combination of DBFIB-etching and standard, high magnification SEM microscopy to attempt to further characterize the sub-grain and nano-grain transitional regions within close proximity to the selected region. These micrographs were taken on an excavated plane that was perpendicular to the orientation of all of the previous ion beam induced secondary electron micrographs. This new orientation was attempted as it was determined that the excavated surface would possibly etch better, which would be critical to successfully capture a higher magnification view of the nano-grain regions. The reason for this is that the surface on the top of the sample, etched manually using conventional surface etching methods prior to placement into the DBFIB, decays more rapidly under the ion beam etching (as it had already undergone significant etching during the manual polishing process). These multiple etching stages limit the potential micrograph resolution that can be achieved due to a higher delta in the etched "peaks" and "valleys". While this was not a problem in generating the ion beam induced secondary electron micrographs necessary to do the primary sub-grain size analysis, it was preventing potentially useful higher resolution micrographs of the nano-grained regions themselves.

It was found that high quality SEM electron micrographs of these regions could be generated through the process of excavating a 5.0 μm "pit" using the DBFIB, and then etching a cross section of the sample within this pit (which would be

perpendicular to the previous ion beam induced secondary electron micrographs). This approached is illustrated in Figure 42.

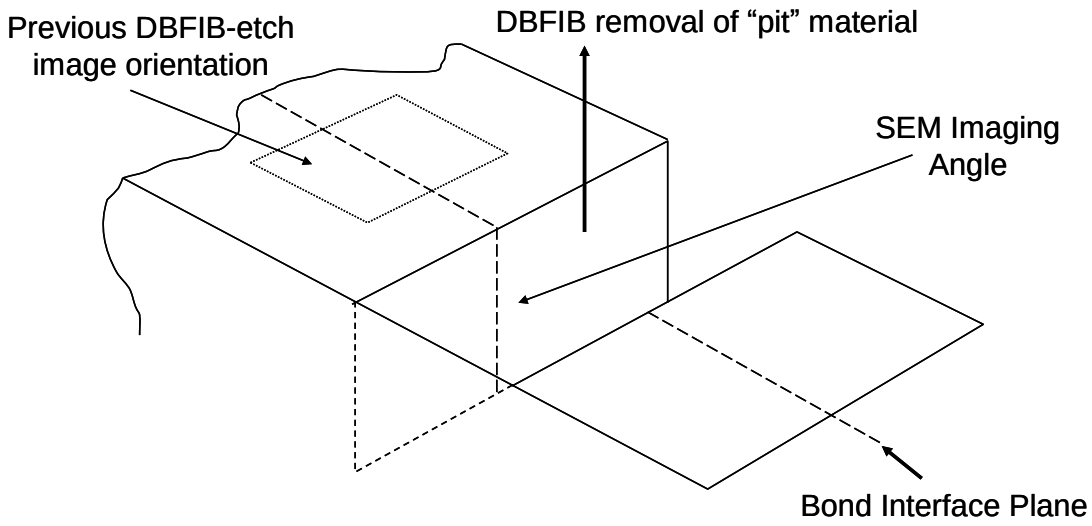

Figure 42 Illustration of DBFIB etching and subsequent SEM electron micrograph generation taken perpendicular to primary ion beam induced secondary electron micrographs.

Following etching, several high magnification SEM electron micrographs were taken of the area.

6.4. DBFIB-etching of Engineered Mating-Surface Regions.

To provide further comparative date with the results from Section 6.3, and to further explore the initial foil interface texture effects on the sub-grain size, four additional UC interface regions were prepared and ion beam induced secondary electron micrographs were generated and then analyzed. The purpose of these additional micrographs was not only to confirm the relevance of the primary sample region, but it was also useful to assess at a high level, the effect of variable interface roughness. Understanding this would allow for a much broader understanding of the results as they would shed light on many of the most common interface conditions that are

experienced by practitioners of the UC process. The process steps for these supplemental samples were as follows.

1) Weld a single 15 cm-20 cm strip of aluminium 3003 T0 tape to a 3003 H18 base plate. This initial foil layer would then serve as the substrate for the sample region as the H18 base plate would have potentially altered the results due to the material property differences and edge effects.
2) Next, the top of the first layer was "flat passed" with the Formation™ CNC 3-axis milling centre to remove residual sonotrode texture marks and the entire DAZ from the deposition of the first layer (~20 μm were removed to accomplish this). Note that this step also replaced the rather robust oxide layer of the as-rolled material with a much thinner oxide layer (that would immediately form once the top material was removed but not be fully ingrained as the commercial oxide layer would have been).
3) Then, the top of the new flat passed layer was plastically deformed through mechanical means in four different sample regions, each with its own unique surface topology. The four modified regions were as follows:
    a. 2.54 cm^2 section that was highly polished by hand to a 1 μm finish.
    b. 2.54 cm^2 section that had its surface rolled with the sonotrode at the normal rolling force (500N) without the ultrasonics engaged to create a texture similar to normal operating conditions, yet without any cyclic ultrasonic forces.
    c. 2.54 cm^2 section "trough" in a generally consistent linear direction parallel to the motion of the ultrasonic vibration of the sonotrode. The parallel "trenches" were ~3 - 5.0 μm in depth.

d. 2.54 cm^2 section "trough" in a generally consistent linear direction perpendicular to the motion of the ultrasonic vibration of the sonotrode. Again, the perpendicular "trenches" were ~3 - 5.0 μm in depth.

4) Next, the preceding patterns were repeated on the bottom of a new foil (so that they would line up to the corresponding texture on the new substrate layer). This new foil layer was then welded to the previously textured substrate, becoming the second layer of the sample. Note that it was not possible to flat pass the bottom of the second foil layer due to the fact that it could not adequately be clamped to accomplish this. The processing parameters for both layers were again that presented in Table 6.
5) The base plate was then removed from the Formation™ machine and the sample, with its four engineered texture regions, was cut away from the rest of the base plate.
6) A small sample region was then selected from each of the four sections, roughly from the middle of each texture region to ensure there were no edge effects.
7) Finally, a series of ion beam induced secondary electron micrographs were taken and the results were analysed.

Figure 43 and Figure 44 illustrate the basic experimental procedure that was used in the preparation of these samples.

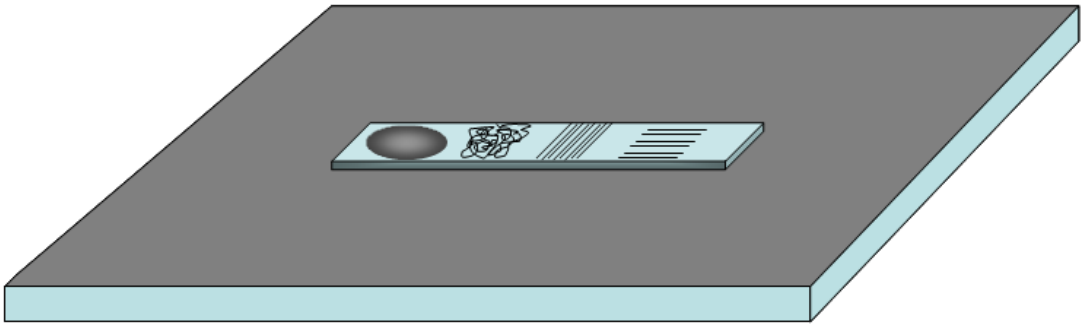

Figure 43 Initial substrate surface modification following deposition of first UC tape layer.

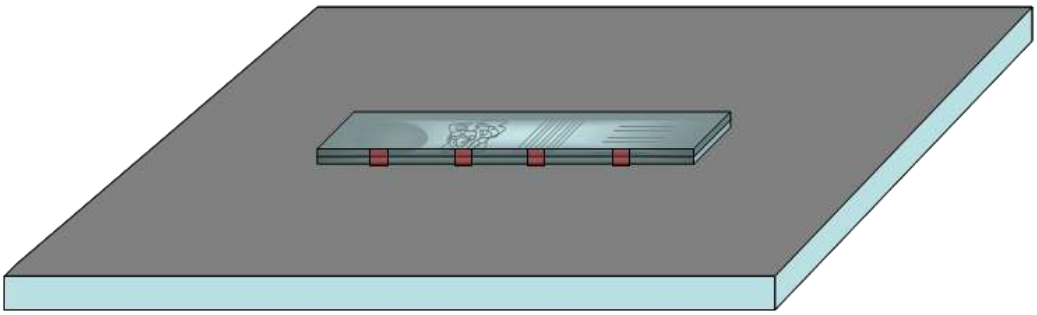

Figure 44 Ion beam induced secondary electron micrograph regions (in red) following deposition of second UC tape layer.

6.5. TEM Electron Micrograph Production

The final step was to generate and analyze a series of TEM electron micrographs in and around the interface at known locations. The focus was on assessing the micrographs to determine if there were any clearly identifiable dislocations present and/or to confirm consistent sub-grain morphology to that seen using the DBFIB.

The TEM sample and micrographs were also generated in collaboration with the Materials Department at Loughborough University (IPTME), once again utilizing the Nova 600 NanoLab, UHR FEG-SEM/FIB machine. The Nova 600 was employed to perform an in-situ lift out procedure to generate the TEM electron micrograph

samples. The in-situ lift out procedure is able to extract an ideal TEM sample geometry of approximately 20.0 μm x 0.5 μm x 4.0 μm.

The Nova 600 has a minimum etched line width of 15.0 nm and a maximum hole aspect ratio of 10:1. One can think of the 15 nm line width as the width of the "cutting tool", or etching removal "spot size". So for example, the extraction process described below extracts a 1.0 μm thick sample, which to be usable on a TEM must be additionally thinned to a thickness of less than 500 nm. Thus the DBFIB is further used to "scan remove" 15 nm layers away from the 1.0 μm thick sample in a raster fashion to end up with the necessary 500 nm thick sample (in this case between 30 and 40 passes would be required). The final net geometry of the TEM sample extraction point is then approximately 20.0 μm x 0.5 μm x 4.0 μm. An illustration of a TEM sample extraction point is shown in Figure 45.

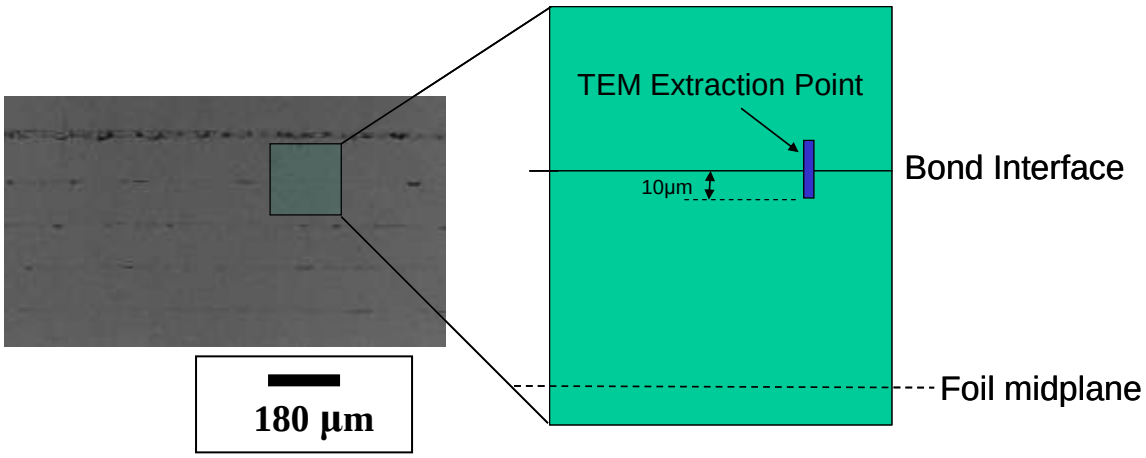

Figure 45 Illustration of an initial TEM extraction point selection.

There were several key steps that were necessary in the fabrication of the TEM samples using the DBFIB. Care had to be taken throughout the steps to ensure

that the extraction process itself did not introduce any noticeable dislocation affects. The primary steps that were employed are outlined in the following sections.

6.5.1.1. Extraction Site Location Selection

For this step a location that did not appear to be within close proximity to any interlaminar voids or other major defects was selected. Figure 46 demonstrates such a region. The primary reason for this was to avoid an area specifically flawed by a manganese particle or other abnormal defect at the interface. However, if a small to moderate void was believed to be a natural occurrence between aluminium interfaces alone, the sample would be deemed acceptable.

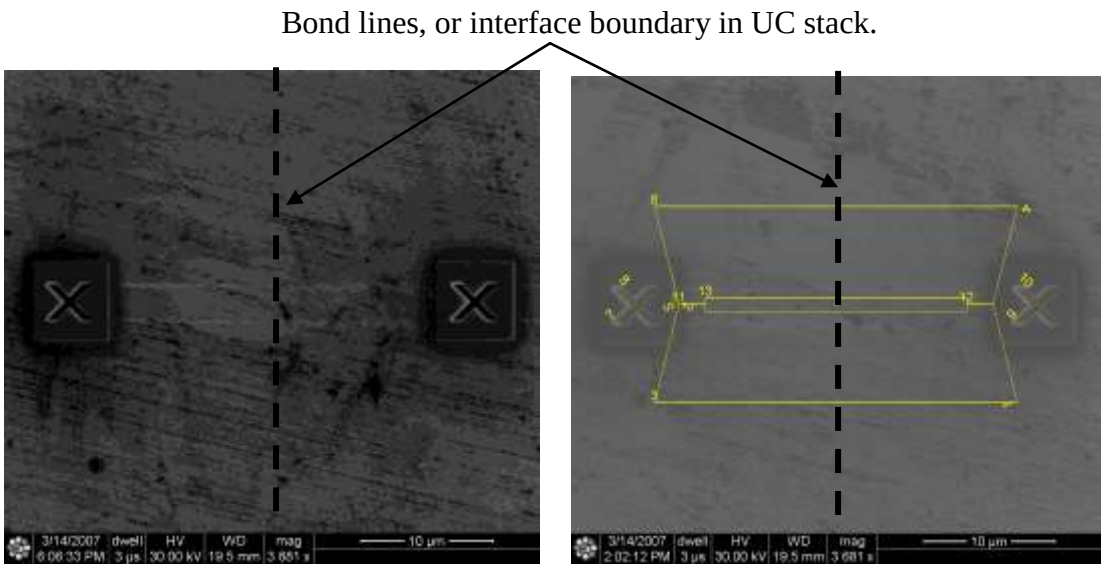

Figure 46 Sample region for DBFIB in-situ extraction showing no obvious voids or second phase particles. The yellow guidelines outlined the basic region to be excavated around the sample area, the dashed line represents the bond line between two layers in the UC stack.

6.5.1.2. DBFIB Mapping to Extraction Locations

The location that was selected as the extraction point was then "mapped" into the NanoLab software so that the automated material removal program could progress (Figure 47). This graphical user interface allowed for the straightforward viewing of the sample using either the SEM or the FIB.

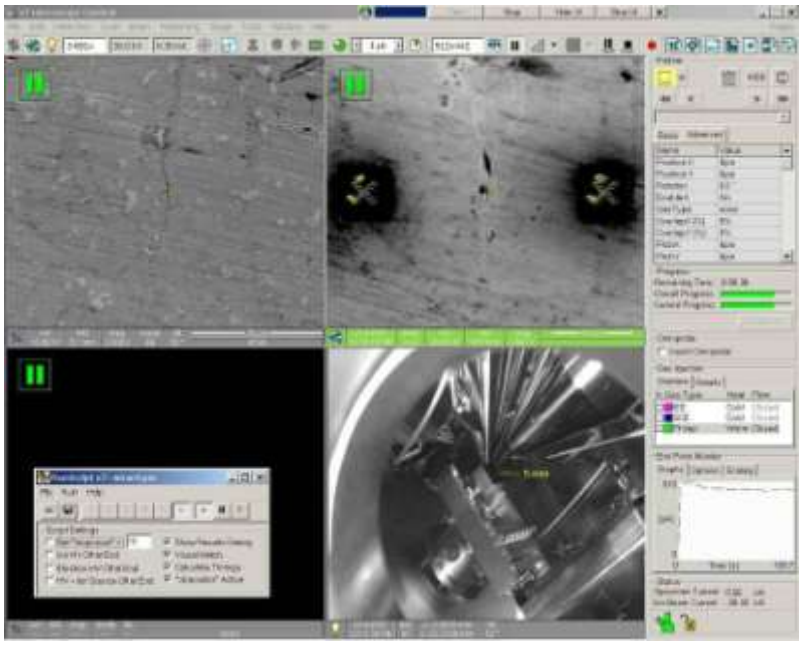

Figure 47 DBFIB/SEM user interface.

6.5.1.3. Automated DBFIB Etching Material Removal

The surrounding material near the chosen sample location was then removed using the iterative DBFIB-etch removal method described earlier (Figure 48). This process had to be monitored to ensure the sample would not be damaged or overly thinned at any point during the excavation process.

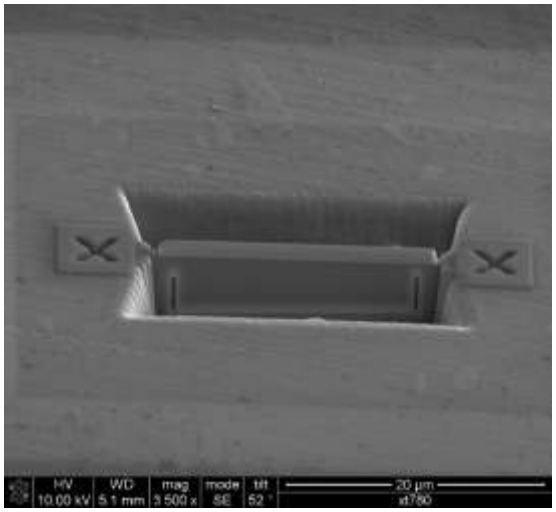

Figure 48 Sample following surrounding material removal.

6.5.1.4. Removal of Sample and Placement onto TEM Grid

The next step was the removal of the sample from the excavated pit and its subsequent placement onto a copper TEM mounting grid (Figure 49 and Figure 50). This stage required the micro-welding of the sample to a tungsten probe using a platinum weld and then the subsequent welding of the sample to the copper TEM grid, followed by the cutting of the weld bead to release it from the probe.

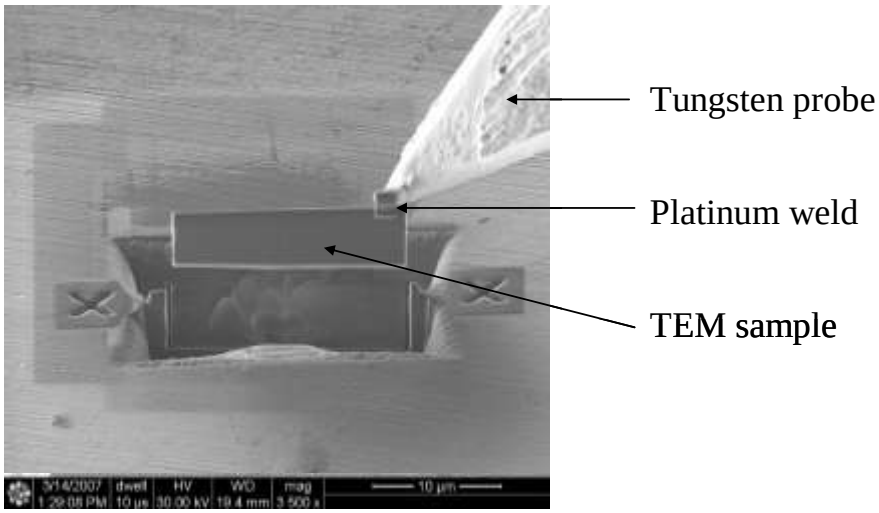

Figure 49 FIB extraction of TEM sample from UC laminate interface region from aluminium 3003 T0 sample.

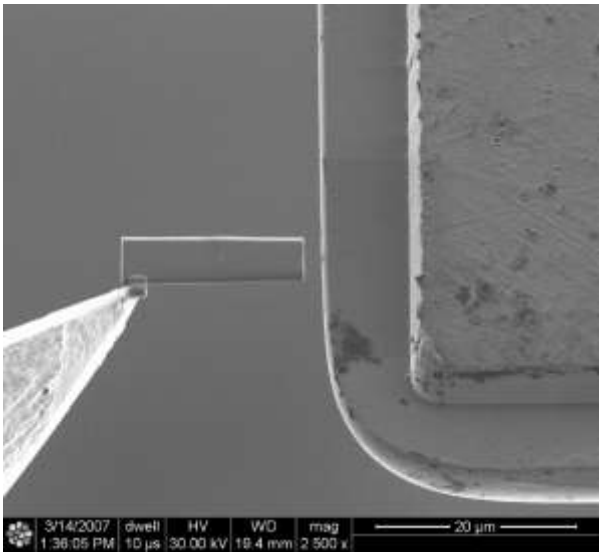

Figure 50 Placement of TEM sample extracted from UC laminate onto copper TEM sample grid fixture.

6.5.1.5. Final Sample Thinning and Transfer to TEM Machine

Once the sample was mounted to the copper TEM sample grid fixture it was iteratively thinned with the DBFIB from an initial thickness of 1.0 μm to an approximate final thickness of 0.4 μm (Figure 51). Ideally the sample would be thinned even further (as 0.4 μm is generally the maximum thickness desired for TEM imaging), however, the UC interface sample began to slightly bend at around 0.4 μm, possibly due to the high degree of internal stresses inherent within the UC deposition process. Fortunately, aluminium samples lend themselves well to TEM microscopy and a sample of this thickness was fully acceptable.

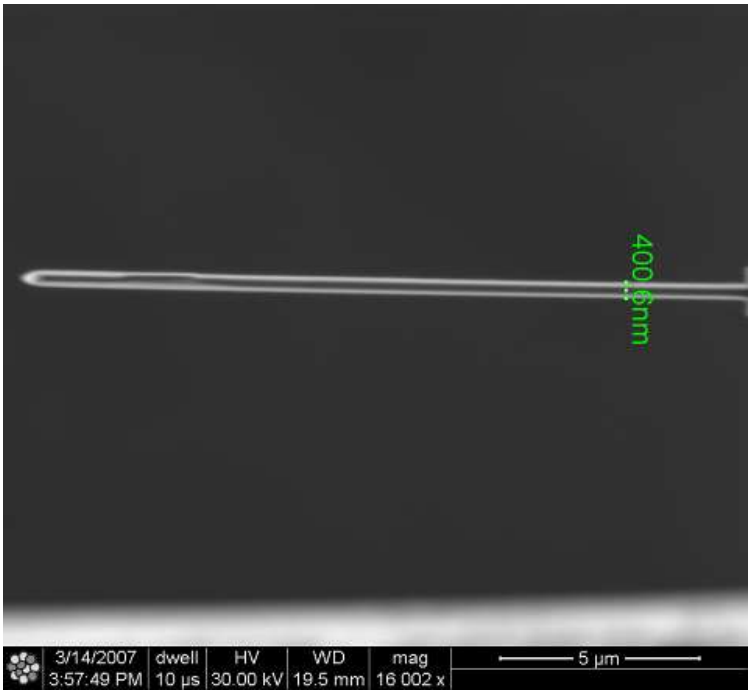

Figure 51 Cross section view of the TEM sample following thinning with the DBFIB.

Once the TEM sample preparation was complete, it was then carefully transported to the Loughborough University TEM machine within IPTME and a series of high resolution TEM micrographs were generated and analyzed.

7. Results

7.1. Macroscopic Effects of Sonotrode Texture

7.1.1. Sonotrode Surface Preparation

Two sonotrodes were successfully textured utilizing both Electro Discharge Machining (EDM) and Laser Etching (LE) approaches. The LE textured sonotrode was produced first and is shown in Figure 52.

Figure 52 Photograph of surface texture produced by laser etching. The textured area is 2.54 cm in width.

The EDM textured sonotrode was produced next and is shown in Figure 53.

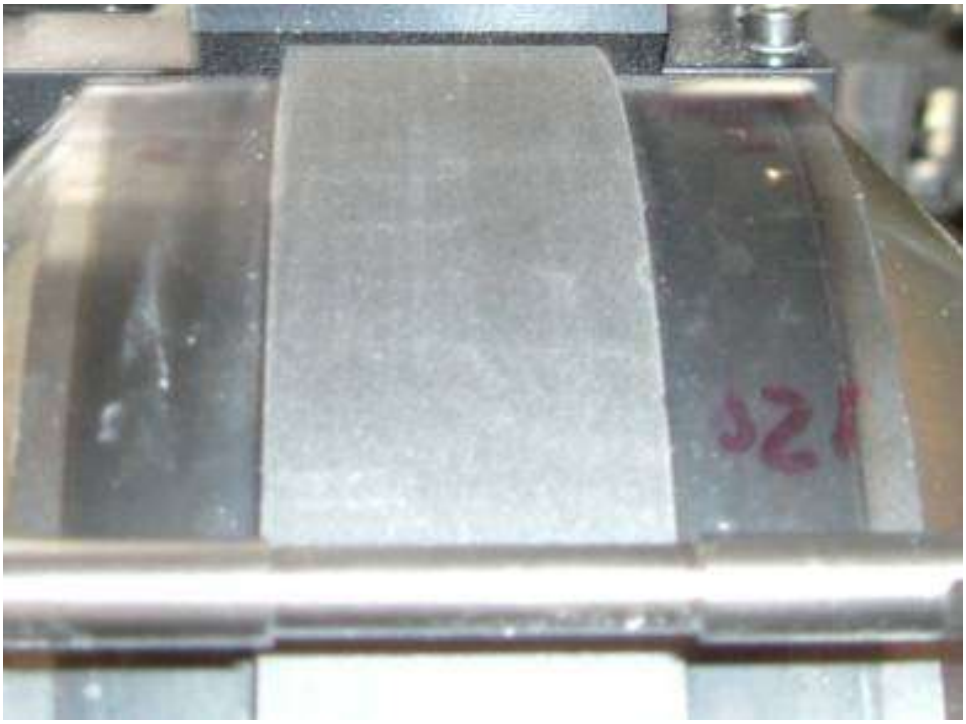

Figure 53 Photograph of surface texture produced by electro-discharge machining. The textured area is 2.54 cm in width.

7.1.2. 3D Mapping of Sonotrode Surfaces Using WYKO NT 8000

Both the EDM and LE textured sonotrodes were successfully digitally 3D mapped utilizing the WYKO NT 8000 system. Following the generation of the data, Ra factors quantifying the average surface roughness were outputted by the WYKO Vision software as shown in Table 7.

Table 7 Ra values for as-rolled foil, sonotrode with laser etched (LE) surface, and sonotrode with EDM etched surface.

	As-Rolled Foil	LE	EDM
Ra	0.08	6.27	2.52

A visual inspection of the digital 3D texture image of the LE surface showed highly pronounced topology features resulting in a Ra value over twice that of the

EDM textured sonotrode. A sample image taken from the LE sonotrode is shown in Figure 54.

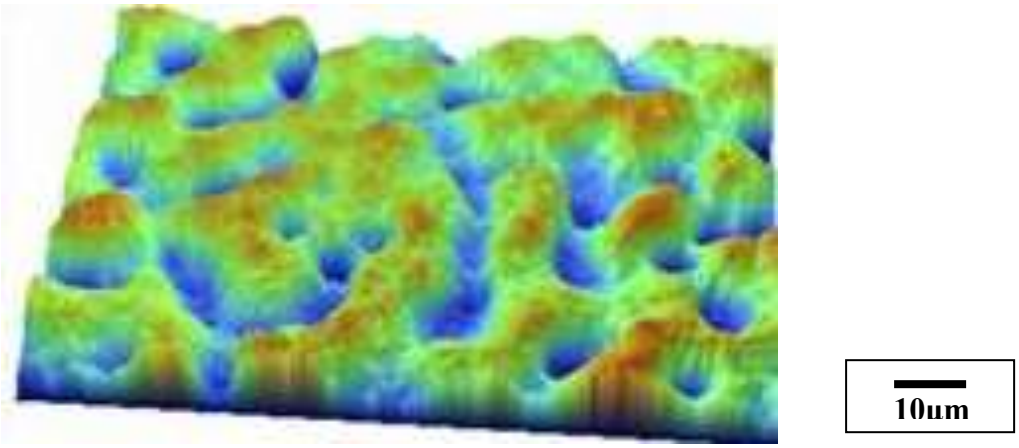

Figure 54 3D imaged taken of sonotrode with a texture generated by laser etching (LE).

The results for the EDM textured sonotrode were far different than that of the LE sample. The EDM 3D image results appeared to be both of greater consistency, and the topography "peaks" and "valleys" were clearly less pronounced, leading to a far smaller Ra value. A sample digital 3D image taken from the EDM sonotrode is presented in Figure 55.

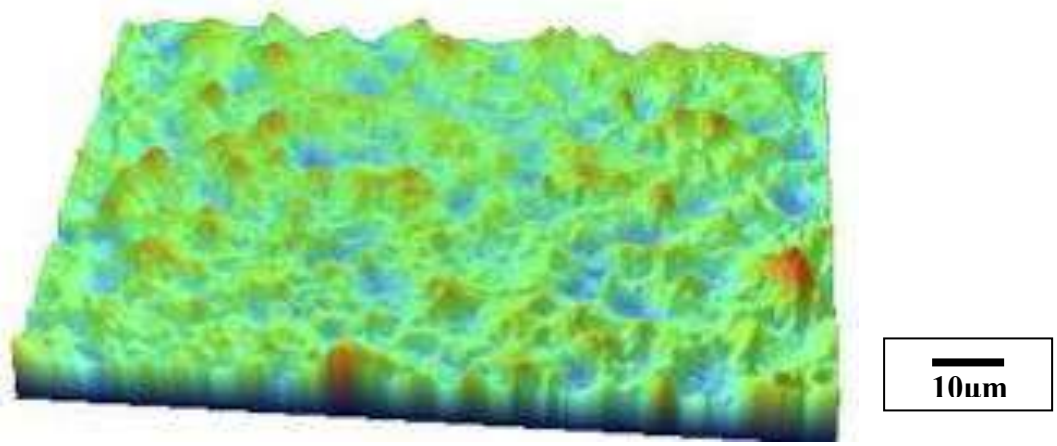

Figure 55 3D imaged taken from sonotrode with a texture generated by EDM.

7.1.3. Optical Micrographs of Texture Imprint

Transfer function experiments were carried out to determine how much of the sonotrode texture is transferred to a new deposited foil surface. It is well known by UC practitioners that, following joining during layer-by-layer welding; the residual texture on the newly applied material has a certain geometry associated with the residual of the sonotrode texture and these results provide direct quantifiable evidence of this perception.

The black regions in Figure 56 identifies that portion of the foil surface which has been plastically deformed by the sonotrode texture. The blue (or light) region in between has been unaffected. These areas are essentially untouched foil that stands higher than the black regions and would probably be the first region that would come into contact with the subsequent foil layer during ultrasonic welding.

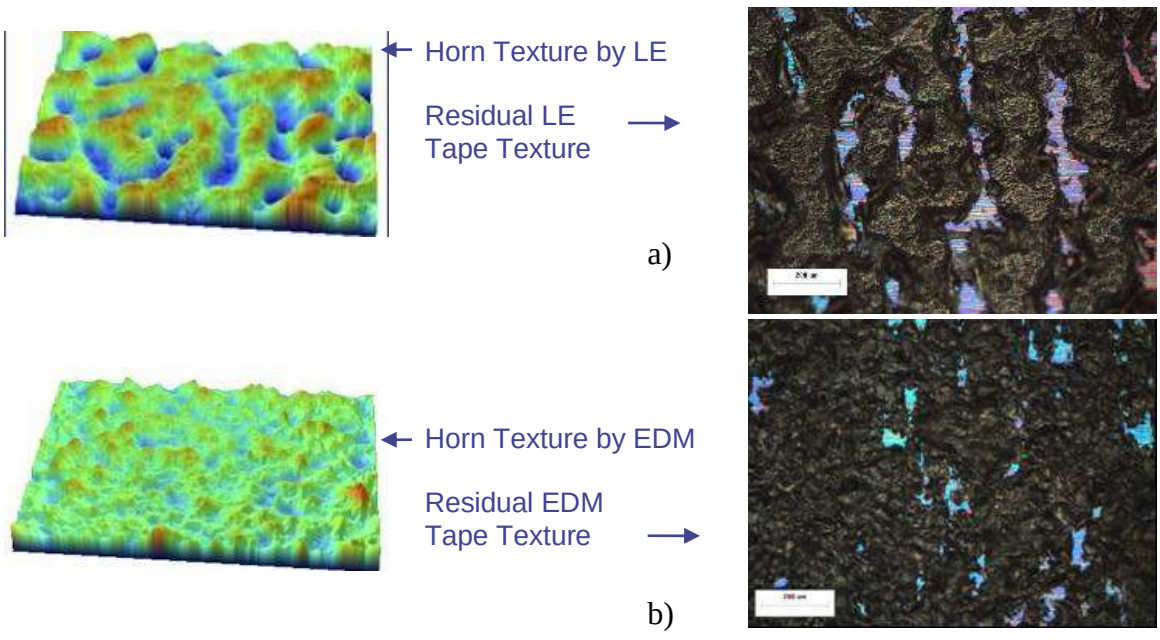

Figure 56 Laser etched (a) and EDM (b) sonotrode textures and the optical micrographs of the residual textures left behind. The blue (or light) areas are in indication of void volume.

Additional sample evaluations were then conducted to gather supporting macroscopic data related to the general influence of the two transferred textures on subsequent build layers. Specifically, an additional foil layer was deposited to each new substrate and then removed. Optical micrographs of the resulting undersides of each foil were then taken and compared with the micrographs of the substrate prior to the foils deposition (ie. with the texture that resulted from the transfer of the sonotrode texture during the previous deposition). Figure 57 shows the effect of the LE produced substrate surface on subsequent foil depositions. Note that the black areas once again show plastically deformed regions where the bottom of the new foil (b) came into contact with the highest asperity surfaces on the substrate (a).

a)

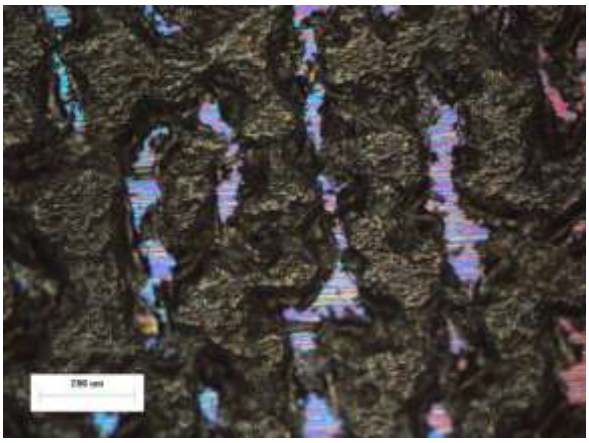

b)

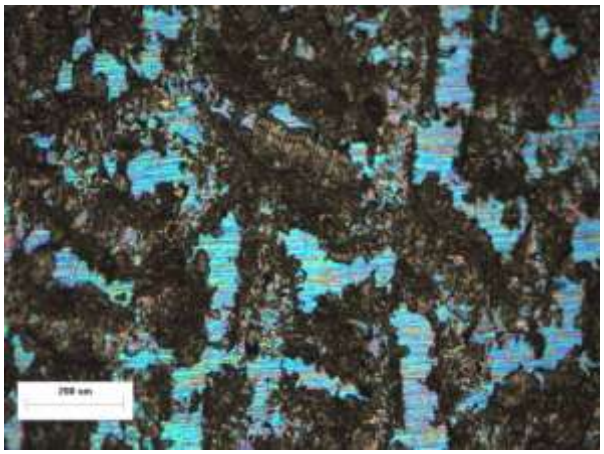

Figure 57 Optical micrographs of a) residual texture on top of tape from LE sonotrode contact; b) residual texture on bottom of tape (after subsequent layer bonding and forced separation).

Figure 58 shows the same results for the case of the EDM textured substrate. In this case the EDM substrate, with its higher consistency and lower Ra values, left a different pattern than that left by the LE surface. In the case of the EDM the black contact regions were smaller, and somewhat more consistent than with the LE sample.

a)

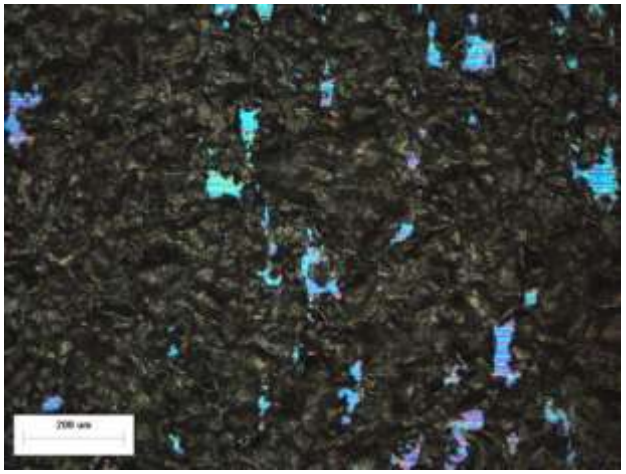

b)

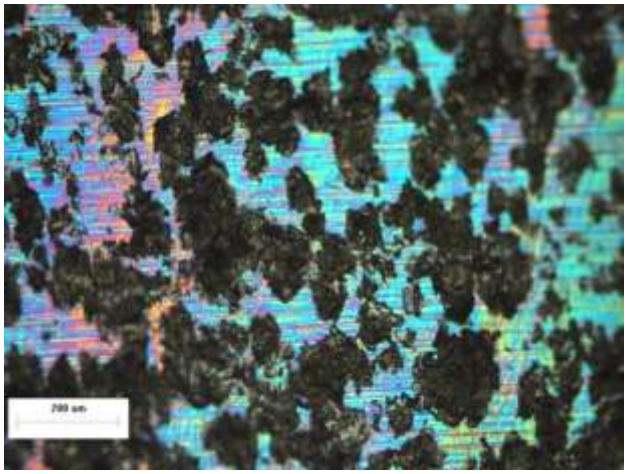

Figure 58 Optical micrographs of a) residual texture on top of tape from EDM sonotrode contact; b) residual texture on bottom of tape (after subsequent layer bonding and forced separation).

7.1.4. SEM Electron Micrographs of Weld Cross Section

Cross section samples were then produced and polished for both the LE textured samples and the EDM textured samples. In general, the SEM electron micrographs of

the cross sections appeared consistent to the earlier results in that the LE surfaces had a topology that was noticeably rougher than the surfaces that remained following the EDM sonotrode contact. Figure 61 shows two such micrographs, note the significant size of the asperities that result form the sonotrode contact that appear to be on the order of 15-25 μm.

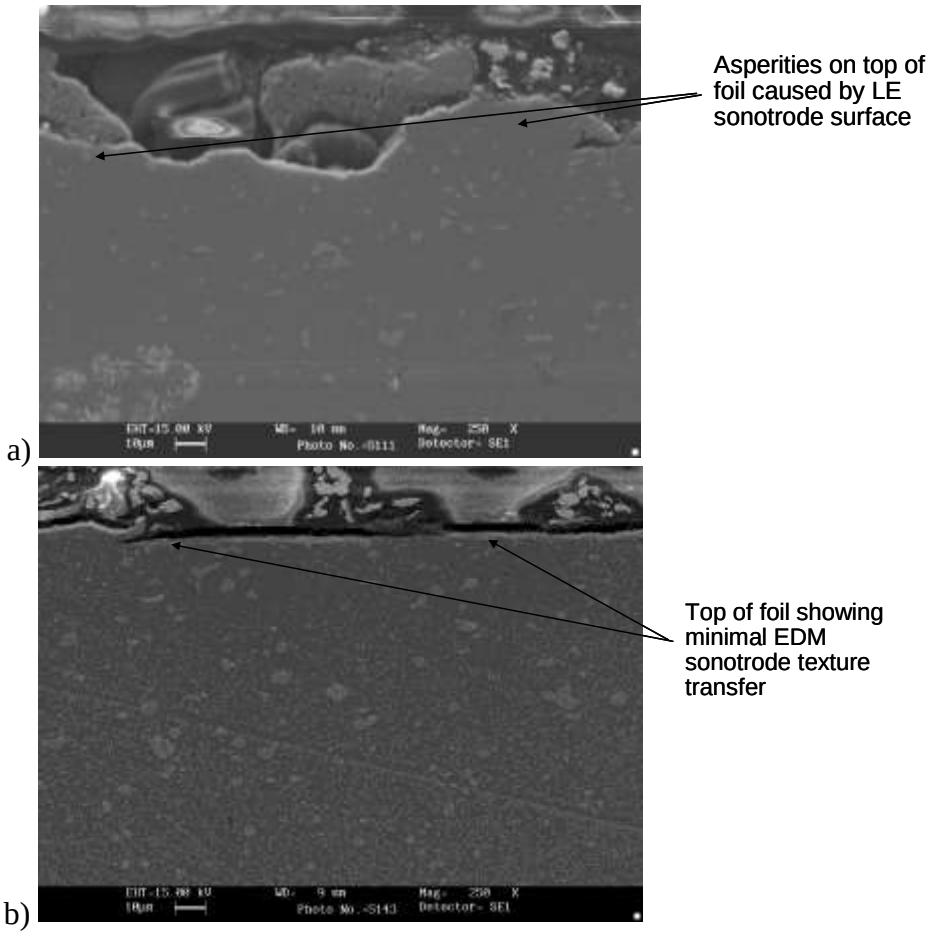

Figure 59 SEM electron micrographs of a) Cross section of top of foil produced from LE textured sonotrode at an amplitude of 20 μm and a sonotrode velocity of 30 mm/s; b) Cross section of top of foil produced from EDM textured sonotrode at an amplitude of 20 μm and a sonotrode velocity of 30 mm/s.

The influence of the transferred texture was additionally evident when an entire five layer UC processed "stack" was fabricated with each sonotrode. Figure 60 shows two separate five layer stacks produced by UC, one fabricated with the generally rough LE sonotrode and the other fabricated with the less rough EDM

sonotrode. These specimens indicate an increase in voids resulting from the LE sonotrode over the EDM sonotrode. A rudimentary count of the void regions within the two samples provides a quantitative value to this result. In the EDM sample there are approximately 8 void rich areas whereas in the LE sample there are 18.

a)

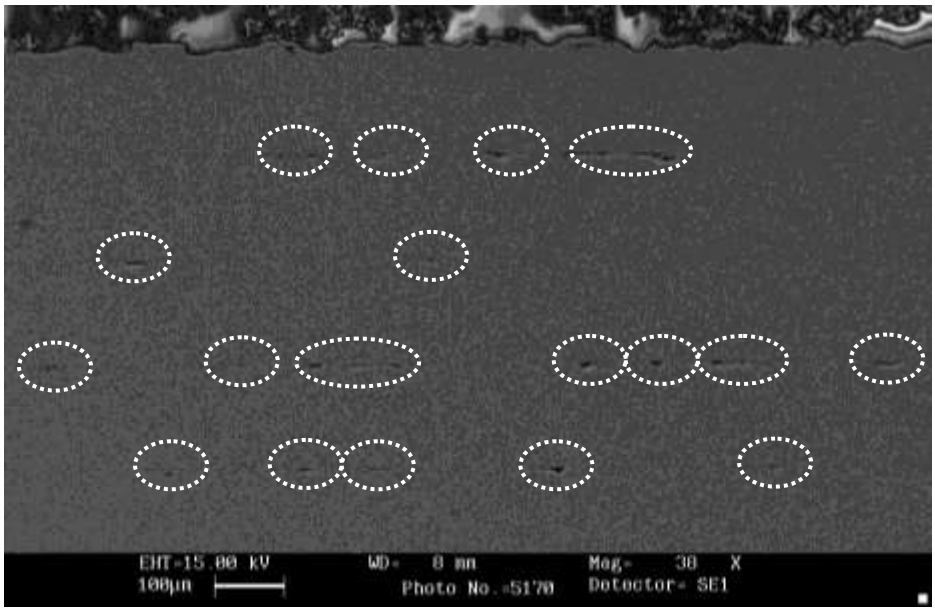

b)

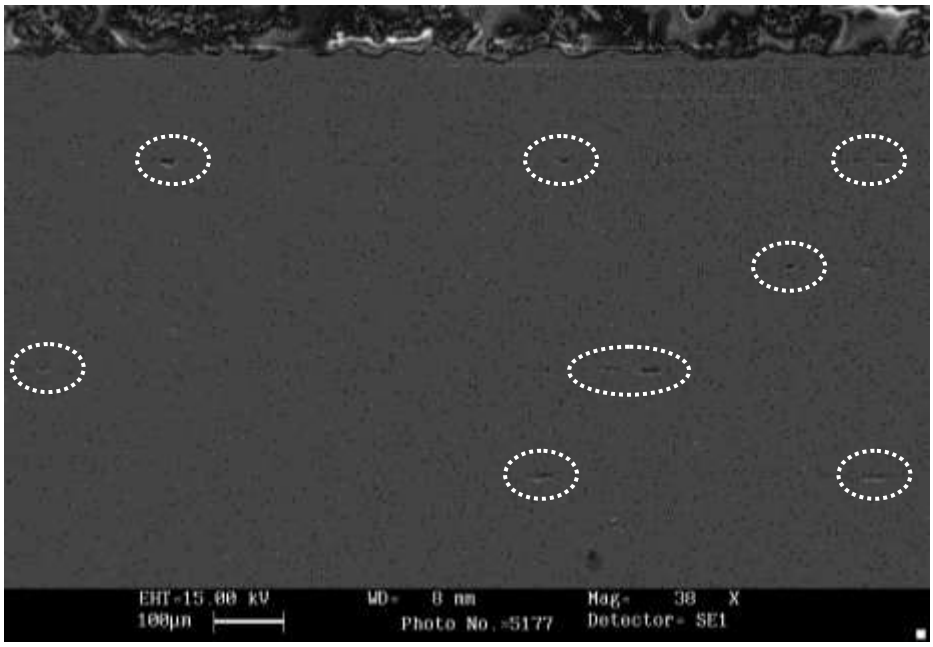

Figure 60 SEM electron micrographs of a) Cross section of top of a five layer stack of foil produced from LE textured sonotrode at an amplitude of 20 µm and a sonotrode velocity of 30 mm/s; b) Cross section of a five layer stack produced from EDM textured sonotrode at an amplitude of 20 µm and a sonotrode velocity of 30 mm/s.

7.2. DBFIB-etch Results for Primary Sample

Figure 61 shows an SEM electron micrograph of the aluminium 3003 T0 sample following the completion of the ion beam induced secondary electron micrograph gathering process. Each of the dark squares represents one micrograph from a region approximately 16 μm x 16 μm in size. Note that each micrograph overlapped several microns with the previous micrograph which allowed for post "stitching together" of the entire region to provide useful continuity imagery. A sample area for the DBFIB-etching was selected following a visual analysis of the entire laminate sample. Care was taken to select an area that appeared to be "typical" of the three layer UC sample stack (ie. no abnormally large voids or areas of obvious poor weld quality).

Consistent with other regions throughout the sample the selected area appeared to possess both "good" and "poor" bonding (typical of many UC articles). "Good" bonding would be classified as areas where there was no observable gap as seen through an SEM at the interface. "Poor" bonding would be classified as areas where either a void, or a small gap could be seen with the aid of the SEM. It is important to note that the pronounced presence of the actual interlaminar region following the etching process (seen as the white regions, or "winding lines" within the ion beam induced secondary electron micrograph regions), were only visible following the DBFIB etch process as prior to this the regions were largely grey, as is typical of SEM electron micrographs of aluminium.

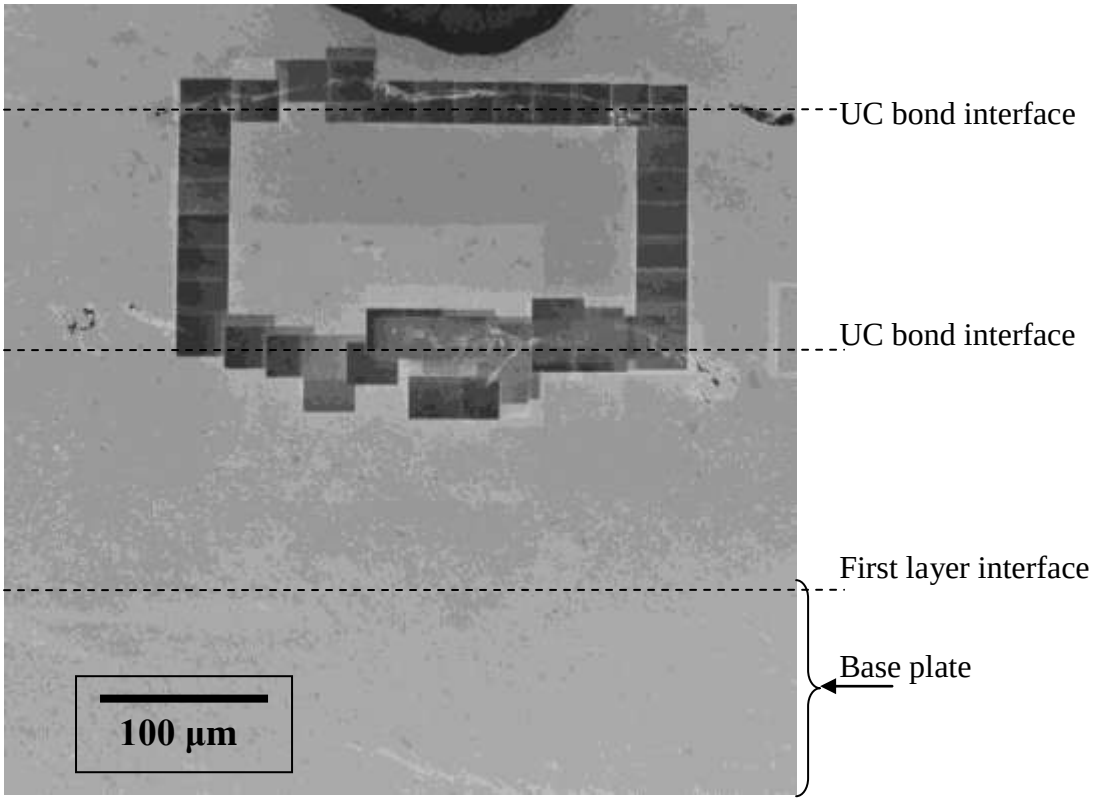

Figure 61 SEM electron micrograph of aluminium 3003 T0 sample following DBFIB-etch and ion beam induced secondary electron micrograph capture process.

7.2.1. Ion Beam Induced Secondary Electron Micrograph Sample Region Identification

Figure 62 provides the assigned micrograph identification number (corresponding to the general ion beam induced secondary electron micrograph gathering sequence) for each of the micrographs that were analysed. The numerical gap between each of the micrograph numbers in the sample region was due to the fact that the DBFIB-etch method is an iterative etching process whereby each area is "etch-scanned" multiple times until a suitable micrograph quality is achieved for a given area. A suitable micrograph quality is achieved by adjusting the ion beam power levels and focus until an acceptable balance has been reached for a given material. The ideal settings to achieve the appropriate operating parameters are calibrated in a separate region close to the primary sample region.

Once the correct settings were achieved, the ion beam was shifted to the region of interest and the etch micrographs were gathered one at a time (often requiring 2-4 “scans” or ion beam material removal raster’s per micrograph area). The typical settings that were found to work best for this research were an ion beam power level of 50 pA and a raster time of 90 seconds per micrograph. Following the first etched micrograph acquisition, the scan area was then moved to the next adjacent location where the iterative process began once again. Note also that due to the non-linearity of the interface, the micrograph regions frequently had to be moved up or down to ensure that the interface region was generally maintained within the micrograph image area.

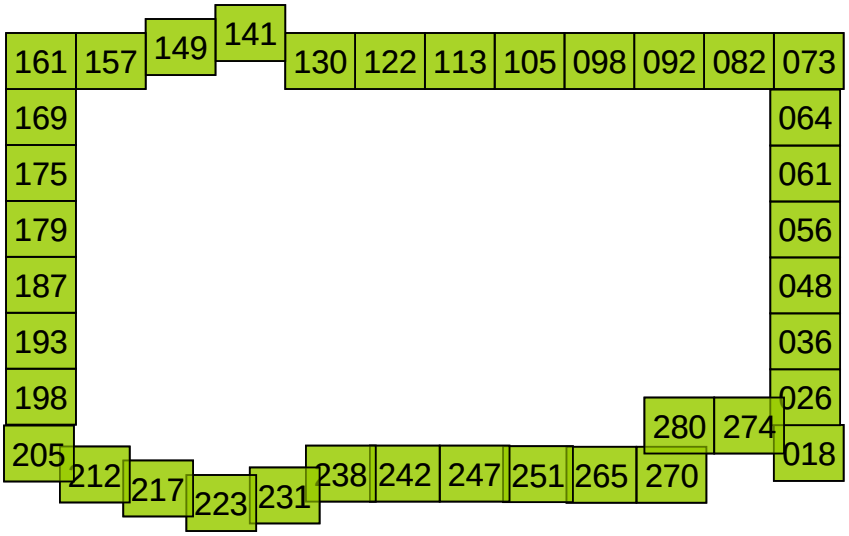

Figure 62 Numbers for the respective micrographs that were gathered using the DBFIB-etch method.

7.2.2. Ion Beam Induced Secondary Electron Micrograph Examples

Samplings of the micrographs taken are shown in Figure 64 through Figure 67. These micrographs prominently show a change (or reduction) in sub-grain size and plastic-flow induced sub-grain morphology when compared to an optical micrograph of aluminium 3003 T0 foil that has not undergone the UC process (see Figure 63).

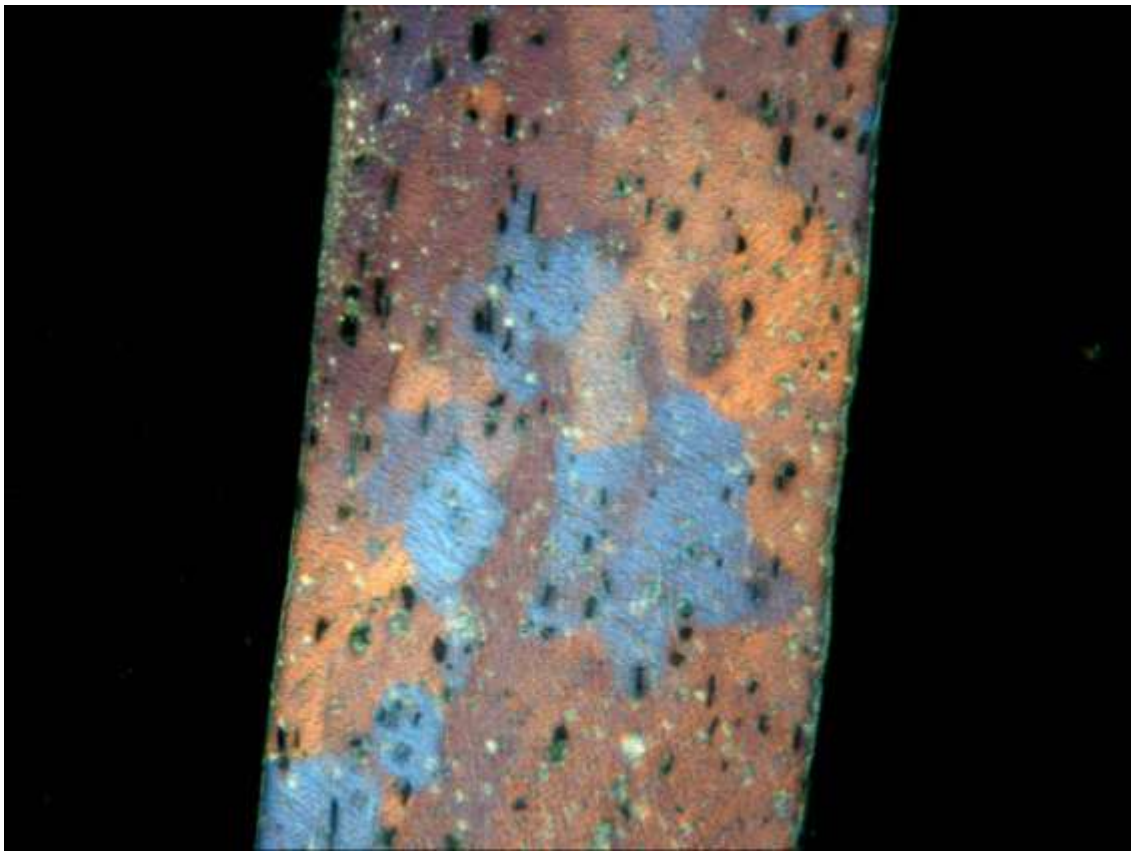

Figure 63 SEM electron micrograph of grain structure in an as-rolled foil of aluminium 3003 T0 that has not undergone the UC process.

This change is generally identifiable in each micrograph by simply observing the non-equiaxed nature of the sub-grain morphology (ie. the sub-grains are clearly not all the same size within the micrographs). Some key observations of the following micrographs are as follows:

- The white regions in Figure 64, or "winding white lines", are possibly the oxide region of the original interface and would indicate a lack of disruption of the pre-weld Al_2O_3 layer.
- There is an increased amount of cold work (as evidenced by the difference in sub-grain size above and below the interface) that has occurred to a gradient extent below the interface as compared to that occurring above the interface, as is most clearly shown in Figure 65.

- Sub-grain morphology “flow” seems to have been influenced by potential collapsed asperities and/or other foil surface flaws as shown in Figure 66.
- Nano-grain colonies were found in a variety of locations in and around the interface, occurring more frequently below the interface and near non-planar interface regions such as in Figure 67.

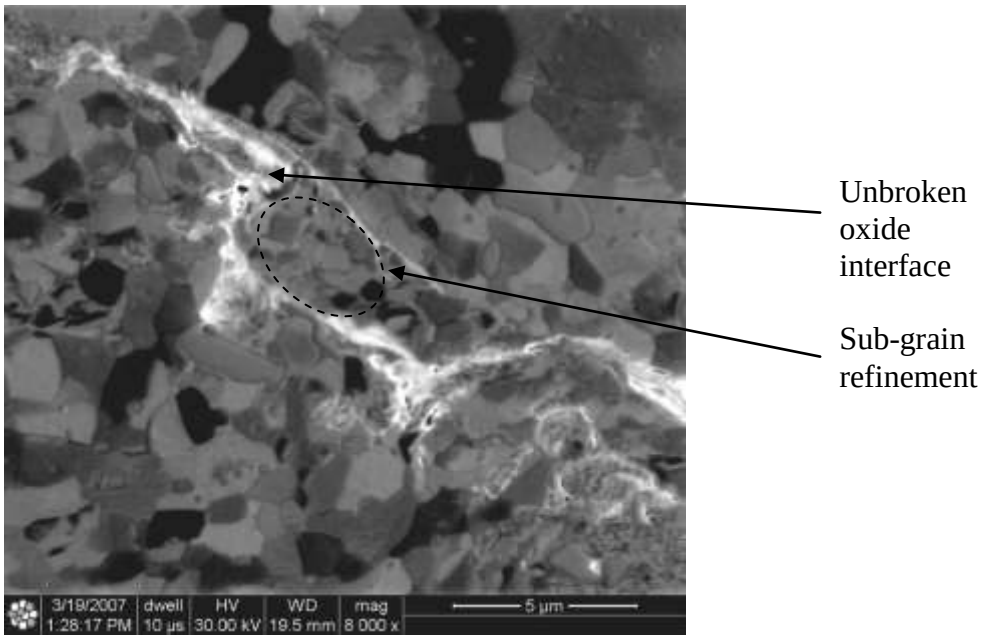

Figure 64 Ion beam induced secondary electron micrograph of DBFIB-etch result for UC interface region, note unbroken oxide layer (in white).

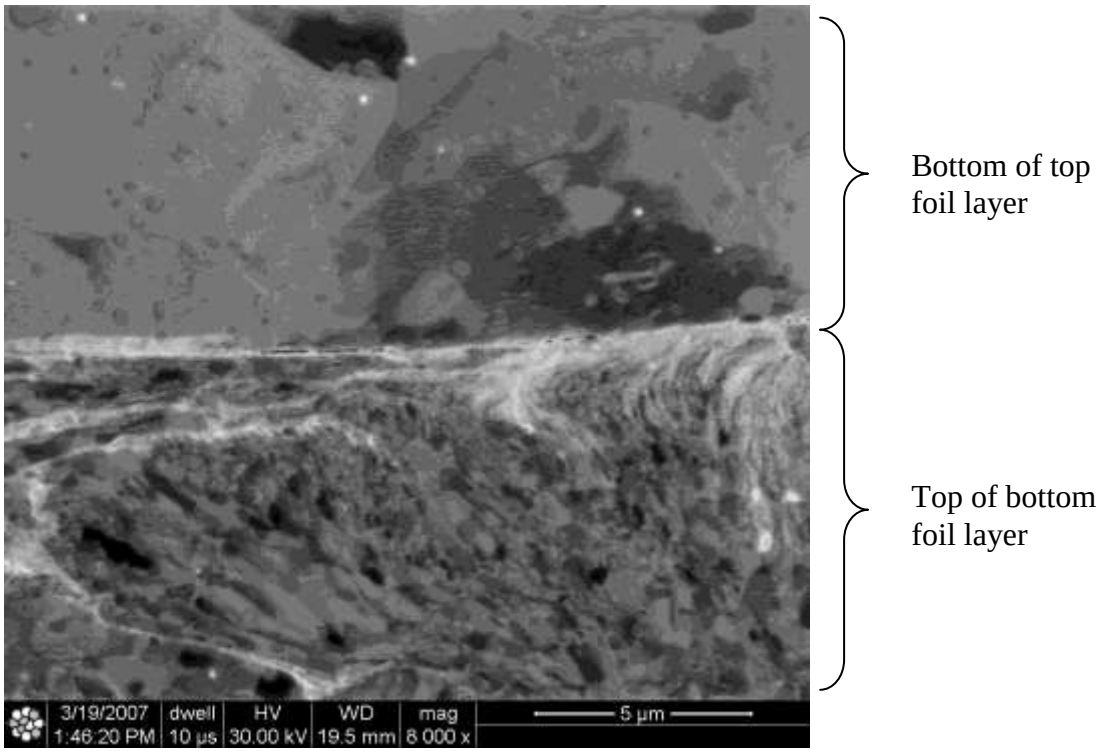

Figure 65 Ion beam induced secondary electron micrograph of DBFIB-etch result for UC interface region showing dominance of plastic work occurring on the top of a foil as opposed to the relatively flat bottom foil surface.

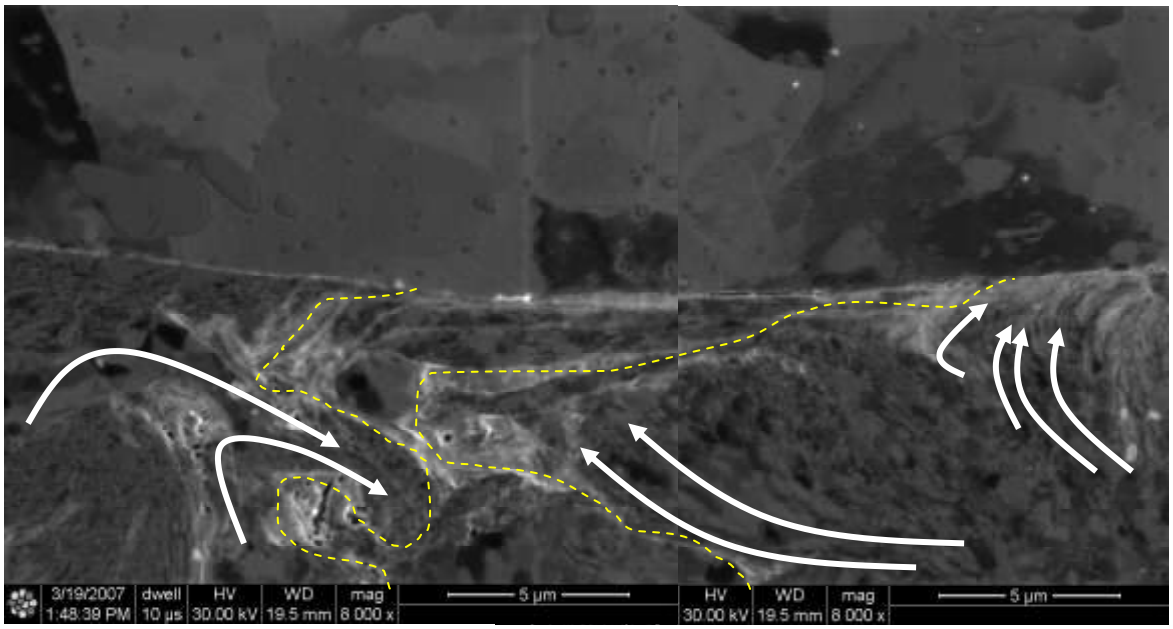

Figure 66 Ion beam induced secondary electron micrograph of DBFIB-etch sample for UC interface region showing complex displacement and re-orientation of substrate asperity voids. The dashed lines within the micrograph represent possible interfaces of a pre-process asperity that has subsequently been plastically deformed and flattened during the UC process. The white "flow" lines highlight the directionality of the plastic deformation.

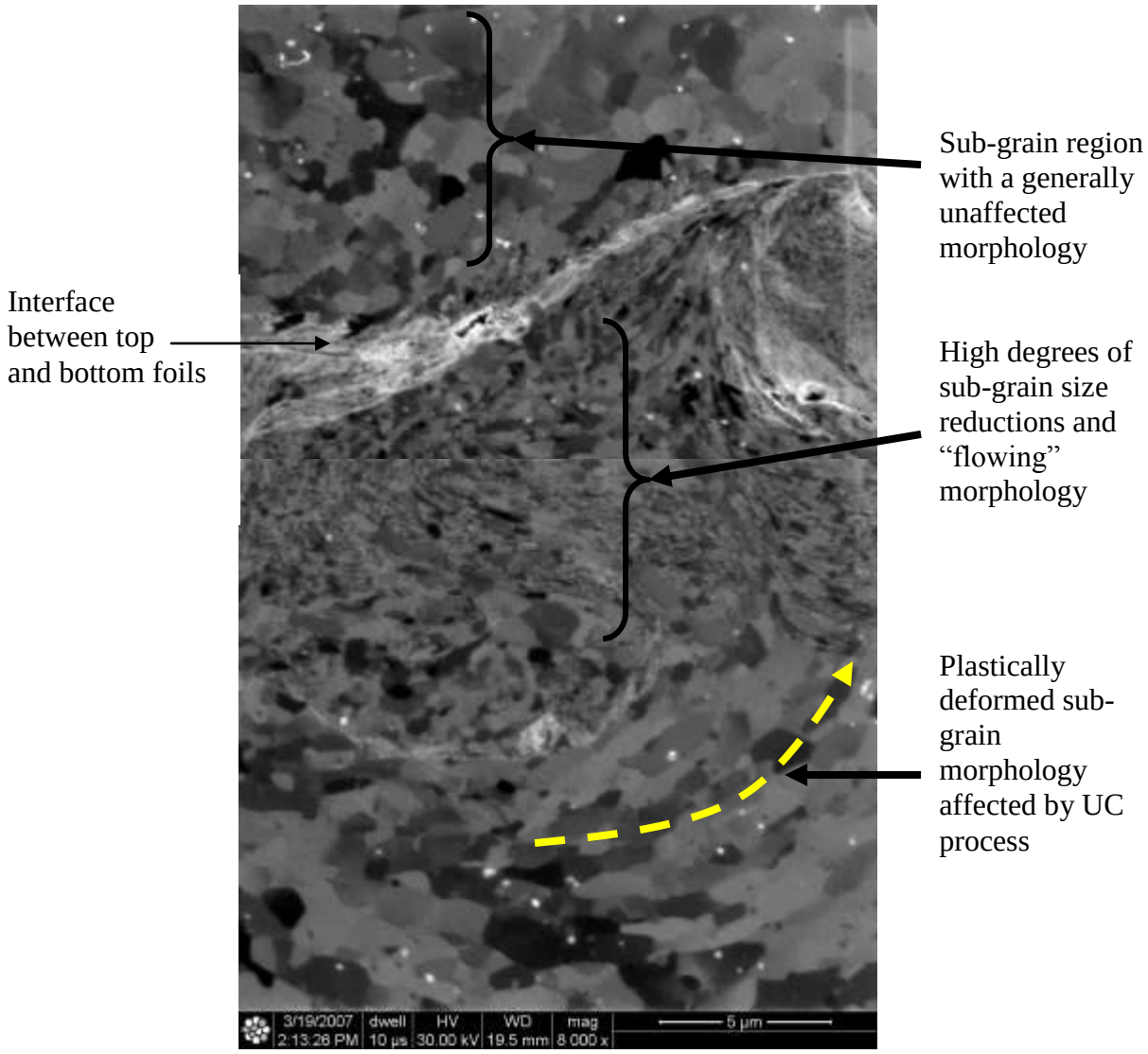

Figure 67 Ion beam induced secondary electron micrograph of DBFIB-etch result for UC interface region showing extent and depth of sub-grain morphology change as a result of the plastic deformation.

7.2.3. Summary Results of Average Sub-grain Size

A total of 315 unique sub-grain regions as shown in Figure 40 were analyzed using the linear intercept method. The graph in Figure 68 provides a high level visual summary of the results of the average sub-grain size in the sample.

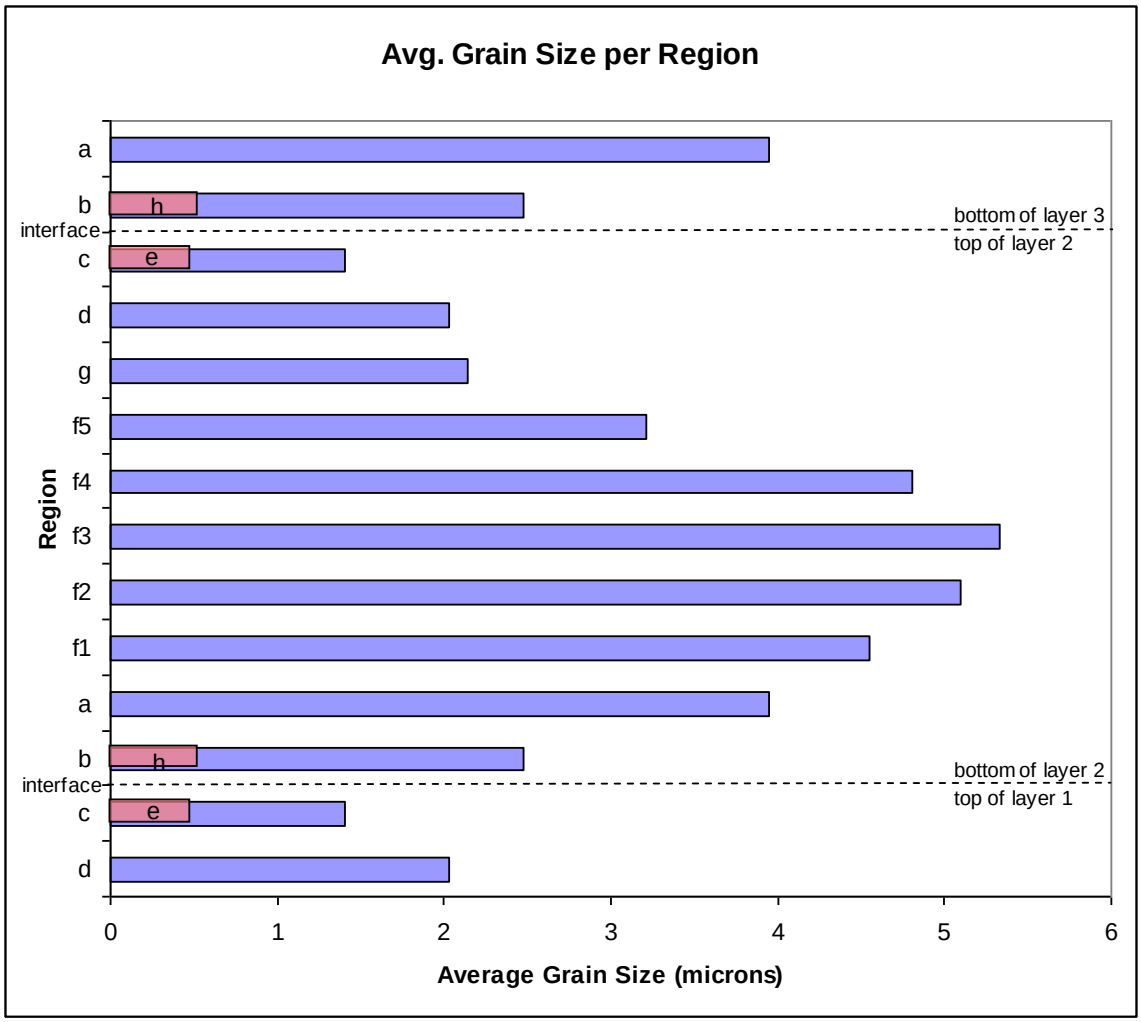

Figure 68 Summary of results of sub-grain calculation following UC processing for each of the 12 sample regions.

The exact values of the mean, standard deviation, and sample size are provided in Table 8. Note that the smallest and largest sub-grain size value is also presented in this table the help illustrate the general variability of the morphology. X represents the average sub-grain size for a given region, n represents the total number of sample areas within a region that were analyzed using the mean linear intercept method, s is the standard deviation for the given set of samples within a region. These data will be discussed further in the following chapter.

Table 8 Summary of sub-grain size results by region.

Region	χ (μm) Mean	n Sample size	s Std Dev	Smallest	Largest
e	0.487	19	0.090	0.35	0.677
c	1.402	61	0.729	0.595	3.925
d	2.024	47	0.789	0.981	3.925
g	2.144	10	0.857	0.654	2.804
f5	3.206	12	2.143	1.51	9.813
f4	4.805	17	1.901	2.804	9.813
f3	5.328	23	2.456	2.453	9.813
f2	5.102	16	1.767	2.804	9.813
f1	4.545	18	1.629	2.804	9.813
a	3.944	31	2.405	1.09	9.813
b	2.480	58	2.075	0.654	9.813
h	0.565	3	0.118	0.491	0.701

7.2.4. 95% Confidence Limit Calculation

Additionally, the 95% confidence limit was calculated for the sample group of each region to assess the variability of the sample mean. Equation [6.2] was used to determine the confidence values utilizing the following t values.

Table 9 The 95% confidence values for sample regions

Region	t	95% error S
e	2.101	0.043
c	2.000	0.187
d	2.010	0.231
g	2.262	0.613
f5	2.201	1.361
f4	2.120	0.977
f3	2.080	1.065
f2	2.131	0.941
f1	2.110	0.810
a	2.042	0.882
b	2.000	0.545
h	4.303	0.293

The t values for 95% confidence limits are a function of the number of degrees of freedom for each sample region (v = n -1). The t values were taken from existing reference tables[78]. The resulting 95% confidence interval can then be applied to a single mean value that is calculated to define a range within which there is a 95% probability that the actual mean exists. These results were next plotted in conjunction with the average grain boundary separation data as shown in Figure 69.

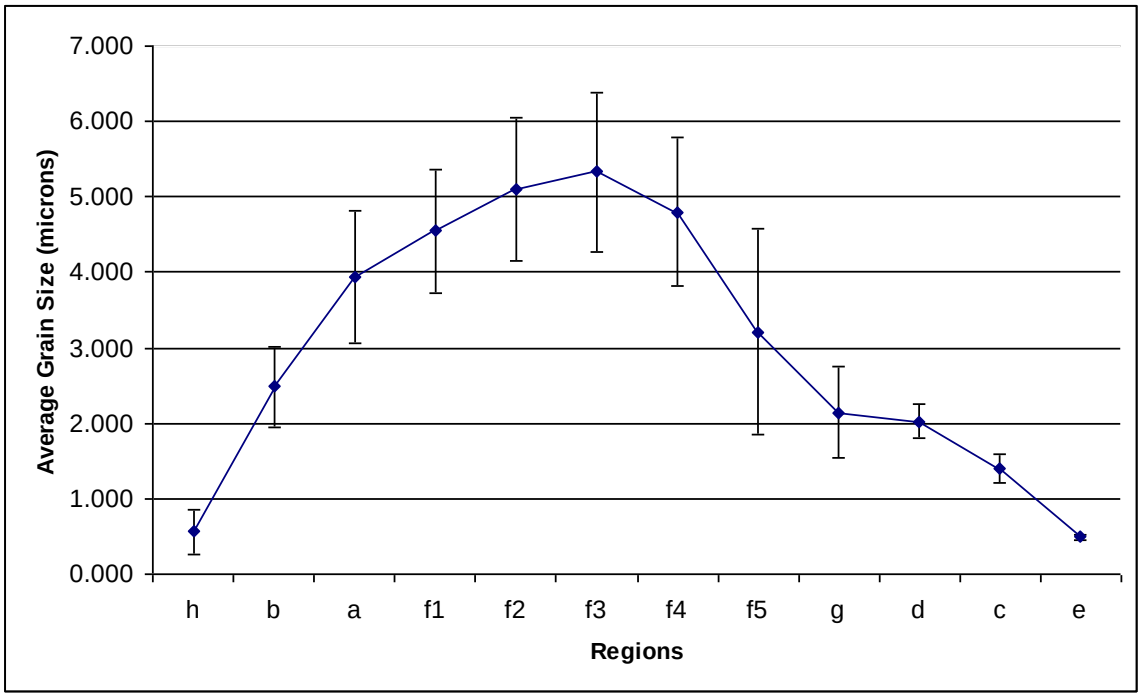

Figure 69 Average grain boundary separation data by region with corresponding 95% confidence intervals.

7.2.5. DBFIB-etch Combined with High Magnification SEM

Additional high magnification SEM electron micrographs were successfully gathered from the primary sample using a combination of DBFIB-etching and standard SEM microscopy. These micrographs were taken on an excavated plane that was perpendicular to the orientation of all of the previous ion beam induced secondary electron micrographs as shown in Figure 42.

Following etching, several high magnification SEM electron micrograph were taken of the area which provided an excellent detailed view of the various UC regions that have been previously described (Figure 70). This micrograph further provided compelling confirmation as to the existence of a stepped transition region between the nano-grain region and the plastically deformed sub-grain regions.

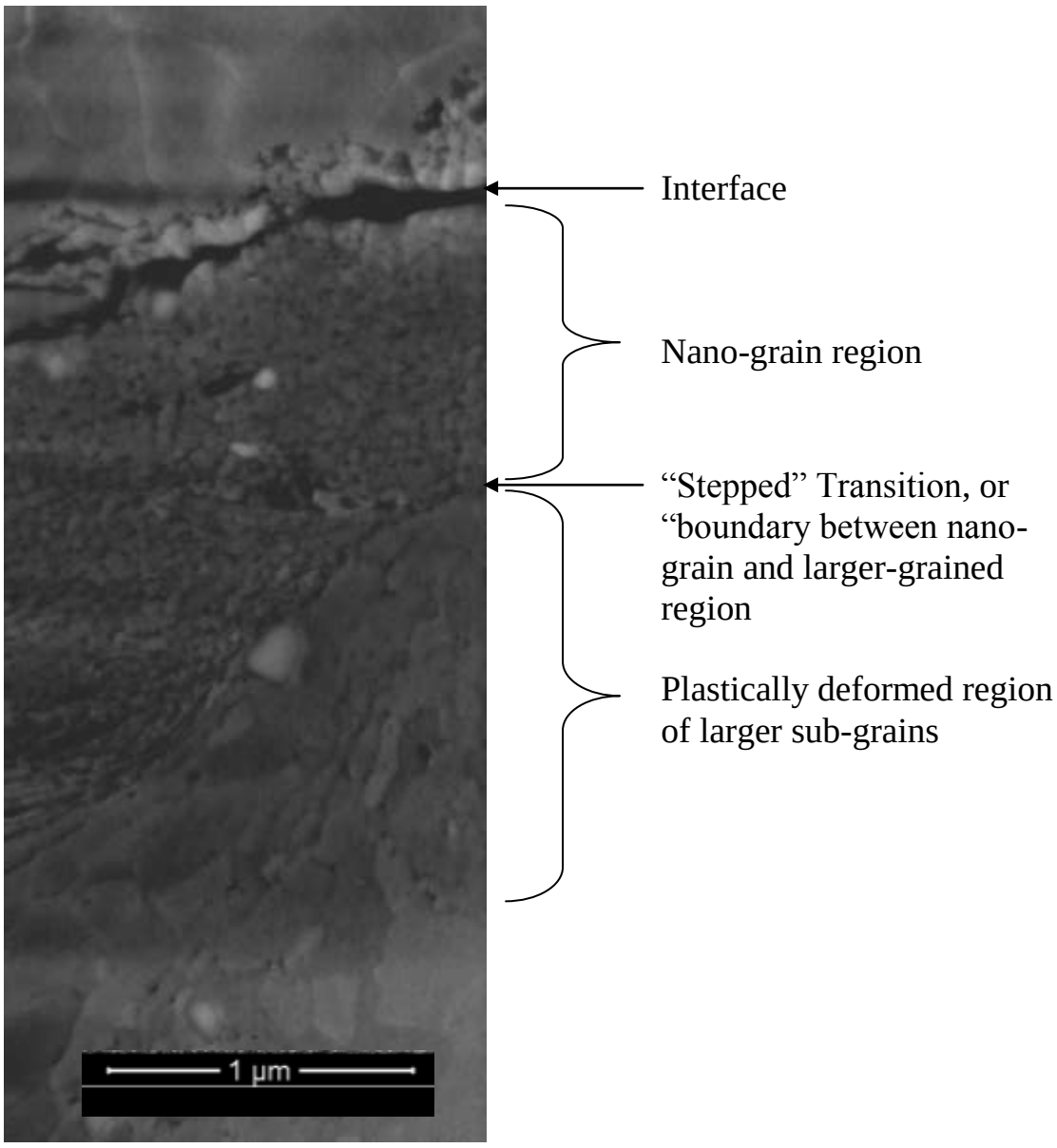

Figure 70 SEM electron micrograph showing aluminium 3003 T0 sample interface region illustrating post UC nano-grain regions.

7.2.6. Identification of Direct Sonotrode Contact Effects

As noted previously, it became clear that it was also important to evaluate the sub-grain refinements caused directly between the sonotrode and the top of the foil layer to determine the extent of sub-grain refinement being caused by the direct contact and cyclic work of the sonotrode, prior to any further UC layer deposition. The primary method to assess this was by analyzing the very top of the three layer stack using the DBFIB-etching process to gather several ion beam induced secondary electron micrographs. The following series of micrographs show these results and indicate that there was indeed a significant amount of sub-grain refinement occurring between the sonotrode and the top of the foil prior to subsequent foil deposition (see Figure 71). Naturally these effects would remain intact prior to the following foil deposition and would have the potential to influence subsequent layer bond quality. These significant considerations will be discussed further in chapter 8.

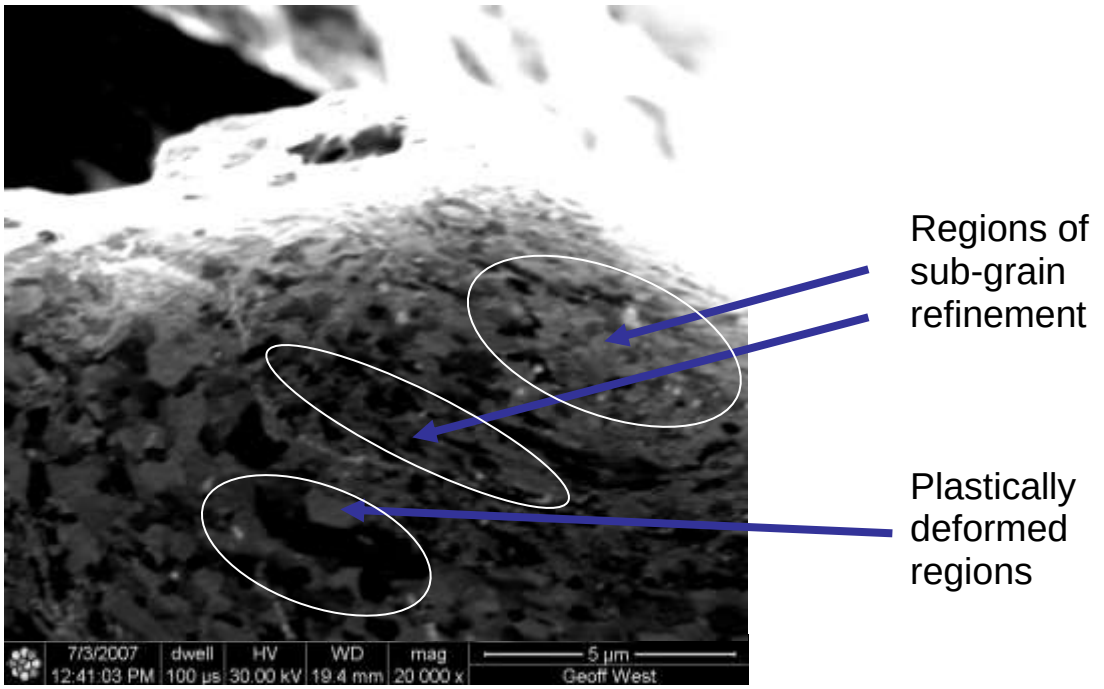

Figure 71 Ion beam induced secondary electron micrograph of top of welded foil layer that experienced direct sonotrode contact (with full ultrasonic's engaged).

Interestingly, the extent of the sub-grain refinement at the top of the three layer stack seemed to be impacted by the topology of the sonotrode and the relation of the normal force to the top of the foil. In cases where there was a "valley" on the top surface of the post weld layer, there was typically less sub-grain refinement identified as shown in Figure 72.

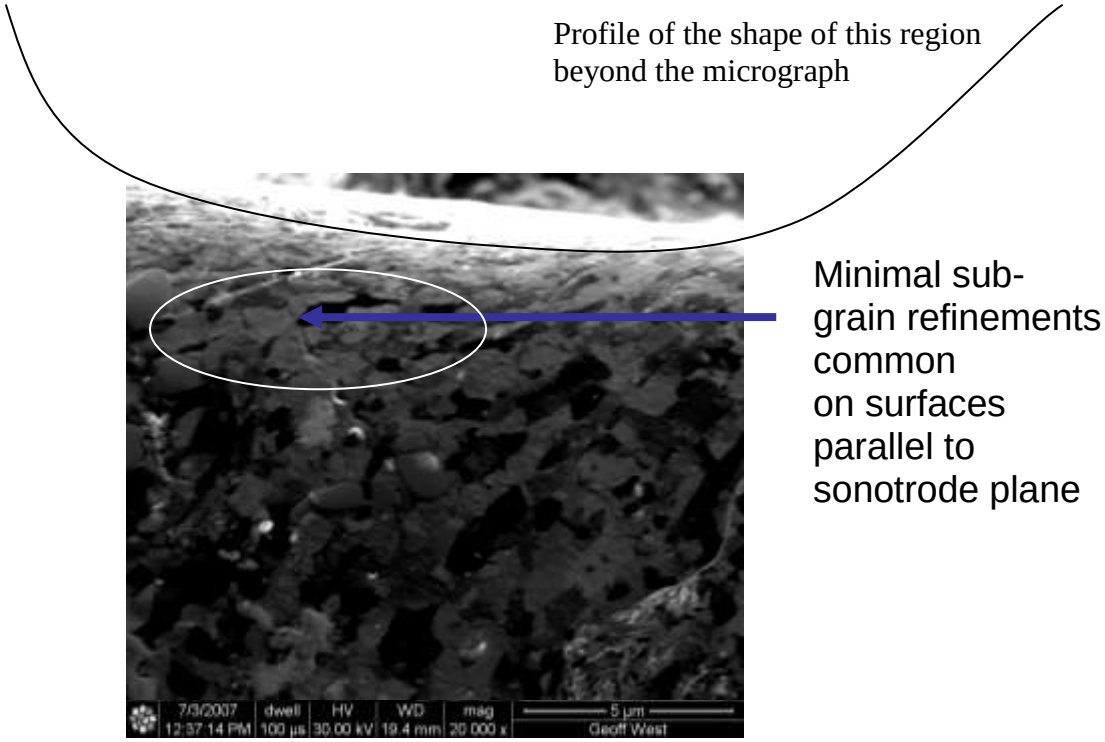

Figure 72 Ion beam induced secondary electron micrograph showing "valley" on the top of the foil following UC process.

Additionally, nano-grained colonies were noticeably prominent when in direct proximity to apparent flaws beneath the foil surface (Figure 73). This would seem to indicate that relative motion and/or dislocation pileups may have occurred in these areas due to a "fault line" or lack of homogeneity, somewhat like a "high resistance" region attracting energy within the system. These flaws may either be artefacts of the commercial rolling process or may also have been foil surface asperities that

collapsed on themselves upon contact with the rolling sonotrode during the UC process.

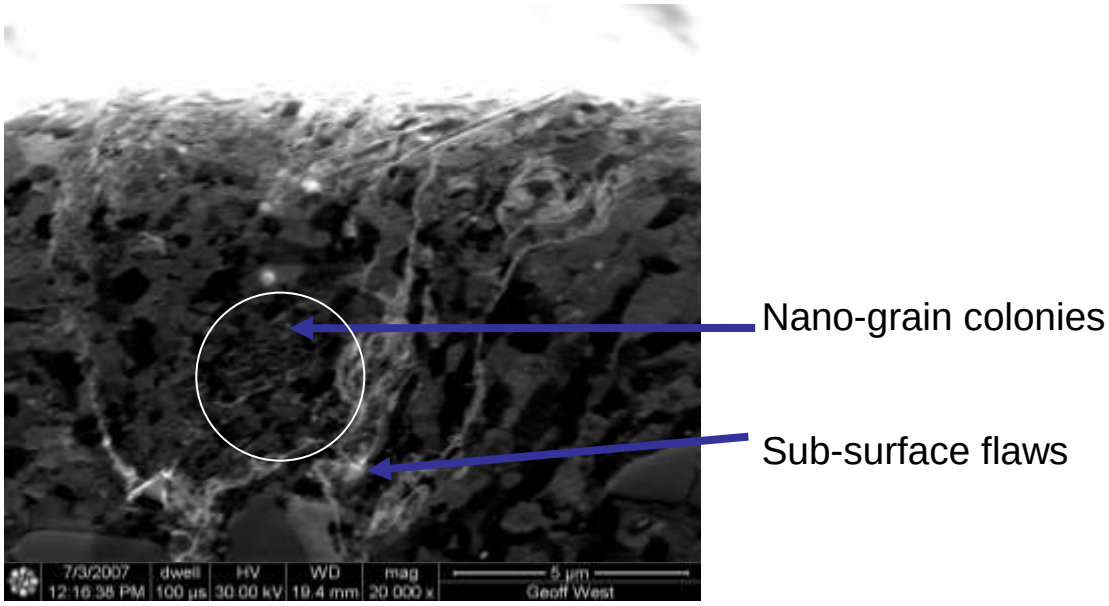

Figure 73 Ion beam induced secondary electron micrograph showing top of foil region illustrating how sub-surface flaws can serve as possible catalysts for sub-grain refinement.

Extensive sub-grain refinements were also frequently observed on diagonal surfaces of the top of the foil following welding as shown in Figure 74. A diagonal surface in this case is defined as an asperity "slope" that was approximately at a 45 degree angle to the substrate plane. As opposed to regions where the sonotrode was not in contact with the foil (and thus there was minimal cyclic motion between the sonotrode and the substrate), diagonal slopes are regions where there appeared to be a high degree of contact.

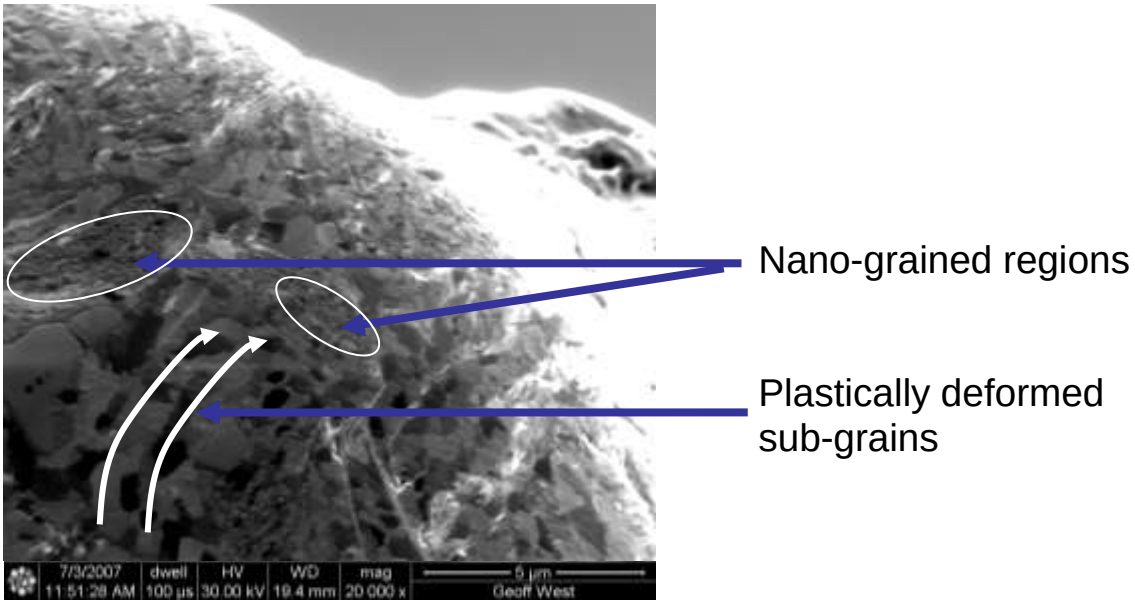

Figure 74 Ion beam induced secondary electron micrograph showing intermittent evidence of nano-grain formations on diagonal surfaces. The white arrows illustrate general directionality and orientation of the sub-grain plastic deformation.

Figure 75 shows the interface following the deposition of a new foil layer, highlighting the similarity of the sub-grain morphology to that of the previous figures, strongly suggesting the potential retention of the sonotrode contact effects following subsequent depositions.

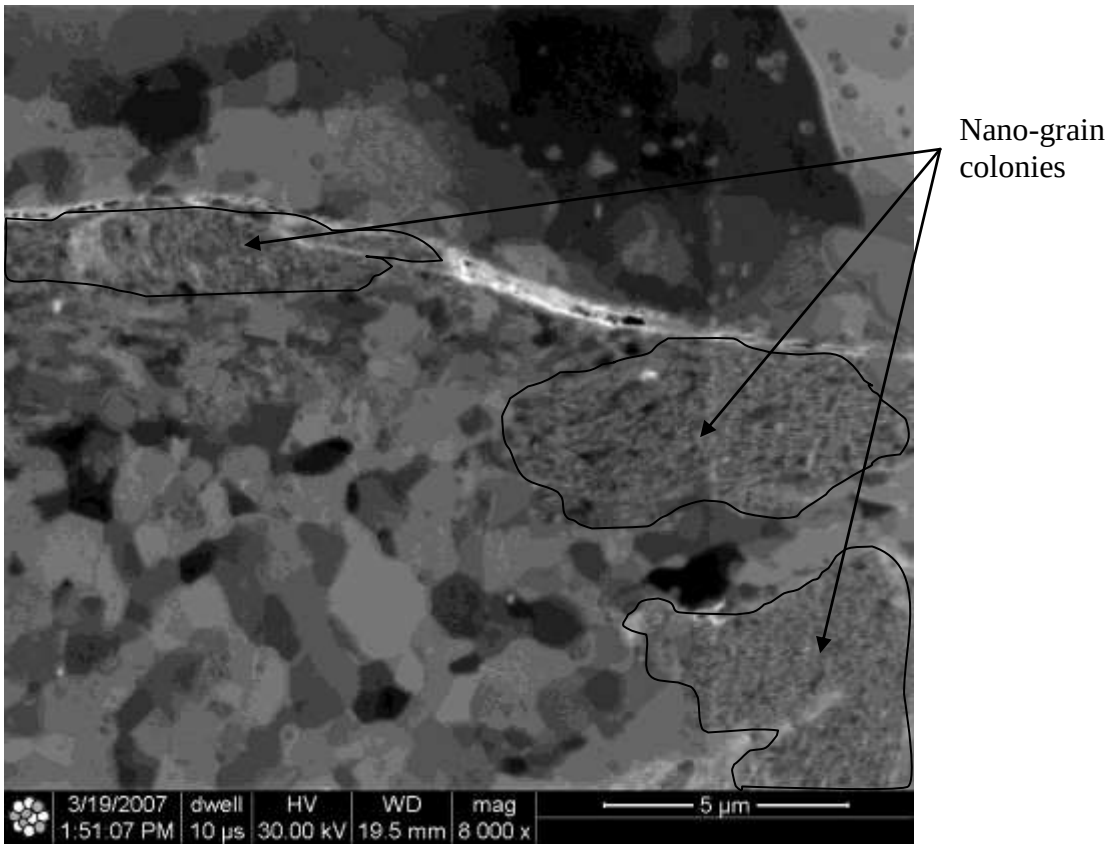

Figure 75 Ion beam induced secondary electron micrograph of DBFIB-etch result for UC interface region showing nano-grain colonies (ie. regions of dense nano-grain sized sub-grains) outlined.

7.3. DBFIB-etch Results from Engineered Mating-Surface Regions.

Additional engineered texture samples were successfully processed for DBFIB-etch analysis to provide a brief examination of the effect of the initial foil interface mating texture and to isolate the non-sonotrode induced sub-grain refinements in a UC weld interface. It is important to stress that for these samples, the previous effects caused by the direct contact of the sonotrode to the top of the foil (which would then become the substrate, or bottom interface surface), as well as the thick oxide layers embedded during the commercial rolling processes, were removed by conventional machining. Thus, these results effectively isolate the effect of the interfacial ultrasonic bonding only. However, given that the three layer UC stack sample was the primary sample and the as-rolled effects and oxides were left intact (which is precisely how the

commercial UC process works in industry for costs and cycle time reasons), care has to be taken in comparing the results. As noted in the experimental method, there were four surface engineered regions that were evaluated as follows.

7.3.1. Highly Polished Interface – "Smooth to Smooth"

When the mating surfaces to be ultrasonically welded were highly polished prior to welding, there was minimal evidence of sub-grain refinement immediately around the interface (Figure 76-Figure 77). The bond interface, or oxide layer, was however, clearly visible in all of the regions that were etched and the interface bond line was extremely planar, as would be expected.

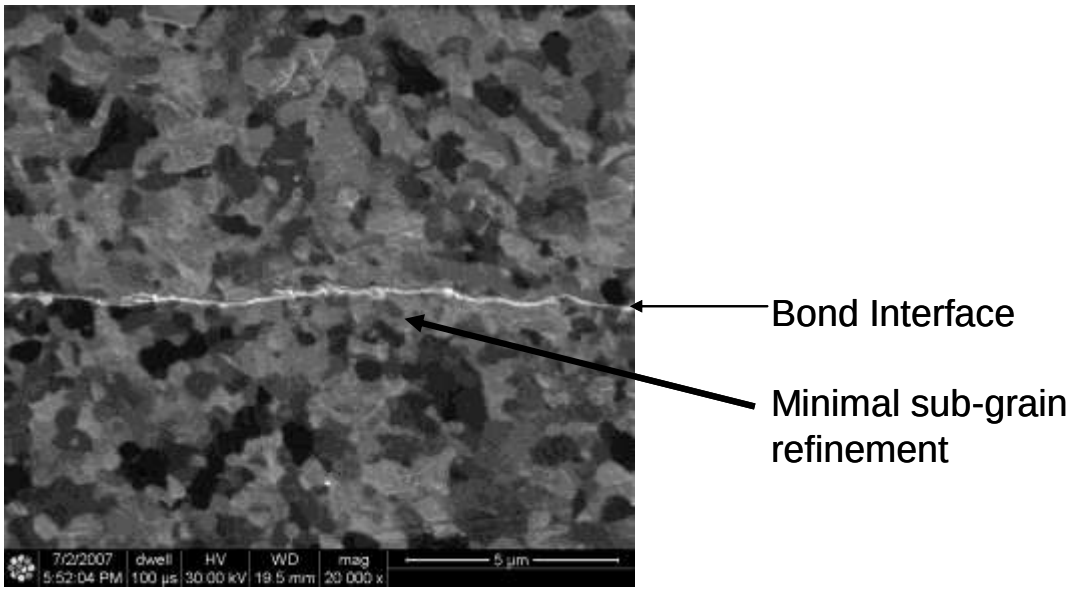

Figure 76 Ion beam induced secondary electron micrograph showing smooth to smooth interface following ultrasonic welding showing minimal sub-grain refinement in and around the interface.

Figure 77 presents another ion beam induced secondary electron micrograph of the smooth to smooth interface taken at a lower magnification to provide a broader view of the interface region. It is apparent that the oxide layer persisted quite readily

in this case and there is also no clear pattern, or gradient, to the sub-grain morphology.

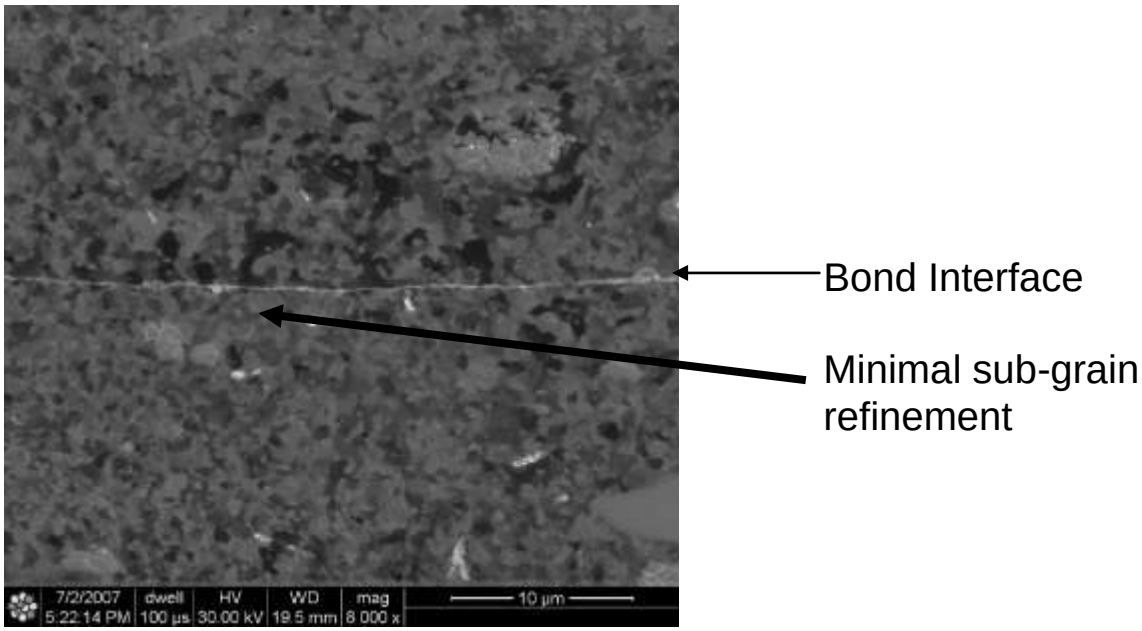

Figure 77 Ion beam induced secondary electron micrograph showing smooth to smooth interface following ultrasonic welding showing minimal sub-grain refinement.

An additional interesting result was observed in the case where a manganese particle had apparently been present at the interface region. It appeared from the micrograph in Figure 78, that the manganese particle was sheared into several smaller pieces by the forces at the interface. This "disturbance" in the system seemed to then facilitate localized sub-grain refinement at and around the interface. This would seem to indicate that there was indeed relative motion at the interface and that like an asperity, the manganese particle had the potential to geometrically disturb the region and initiate sub-grain refinement.

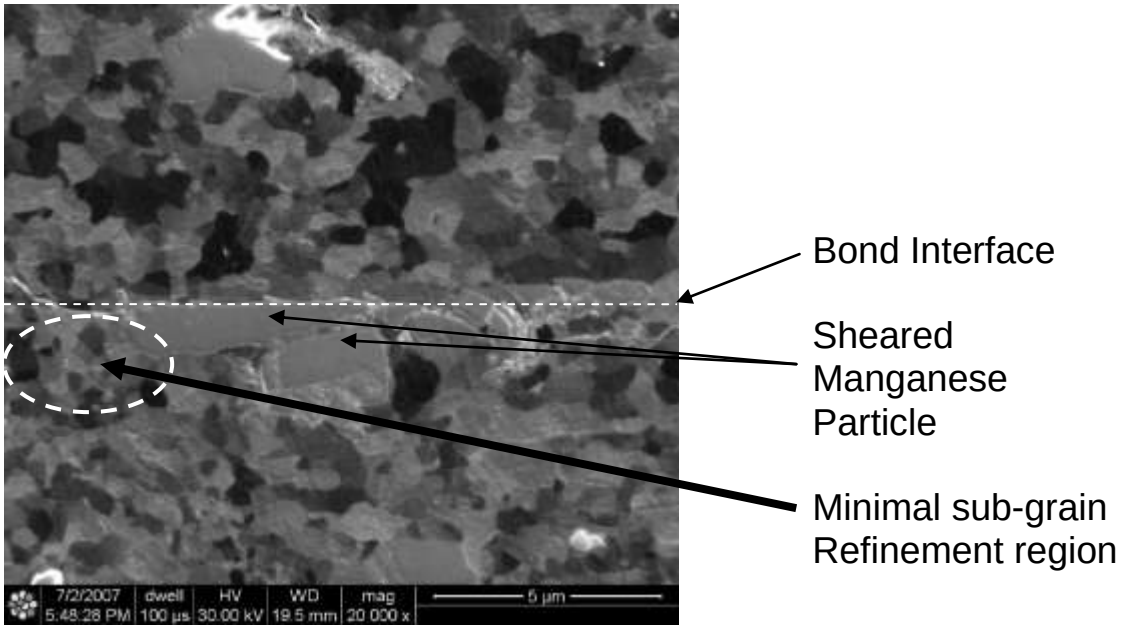

Figure 78 Ion beam induced secondary electron micrograph showing smooth to smooth interface following ultrasonic welding, with manganese particle sheared at interface.

7.3.2. Rolled Surfaces Interface

When the mating surfaces were textured by the rolling sonotrode surface contact alone (with the ultrasonics disengaged), prior to ultrasonically welding the layer, the results were similar to the rough surface results of the primary 3003 T0 samples in Section 7.3.2. Once again, the prior effects of the deposition of the base layer were carefully machined away before the new texture was applied. In this case the rough geometry of the pre-weld asperities seemed to influence the presence and extent of the refined sub-grain region. Figure 79 shows the highly variable interface region seen as a "winding" white line when compared to the results of the previous section. The size of the sub-grain regions were generally similar to that of the primary aluminium 3003 T0 samples where the sonotrode sub-grain refinement was not removed.

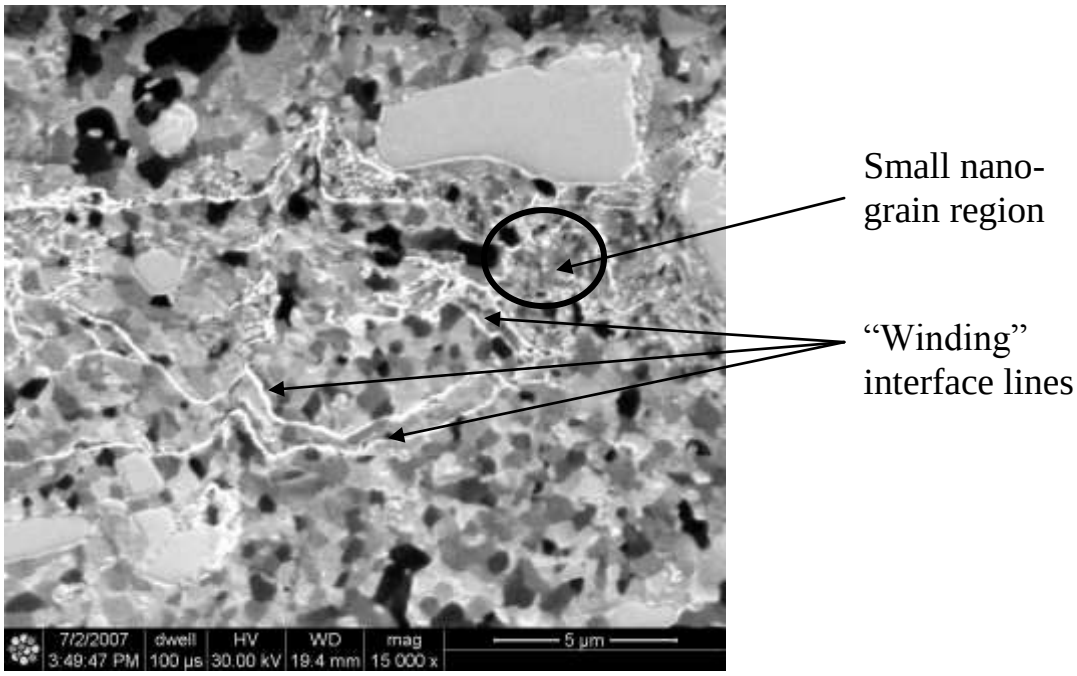

Figure 79 Ion beam induced secondary electron micrograph showing rough to rough interface region, white lines likely represent collapsed asperity boundaries.

Note that in Figure 79 there was a significant network of Al_2O_3 interface boundaries as evidenced by the winding white lines. These were probably boundaries between collapsed asperities and surrounding material as any surface flaws in the rolling process would have generally been removed following the 20.0 µm surface removal.

7.3.3. Interface Texture Perpendicular to Rolling Direction

Similar to the previous sample, when there were grooves perpendicular to the rolling direction, there was evidence of sub-grain refinement near the interface. As would be expected there was also evidence of collapsed asperities resulting in multiple interfacial boundary regions between the two layers. However, there were a few areas (Figure 80) that seemed to have overcome the common oxide interface boundary which resulted in regions where grain growth did indeed seem to have occurred across

the interface. Figure 81 shows several regions of significant sub-grain refinement in and around the interface region.

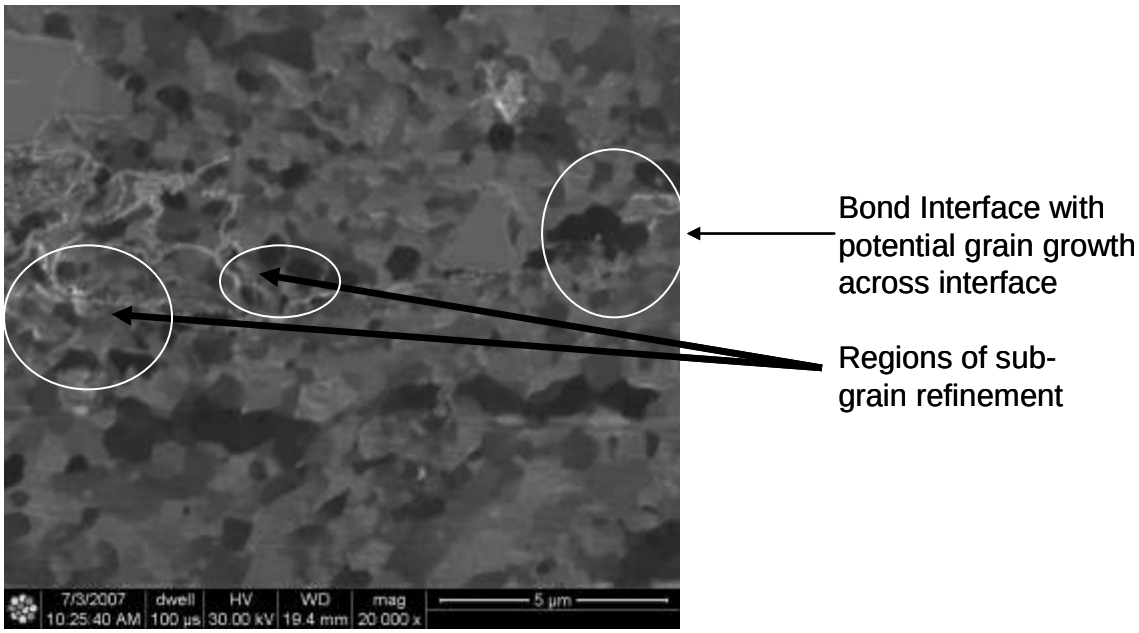

Figure 80 Ion beam induced secondary electron micrograph showing interface of sample with texture perpendicular to rolling direction which shows potential regions of grain growth across interface.

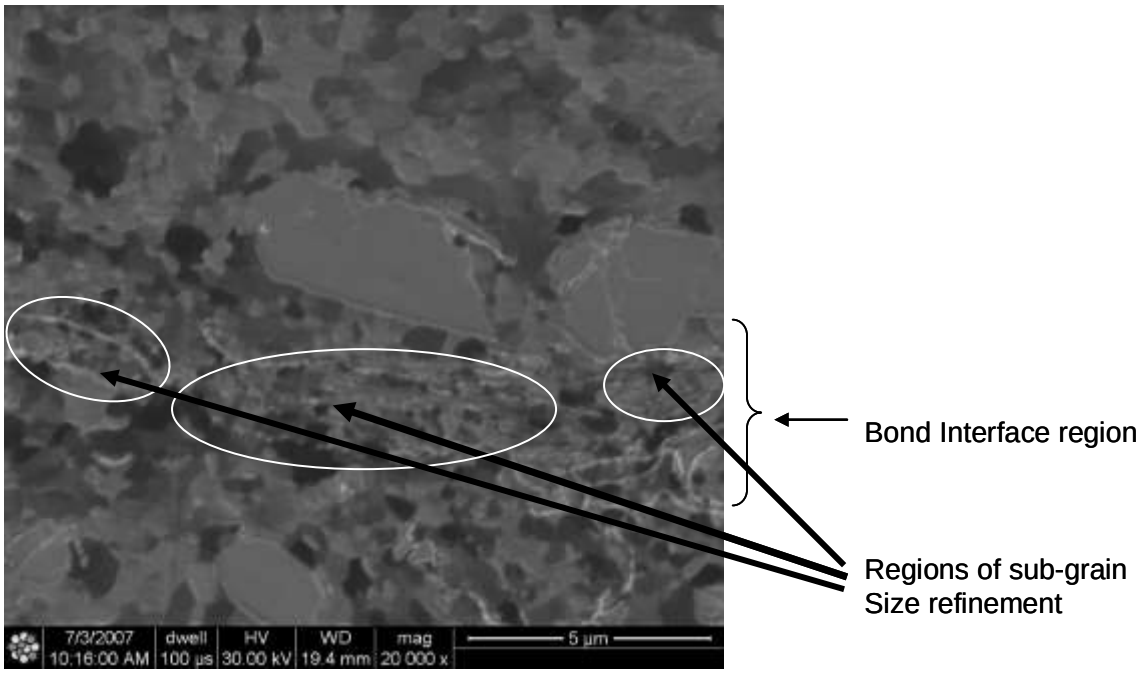

Figure 81 Ion beam induced secondary electron micrograph showing texture perpendicular to rolling direction with signs of sub-grain refinement and plastic flow.

7.3.4. Interface Texture Parallel to Rolling Direction

The results for the samples where the texture was engineered in a direction parallel to the rolling direction proved to be highly intriguing. In nearly all of the micrographs gathered, there was indeed evidence of sub-grain refinement. In addition to this, there were several interface regions were grain growth may have occurred across the interface as suggested by an apparent disappearance of the white interface boundary. Figure 82 through Figure 85 highlight several examples of this.

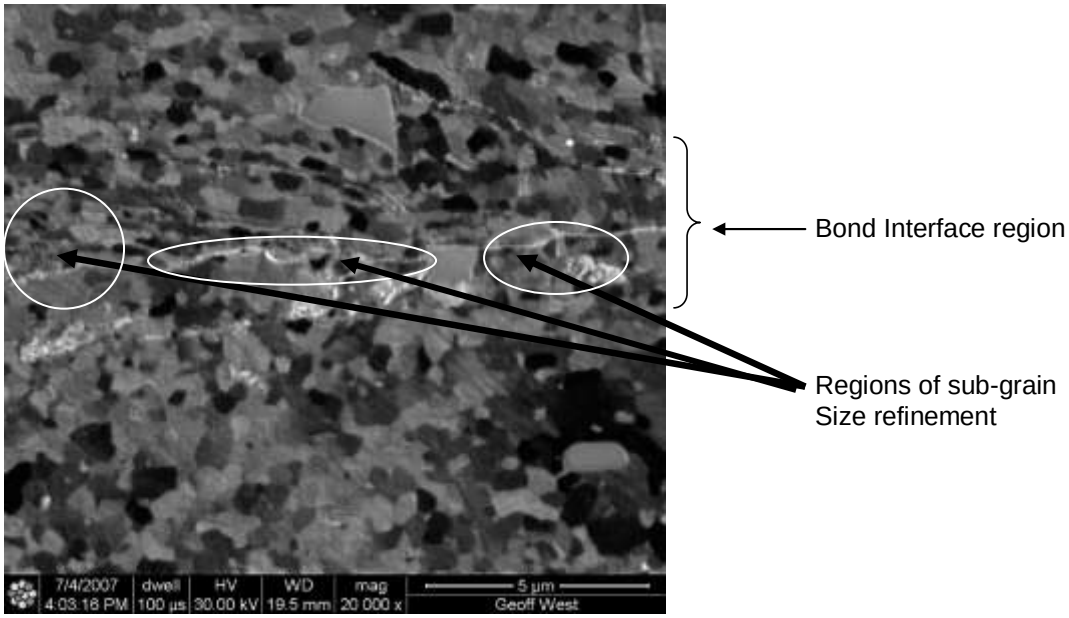

Figure 82 Ion beam induced secondary electron micrograph showing texture parallel to rolling direction showing evidence of sub-grain refinement near interface.

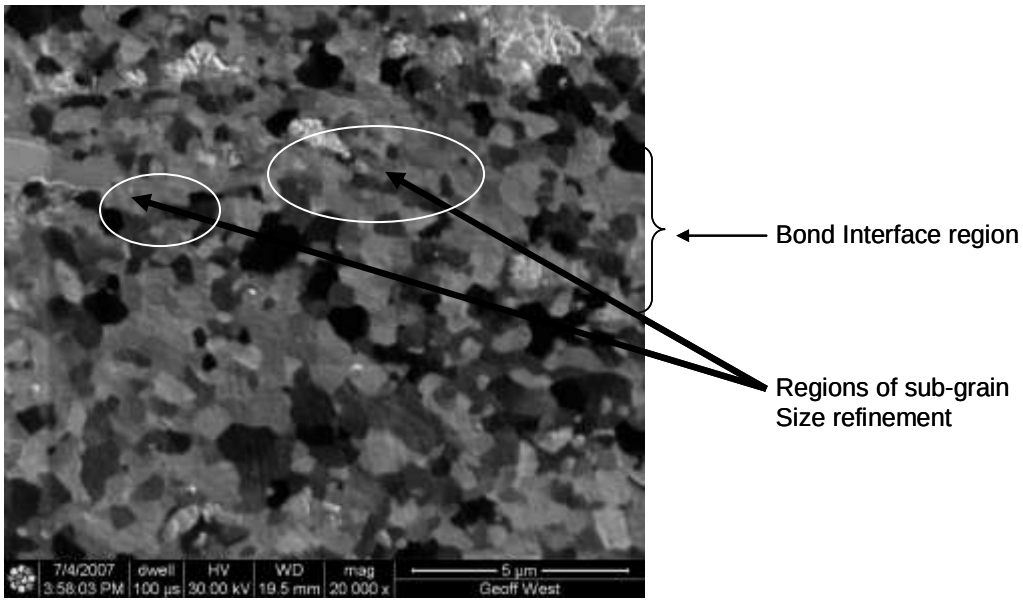

Figure 83 Ion beam induced secondary electron micrograph showing texture parallel to rolling direction where interface is nearly impossible to accurately identify visually.

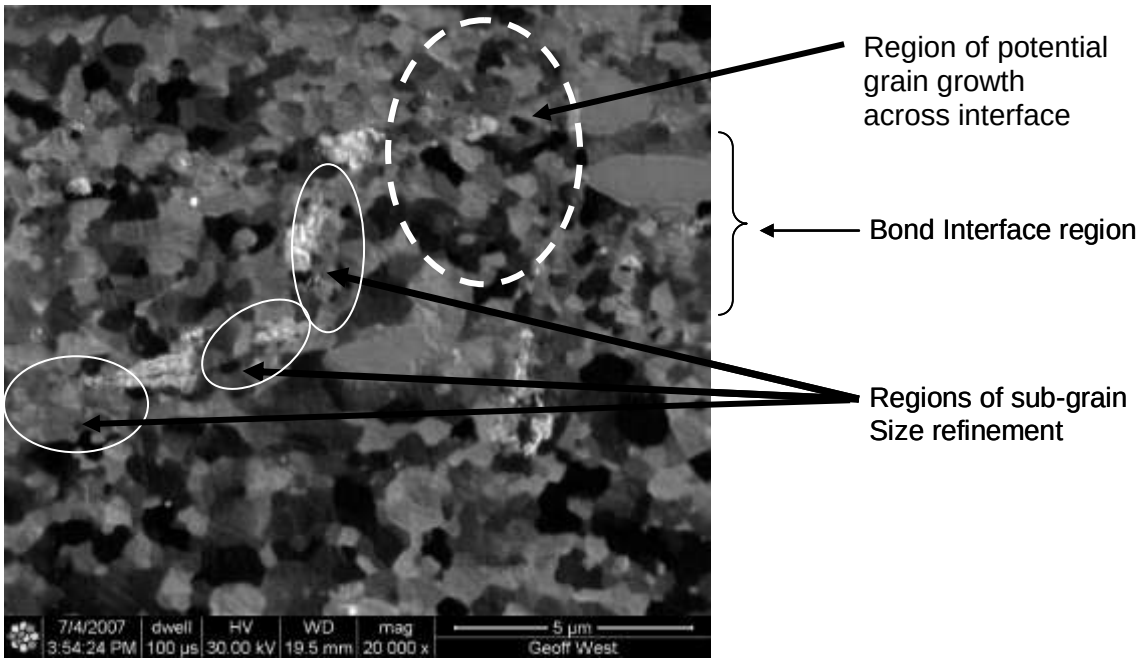

Figure 84 Ion beam induced secondary electron micrograph showing region where the texture is parallel to the rolling direction where interface is nearly impossible to accurately identify visually.

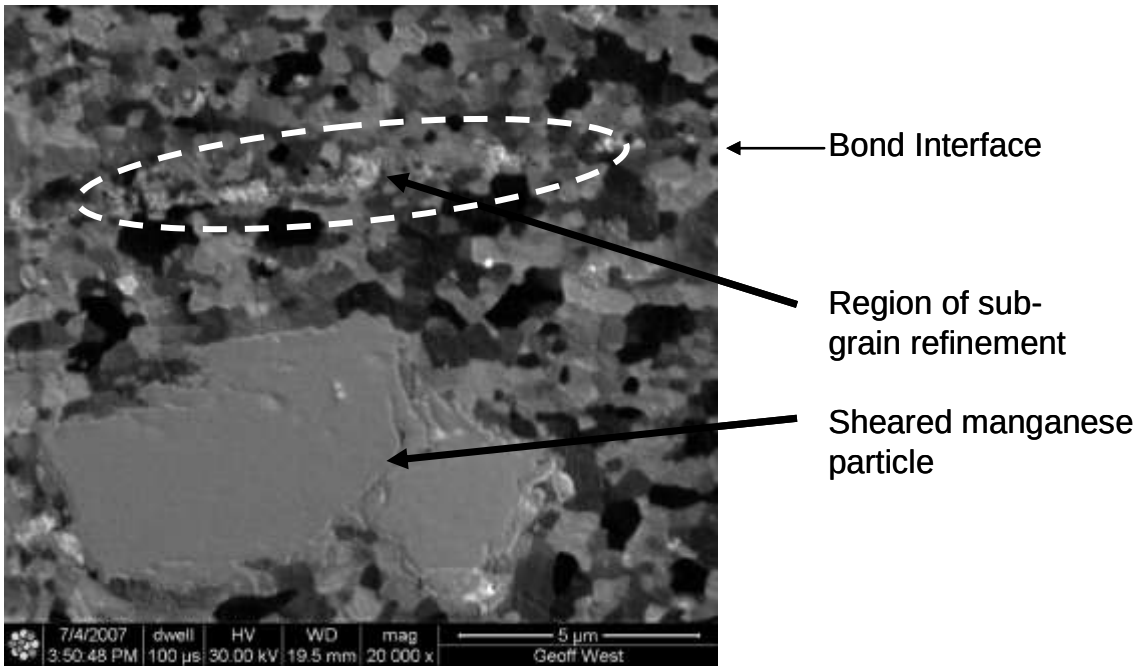

Figure 85 Ion beam induced secondary electron micrograph showing texture parallel to rolling direction where interface is nearly impossible to accurately identify visually in close proximity to sheared manganese particle.

7.4. TEM Electron Micrograph Results

It is important to note that the interface DBFIB extraction that generated the TEM sample represented the first ever opportunity to accurately select a known location in a UC specimen for use in TEM electron microscopy. Up to this point in time, it had been essentially impossible to prepare a quality UC TEM sample, let alone have any degree of confidence in the location of any specific TEM micrograph that may be produced from a sample due to the inherent anisotropic laminar structure. Thus the success of accurately extracting a known location was critical to the ultimate quality and accuracy of the results that were obtained. A TEM electron micrograph of the successfully extracted sample generated as described in section 6.1.2 is shown in Figure 86.

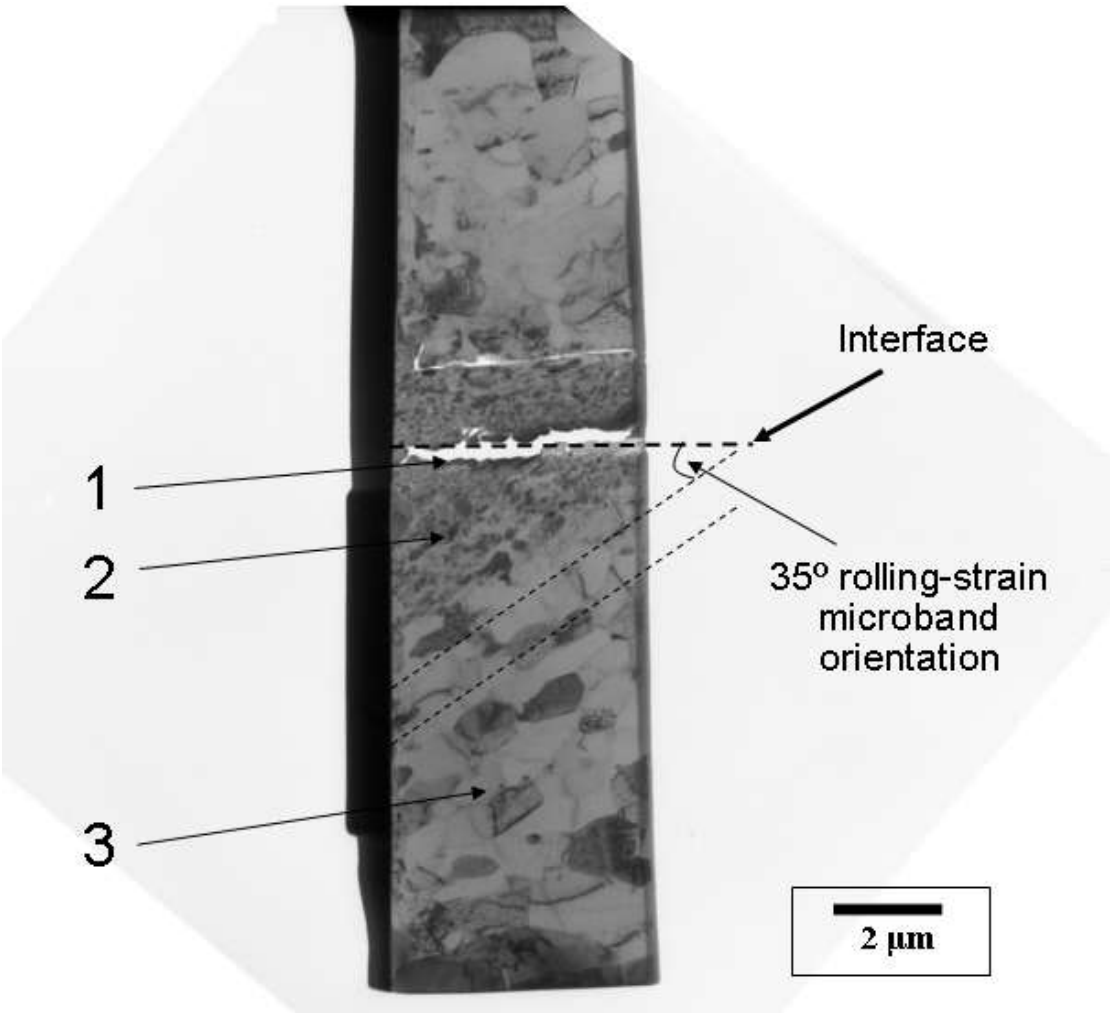

Figure 86 TEM electron micrograph of the UC interface region prepared utilizing the in-situ extraction method on the DBFIB. The numbers on the left indicate specific regions of interest and the right side highlights the dominant strain microband.

The purpose of this TEM sample was to corroborate the sub-grain refinement results of the previous sections as well as to gather evidence of interlaminar dislocations within the sub-grains. Upon immediate visual inspection there was indeed confirmed sub-grain refinement throughout the interface region, supporting the earlier DBFIB–etch results. Given this general confirmation, the TEM micrographs were next analyzed to document both the general sub-grain regions, as well as the nature of the interface itself. As a result of this analysis, three general regions of

interest were identified during the TEM sessions and identified on the left side of Figure 86:

- Region 1: ~ 5.0 $x10^{-3}$ μm
    - Oxide rich interface along the original bond interface.
- Region 2: 5.0 $x10^{-3}$ μm to 5.0 $x10^{-1}$ μm
    - Nano-scale sub-grain region with a general sub-grain size of 2.0 $x10^{-2}$ μm – 3.0 $x10^{-2}$ μm.
- Region 3: 0.5 μm to 35μm
    - Gradient sub-grain region of plastically deformed sub-grains of size: 0.1 μm to 2μm

7.4.1. Oxide Rich Interface

As previously noted, the oxide rich region came as a surprise, as the generally accepted idea that the oxides are broken up and displaced during ultrasonic welding seemed to once again be inaccurate. In the case of this sample, the oxide interface seemed to have played a role in the presence of an obvious large interlaminar void at the interface (Figure 87). While the TEM sample region that was selected came from an area that from the original surface (as viewed by an SEM) had no noticeable voids, there are typically many voids throughout a UC interface and thus it was not surprising that a sub-surface void was encountered during the in-situ extraction process.

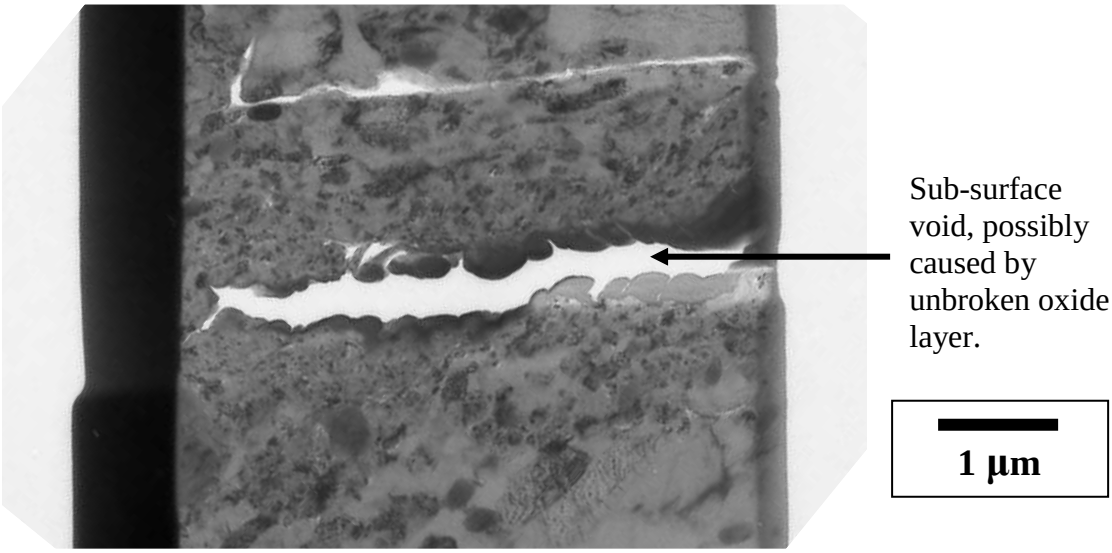

Figure 87 TEM electron micrograph identifying sub-surface void possibly caused by unbroken oxide layer.

Given this void did not appear to be caused by a local manganese particle, the sample was deemed acceptable for the purposes of the TEM analysis. The previous DBFIB-etch results support the idea that this oxide layer is not a unique artefact of the void in this sample, but rather a nearly ever-present reality within the interlaminar region of a UC bond. While it was not possible to completely isolate the exact oxide layer due to the resolution on the EDAX incorporated into the TEM equipment that was used, Table 10 provides the chemical composition that was found in and immediately around the interface. 13.77% oxygen is an abnormally large amount given there is normally not any oxygen present in the general aluminium 3003 T0 atomic composition and thus it's high concentration is indicative of what one would expect due to the influence of an oxide rich region.

Table 10 Chemical composition directly at the UC interface.

Element	Atomic%
O	13.77
Al	77.47
Cu	5.87
Ga	2.90

Table 11 provides a comparison chemical composition reading within a few microns of the interface which shows the oxygen composition had dropped from 13.77% to 1.59%. This result reinforces the clear concentration of oxides at the interface.

Table 11 Chemical composition within 1.0 - 2.0 µm of the UC interface.

Element	Atomic%
O	1.59
Al	91.38
Cu	5.74
Ga	1.28

Figure 88 shows the general region where the element composition was taken for the oxide rich interface sample using the TEM-housed EDAX system.

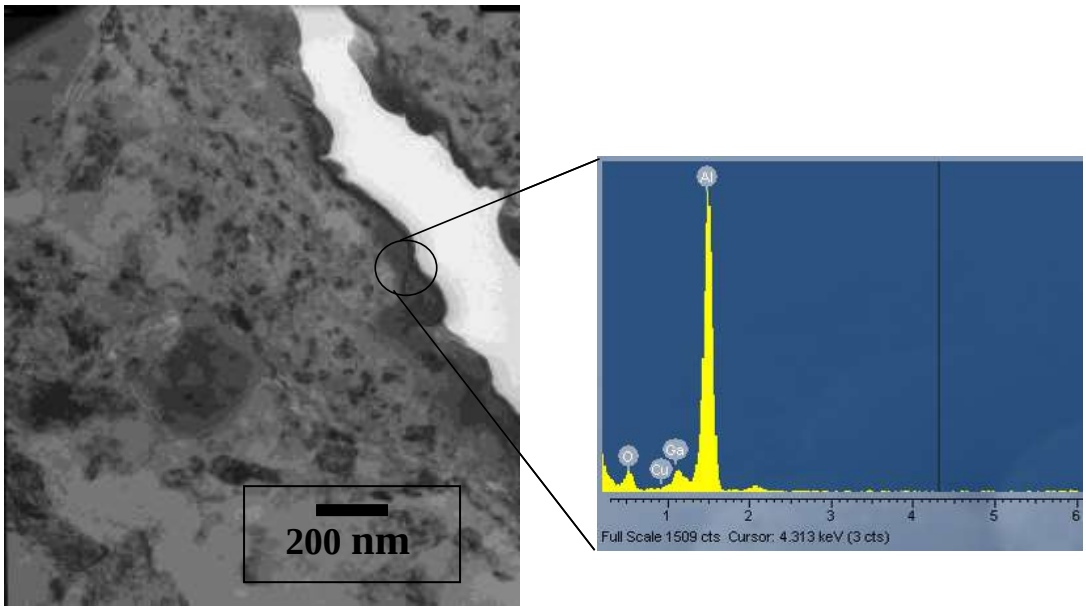

Figure 88 EDAX chemical composition sample area for oxide region shown to the right of TEM electron micrograph of aluminium 3003 T0 sample.

7.4.2. Nano-grain Region

Similar to that observed in the ion beam induced secondary electron micrographs, the nano-grain region was easily the most interesting and exciting discovery with this sample as well. Upon observing this within the TEM electron micrographs as previously discussed, it became clear that there was most definitely a decrease in sub-grain size, and that the decrease was indeed significant.

Another observation that was made concerning the refined sub-grain region was related to the overall geometry of the region. While the previous results indicated the significant influence of the interlaminar texture of the faying surfaces on the morphology of the DAZ, in this sample, there is another possible mechanism that was observed. Figure 86 illustrates a predominant 35º orientation to the sub-grain morphology. This general orientation is suggestive of a common strain microband sub-grain orientation that is consistent with many rolling processes. However, in conventional rolling processes, while the sub-grain morphology is altered, the overall

volume of the sub-grains is not reduced as is the case with a UC sample rolled with ultrasonics engaged.

7.4.3. Plastically Deformed Sub-grain Region

The final region that was studied is best described as a sub-grain region that has undergone both moderate to significant size reductions (although not to the nano-grain level) and noticeable plastic deformation. In addition to this, an additional observation was made related to the fact that there seemed to be a pronounced "step" transition between Region 2 and 3 as shown in Figure 89.

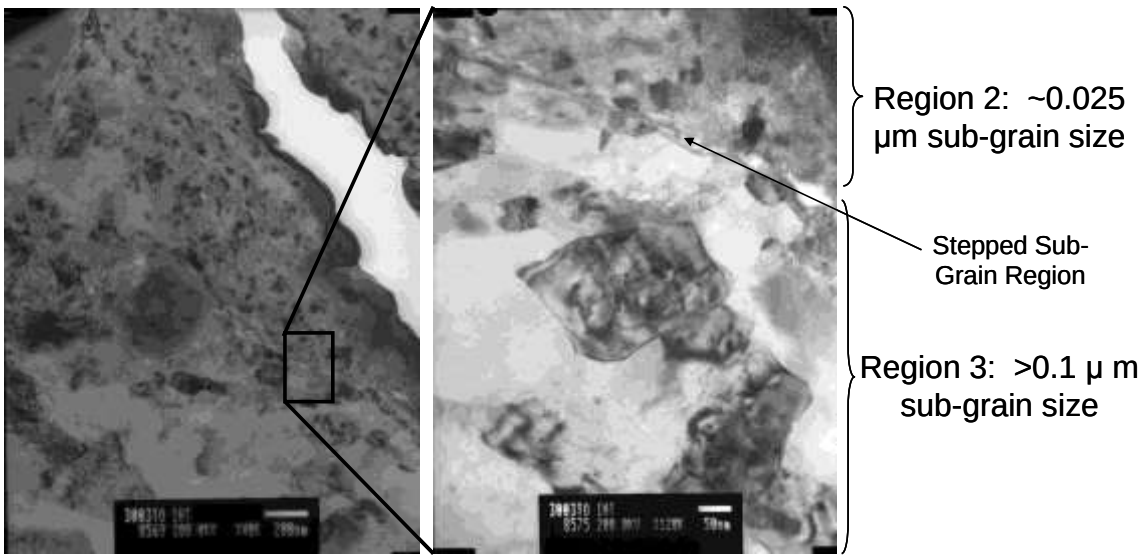

Figure 89 TEM electron micrograph of aluminium 3003 T0 sample showing detail of transition from Region 2 to 3.

7.4.4. Interlaminar Dislocations

While it was not possible to gather higher magnification TEM micrographs of actual dislocations in the nano-grain regions, it was possible to obtain such micrographs within the plastically deformed sub-grain region, around the nano-grain region,

throughout the specimen. One such TEM electron micrograph shows the presence of dislocation patterns known as persistent slip bands due to their common orientation and extended length (Figure 90).

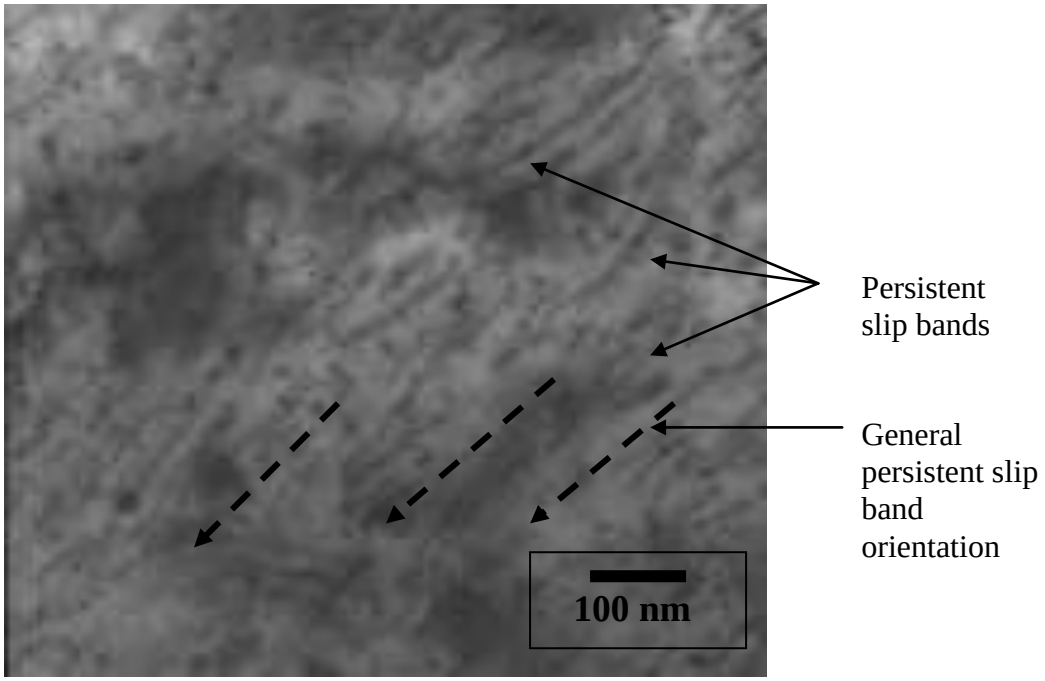

Figure 90 Persistent dislocation slip bands in UC bond area taken from TEM electron micrograph of aluminium 3003 T0 sample within 2.0 μm of the interface.

Additional TEM electron micrographs were gathered around the interface showing further evidence of dislocation-rich sub-grain structures. Figure 91 shows a TEM electron micrograph of a sub-grain within 2.0 μm of the interface. Similar to the micrograph in Figure 90, the dislocations appear to have a general directional orientation indicative of persistent slip bands.

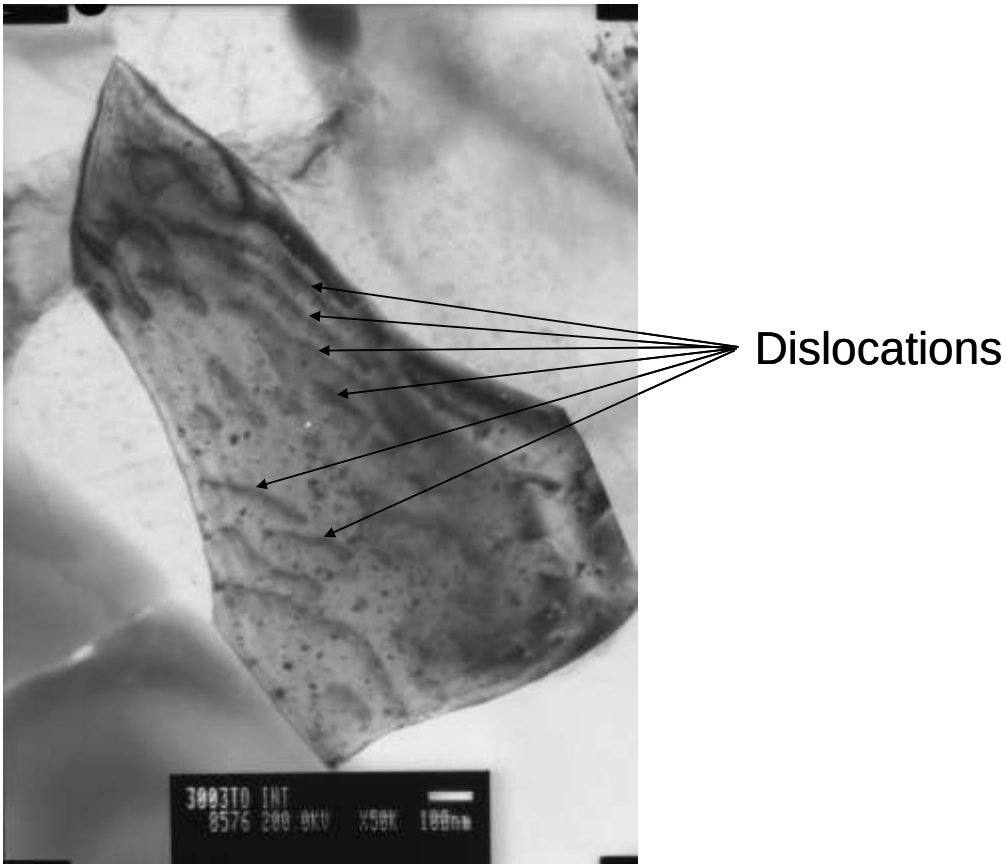

Figure 91 TEM electron micrograph of dislocations within aluminium 3003 T0 sample approximately 1.0 µm - 2.0 µm from the interface.

However, not all of the dislocation structures that were observed had a dominant orientation to them. For example, an additional TEM sample was extracted from the primary aluminium 3003 T0 3 layer stack near the mid-plane of the second foil. Figure 92 provides a representative micrograph of the dislocation structure of this region which does not exhibit any dominant dislocation orientation.

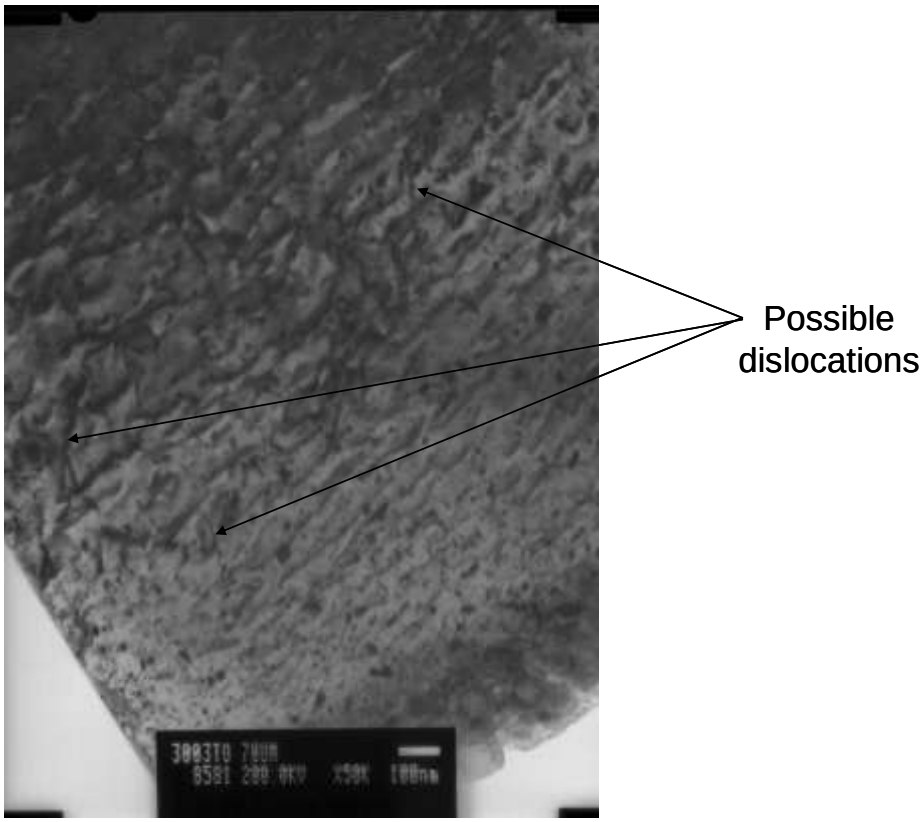

Figure 92 TEM electron micrograph of dislocations within aluminium 3003 T0 sample approximately at the mid-plane of the deposited foil (~ 75.0 µm from interface).

8. Discussion of Results

The observed sub-grain refinement and dislocation density in the UC aluminium 3003 T0 samples highlight a significant and unique metallurgical affect resulting from the UC additive manufacturing process. As will be discussed further, the results point to a general similarity to Bauschinger like cyclic softening propagation which may explain the general phenomena of interlaminar plasticity at the UC interface[67]. This effect, penetrating well into the sample, can be referred to as the Ultrasonic Bauschinger Effect (UBE) whose extent is described by the size of the UC induced DAZ. The extent of the DAZ can be thought of as any region in the sample whose morphology, or sub-grain size, has been noticeably affected by the application of the UC process, including that caused by the direct contact of the sonotrode to each deposited foil. Assessing the nature of the UBE as well as the primary attributes of the DAZ will be the focus of this Chapter.

8.1. DBFIB-etch Results Discussion

There were four key results that were documented from the ion beam induced secondary electron micrographs following the DBFIB-etching process that have particular relevance to this research and the field of ultrasonic welding in general:

- Change in sub-grain morphology
- Nano-grain formation
- Sonotrode induced sub-grain refinement
- Oxide layer persistence

8.1.1. Change in Sub-Grain Morphology

The most important result that directly supports much of the originally stated hypothesis is the documented change in sub-grain morphology at and around the interface. Whether the increase is caused by the direct contact of the sonotrode to the top of the foil or whether it is caused by the interface ultrasonic motion alone, both can be classified as ultrasonic cyclic deformation effects and constitute a UBE resulting in a UC-driven DAZ. The results further indicate that the severity of the DAZ is a function of the foil height as evidenced by the summary of the average sub-grain sizes for each of the sample regions shown in Table 8.

This conclusion is readily observable upon a simple comparison of the stunning morphology of the post-UC sample from Figure 67, and a micrograph of aluminium 3003 T0 foil that had not undergone the UC process (Figure 63). In this case the sub-grain size of the pre-UC processed foil is on the order of 30-70 μm as compared to 0.487 to 5.328 μm in the UC processed samples.

When compared to the generally non-gradient morphology of the as-rolled 0 temper foil, a plot of the average sub-grain sizes of the processed foil regions in Figure 68 visually drive home the extent to which the UC process alters the microstructural nature throughout the sample. Even the maximum sub-grain size of the UC processed foil would appear to be well below the typical sub-grain size in the unwelded material.

Another interesting note is the generally high standard deviation throughout the sample (Figure 93). Most regions had a sizeable difference between their lowest and highest data points highlighting a highly non-equiaxed morphology throughout the samples. The general exception to this was in the nano-grain regions where the consistency was much higher and thus the standard deviation was much lower. It is

important to note however, that due to resolution limitations within these regions, there may be some latent error that is simply not apparent with the current method.

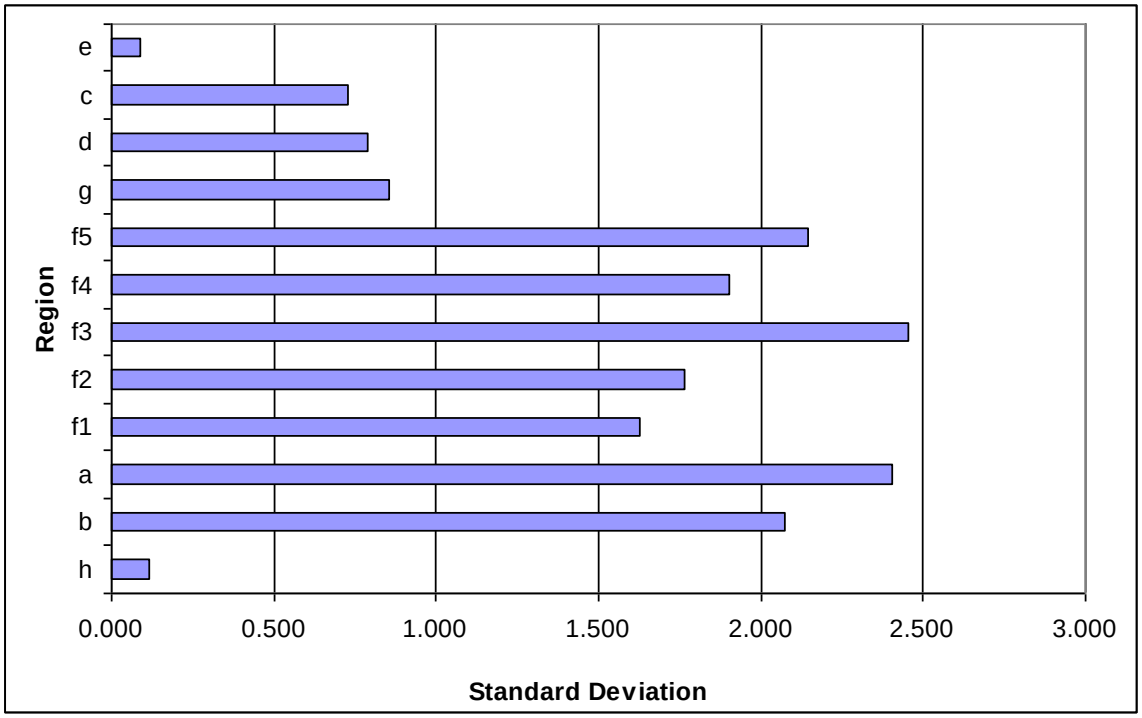

Figure 93 Standard deviation by region illustrating the relative degree of variability in the sample regions.

An additional point of note is that the amount of sub-grain refinement probably caused by the direct contact of the sonotrode to the top of the foil (regions c, d, g) is much greater than that caused by the interface dynamics alone (ie. bottom of the foil in regions a, b). Region b for example has a sub-grain size that was 45.4% greater than that of region c. The ability of ultrasonics to achieve such novel microstructure simply by application of the rolling sonotrode, additive deposition applications aside, is of great interest from the standpoint of materials engineering in general. For example, such ability may prove useful in surface treating materials for industrial high wear and fatigue sensitive applications. Additionally, this method may prove valuable in producing novel additive manufactured articles if the parameters

could be engineered to propagate the nano-grain regions throughout the entire part. This could theoretically be accomplished through the use of very thin layers of foil.

If the decrease in sub-grain size does indeed produce an increase in stored energy within the material, there are additional material processing benefits that may be useful in post UC part fabrication heat treating operations. For example, it may be of interest to utilize the UC process to bond dissimilar materials together for a specific multi-material laminate application. Once bonded, a user could thermally treat the laminate in an attempt to create diffusion, resulting in novel interlaminar alloys that may prove difficult to produce conventionally. In these instances the presence of such high amounts of stored energy would potentially aid in the diffusion process.

8.1.2. Nano-grain Formation

The second significant observation was the formation of nano-scale grain regions within the UC laminate. While much of the nano-grain formation appeared to be related to the cyclic work done directly by the sonotrode contact, the work described in Section 7.3 that removed this effect demonstrated that the UC process does appear to form such regions at the interface as well (although in smaller amounts). This previously undocumented post-UC material attribute is of particular significance as nano-grains in general possess unique material properties that may influence the bonding process.

For example, nano-grains may in fact retard the bond quality of subsequent layers due to their increased hardness. Thus a relatively soft 3003 foil may develop the hardness of a much stronger material through the extensive cold work done to it through the nano-grain formation process and resist subsequent layer depositions. However, given that nano-grain metals have been shown to often possess desirable

engineering properties for certain applications (such as high wear surfaces for aerospace applications), future research may be pursued to maximize their volume fraction in a UC rapid manufactured article.

8.1.2.1.Texture Influence on Nano-grain Formation

An additional observation of significance was the correlation of nano-grain formation to the general topography of the interface. While it has already been discussed that the geometry of the sonotrode and the contact mechanics with the foil appear to influence certain aspects of the nano-grain formation locations, the nano-grain formations unrelated to the sonotrode contact seem also to be highly geometry or "obstacle" driven. For example, the micrograph in Figure 94 clearly demonstrates how the nano-grain formation on the bottom of the new foil is affected by the asperity of the substrate. While this sample is not one of the samples were the sonotrode sub-grain refinements were removed, the nano-grains of interest in this case are on the previously untouched bottom of the new foil.

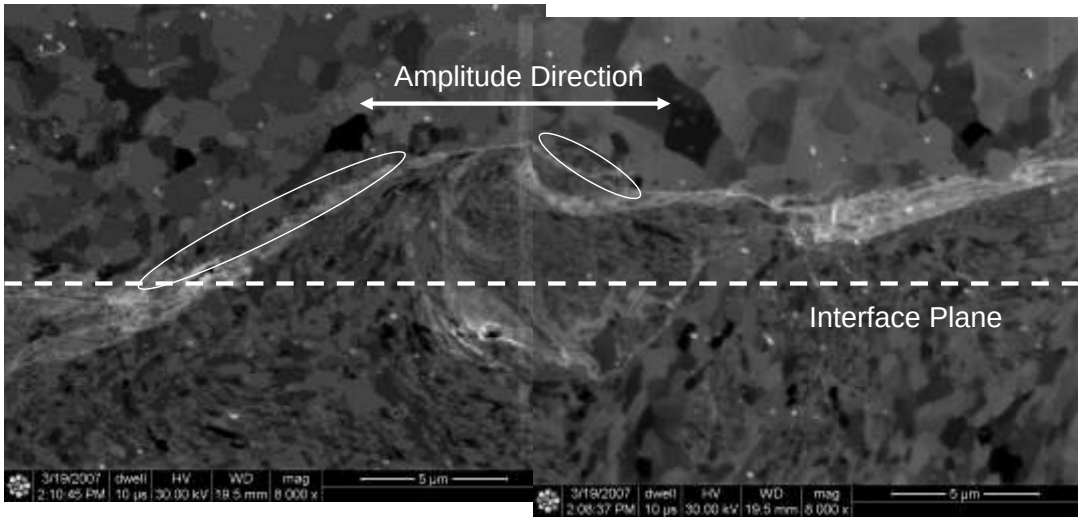

Figure 94 Ion beam induced secondary electron micrograph showing interface geometry impact on nano-grain region formation. Regions at high incidence angles to normal layer interface plane highlighted by white ovals.

The influence of the substrate geometry is further buttressed when a relatively smooth interface section is analyzed. Figure 95 illustrates the lack of sub-grain refinement on the bottom of new foils when they are in direct contact to relatively smooth substrate surfaces. In this case the smooth to smooth region was not specifically engineered and simply occurred randomly. Figure 77 illustrates the same point for the case where the previous layers sonotrode sub-grain refinement was removed and a smooth to smooth interface was engineered.

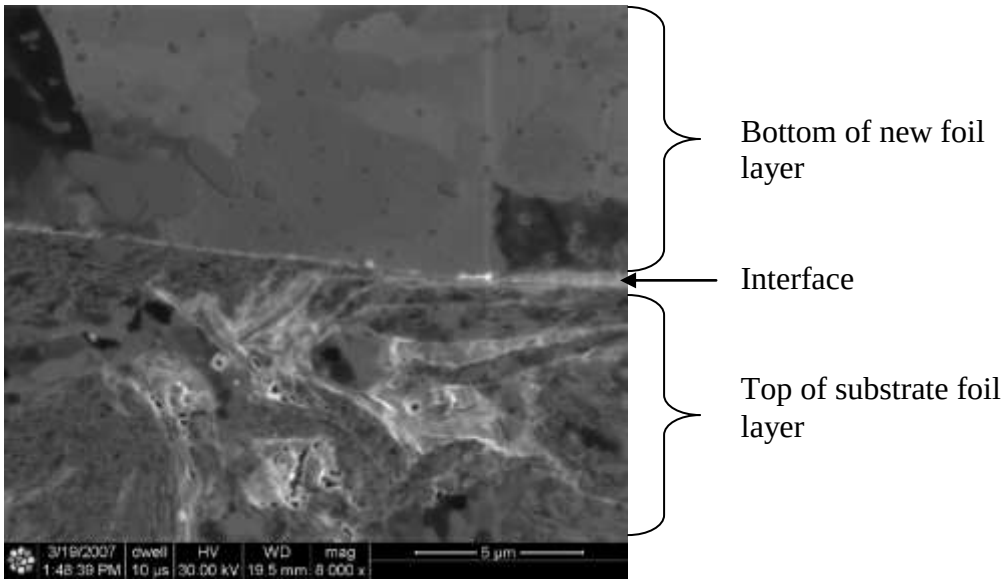

Figure 95 Ion beam induced secondary electron micrograph showing relatively flat interface region showing no signs of nano-grain formation or significant sub-grain refinement on bottom of new foil (region within yellow circle).

A confounding element to the issue of interlaminar texture relates to the approach utilised to eliminate relative motion between the sonotrode and the foil. In practise, a rough sonotrode texture is necessary to maintain mechanical coupling between the sonotrode and the top of the new foil layer. The sonotrode contact surface subsequently transfers its texture to the top of the foil, creating an asperity rich topography that becomes the new substrate. Such significant modifications to the surface roughness have been shown in this research to influence the sub-grain

structure, which generally support macroscopic level results of previous texture research in the ultrasonic field. One such example of the influence of interface texture was noted by Riben when he showed that a surface roughness of more than 30 μ inches was highly undesirable at the interface and roughness of 3 μ inches or less was preferred during ultrasonic bonding of Al-Al and Al-Au[79]. This may be due to the fact that at a certain interlaminar roughness the system achieves its ideal critical resolved shear stress for slip and material softening rapidly progresses.

As previously discussed, developing a sonotrode texture that meets the requirements of sonotrode to foil contact that also results in desirable interlaminar dynamics has proved challenging. The other practical issue is that even if a rough sonotrode texture is shown to be ideal, it would be difficult to maintain a high friction surface on such a sonotrode surface over time due to the increased wear, especially if the material being joined is a harder material (such as with titanium foil). Tool steel sonotrodes have been shown to last longer with rougher textures but their utility is limited due to their higher mass/inertia (that constrains sonotrode diameter) and their higher rate of fatigue failure when placed into aggressive commercial use.

8.1.2.2. Reverse Hall-Petch Relationship

As previously noted, the sub-grain refinement resulting from the UC process may also be creating a harder material. This hardening effect due to the grain size is known as the Hall-Petch relationship[80,81]. This relationship says that the larger the grain size of a crystalline material, the lower the yield strength. However, this work was established for grain sizes in the millimetre through submicron regimes and not the nano-millimetre regime that has now been documented. Recent computer simulations

have pointed to the potential of a reverse Hall-Petch relationship as grain sizes become small where material hardness and yield stress begins to decrease.

This issue is of great interest in this research as it may shed significant light on the nature of the plastic flow now that it is apparent that nano-grain formation exists. With the Hall-Petch relationship, the grain boundaries are believed to act as obstacles to dislocation glide as they would require larger amounts of energy to overcome these barriers. However, for very small grains (~12 ηm) the deformation mechanism is potentially different. It has been proposed that in this case plastic deformation is no longer dominated by dislocations penetrating grain boundaries but by the sliding of grain boundaries themselves[82]. With these small grains the sliding effect would dominate because of the larger ratio of grain boundary to crystal lattice, potentially resulting in a softening effect.

Even if the vast majority of nano-grain formations are the result of the prior work of the sonotrode, these fine structures may potentially be easily reactivated once additional layers are deposited. This would imply that the grain refinement being done by the sonotrode may actually be serving as a catalyst to interlaminar plastic flow throughout the UC build process.

8.1.3. Sonotrode Induced Sub-grain Refinement

The third area of interest, suggested earlier, is the observed high degree of sub-grain refinement that appears to result from the direct contact of the sonotrode to the top of a new foil layer during the foil deposition cycle. As noted in the previous chapter, the degree of sub-grain refinement seemed to be directly influenced by the general topography of the sonotrode surface texture itself, and then the transferred texture in turn contributed to the dynamics of the following layers interface region. The results

indicate that there are perhaps three general conditions that relate to the sonotrode texture and the refinement of sub-grains. These three conditions are illustrated in Figure 96 and are described as follows:

1. Region 1: Direct contact of a sonotrode surface (such as a peak) to the surface of the foil. In this case the local stress would be highest and the local cyclic strain may be transmitted directly into the material where it would quickly lead to the formation of highly refined sub-grain regions.
2. Region 2: Areas of relative motion in and around the direct contact regions. In areas, particularly more horizontal surfaces, that are in less rigid contact with the sonotrode, there also exists the potential for sub-grain refinement. However, sub-grain refinement in these regions may also be countered by recrystallization due to higher local temperatures from the frictional heat that would be developed from the sliding surfaces (not currently observed).
3. Region 3: Non contact regions. Clearly there were areas, presumably opposite valleys in the sonotorode topography, which never came into contact with the surface of the foil. In these regions it was evident that very little sub-grain refinement occurs. Interestingly, these areas, being higher than the surrounding areas, would become the first to make contact with the subsequent deposition of the next foil.

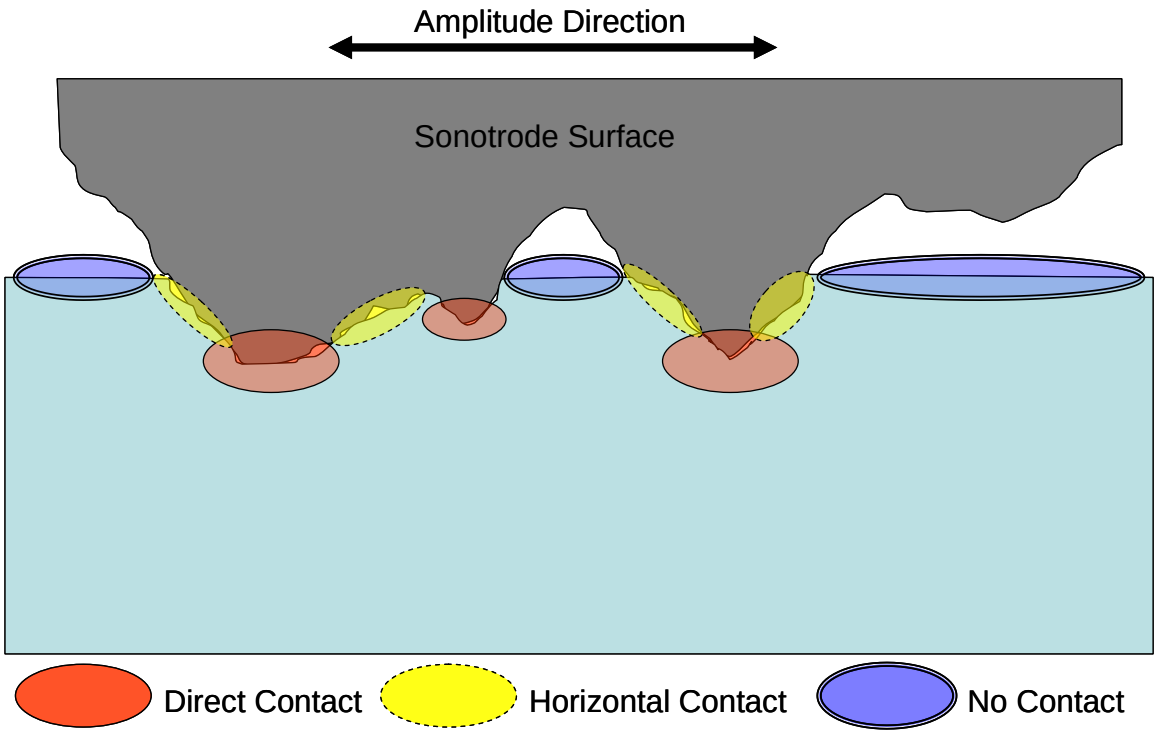

Figure 96 Illustration of regions of sonotrode contact to the top of a foil layer being deposited during the UC process.

Figure 97 shows a series of actual ion beam induced secondary electron micrographs of the top of the three layer sample that illustrate this idea. Note how Region 3 in the figure would seem to have not come into any contact with the sonotrode due to its flatness. This fact also increases the chance that it will be the first part of the region to make contact with the bottom of subsequent foil depositions.

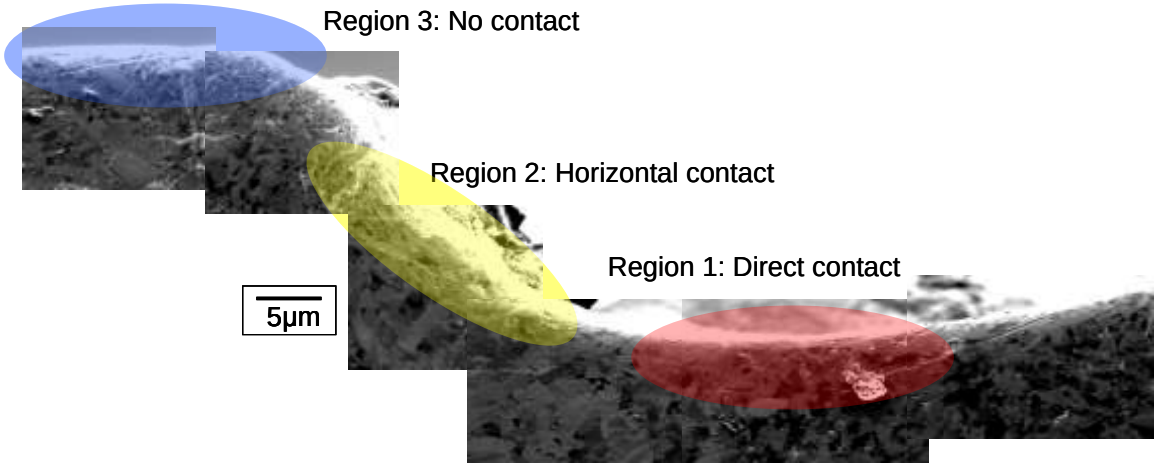

Figure 97 Top surface of aluminium 3003 T0 sample showing sub-grain effects of sonotrode contact.

The fact that so much sub-grain refinement occurred at the sonotrode surface indicates that much of the energy in the overall UC system is being dissipated at that specific interface. It would seem imperative to reverse this result to achieve a greater bond quality at the actual weld interface. Figure 98 illustrates three different theoretical cases where the relative motion and resultant cyclic cold work may occur in the UC system. It would seem at this time that Figure 98c represents the likely scenario that is currently observed.

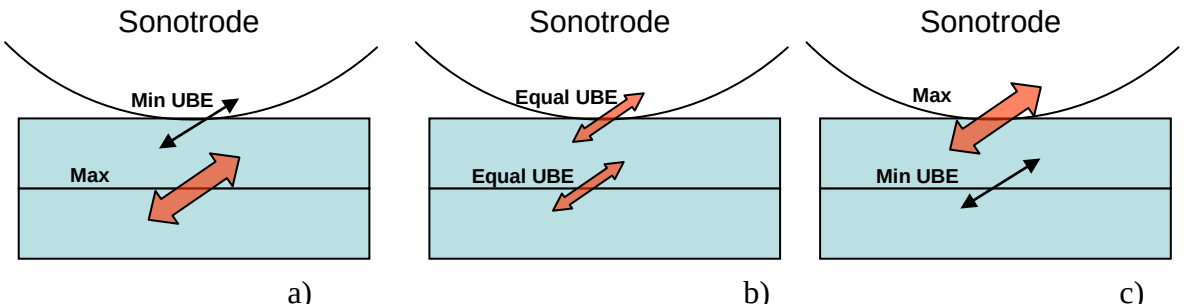

Figure 98 Localization of relative motion in UC system. a) cyclic cold work dominant at weld interface, b) equal amounts of cold work at interface and sonotrode, c) dominant cyclic cold work between sonotrode and top of foil.

Depending on the application and/or the desired interface dynamics, it is logical to assume that a particular outcome could be fully engineered in the future. For example, pre-treatment of the bottom of the new incoming foil layer may lead to increased grip at this interface resulting in increased mechanical coupling between the two interfaces. Given that it is still unknown whether or not rough textures are desirable (and indeed they may be for some applications yet not for others), it is difficult to suggest the most advantageous sonotrode texture at this time.

8.1.4. Oxide Layer Persistence

The final point of significance from the DBFIB-etch results is the fact that the oxide layer appeared to be nearly unbroken throughout the samples when observed following the DBFIB-etch process (also supported by the TEM results). This observation is significant in that essentially all of the current literature on the topic describe ultrasonic welding processes as "quickly breaking up the surface oxides", which leads to direct metal to metal contact and rapid bonding. In light of the fact that much, if not all, of these published results relate to ultrasonic spot welding, it does not necessarily prove their conclusions wrong, it may simply point to the differences between spot welding and UC welding dynamics. Figure 99 presents a typical illustrated method in the literature of demonstrating the commonly held idea of oxide dispersion. (It is additionally interesting to note that this author does not illustrate any sub-grain refinement whatsoever, reiterating the novelty of the present research results to the general ultrasonic welding community.)

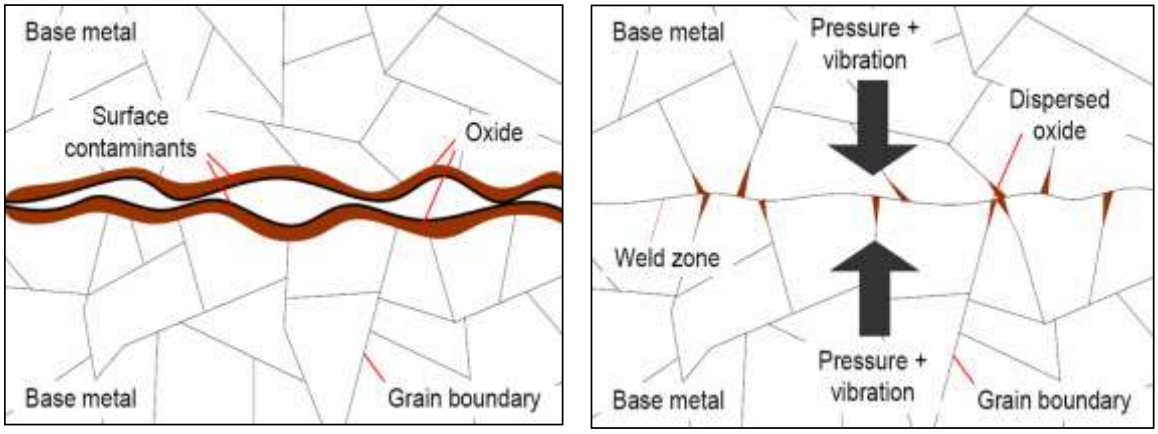

Figure 99 Previous common representation of theoretical dispersion of surface oxides during ultrasonic welding[83].

In stark contrast to this conventional idea of broken and dispersed oxide, Figure 100 shows the clear oxide-rich interface (in white) using ion beam induced secondary microscopy following DBFIB etching. It is important to note that this boundary was not readily visible using an SEM electron microscope alone and thus previous research in the field would have had no way to observe this. This issue is of great importance as it directly relates to not only bond quality, but also to the ability to conduct post weld heat treatment as may be desired for functional direct manufacturing articles as a persistent oxide barrier may slow or completely inhibit diffusion processes.

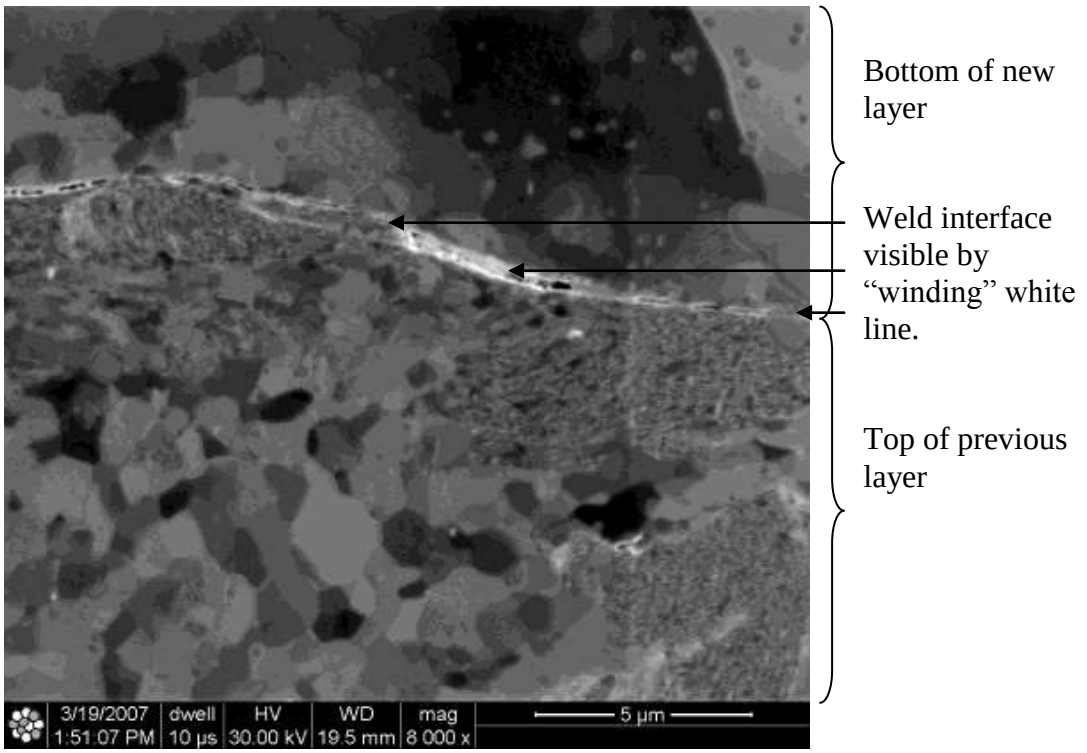

Figure 100 Ion beam induced secondary electron micrograph of UC interface showing clear oxide boundary between previous (bottom) and new layer (top).

As noted in the previous section, there would appear to be significant amplitude losses at the sonotrode/foil interface, thus there is presumably less relative motion at the interface itself, which may be the root cause for the inability of the UC process to disburse the oxide layer. It is important to note that in ultrasonic spot

welding (the focus of much of the current technical publications), the higher forces and longer dwell times that are involved may overcome this issue. However, due to the need to keep the sonotrode moving at a reasonable rolling speed in UC (to facilitate the overall cycle time for making an additive manufactured article), maintaining long dwell times is clearly a process challenge.

An additional key contributing factor may also be the "ultrasonic effect" on the coefficient for friction at the interlaminar region. The rationale for this suggestion is the fact that the sliding friction between contacting surfaces have been shown to be influenced by the application of ultrasonic vibration[84,85,86,87,88,89,90,91,92,93]. Most of this research has been directed at the potential of using this phenomenon to enhance manufacturing process efficiency in processes such as drawing, extrusion and forming. Schey[94] has classified the beneficial effects of ultrasonic vibration in manufacturing processes into two primary segments: reduction in strength of the material, and reduction of interfacial friction. Both of these traits would potentially inhibit the ability of the mating surfaces to generate sufficient "oxide penetration stresses" and/or interlaminar galling, likely necessary to disrupt the oxide layer.

Frederick noted that ultrasonic vibrations cause a reduction in friction because 1) they apply an additional contact stress to aid in breaking the instantaneous welds that occur during contact, 2) they reduce the time that any two asperities on opposite surfaces remain in contact, keeping them from forming a stronger weld[13] or as this author contends, overcoming oxide barriers. Frederick further notes that in unpublished experiments conducted at the University of Michigan he observed that two metallic surfaces vibrating at ultrasonic frequencies with respect to each other had an effective coefficient of friction of less than 0.001. If true, such a drastically low coefficient would further cast into doubt common characterizations of ultrasonic

welding as a micro-friction process and inhibit the interlaminar dynamics required to achieve true metal to metal contact.

An interesting question thus arises relating to how one might increase friction at the interface to achieve better oxide disruption and theoretically superior weld quality. Kumar[95] may have provided the best illumination on the topic through his studies on the affects of amplitude upon the frictional force of a variety of metals including aluminium. What he observed was that there was a noted decrease in the frictional force as the amplitude increased as seen in Figure 101. He plotted the frictional force against amplitude of transverse vibration for different pin materials (a) aluminium, (b) brass, (c) copper and (d) stainless steel, sliding against a tool steel counter surface at 20 kHz. The mean sliding speed was 50 mm s^{-1}.

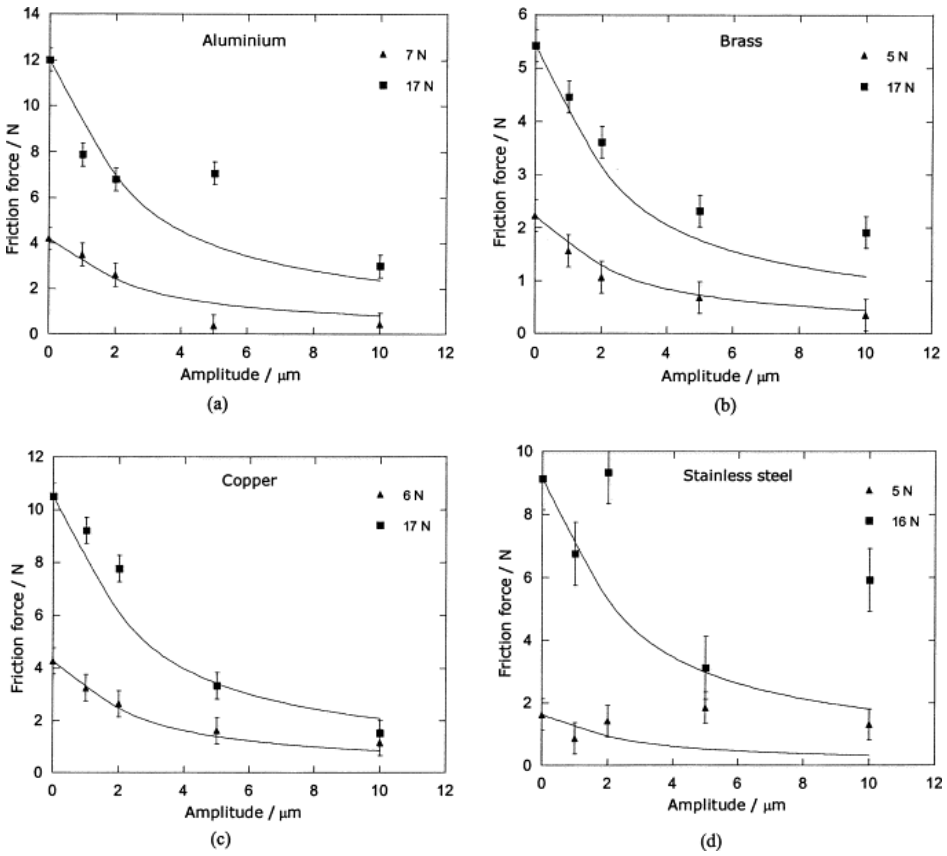

Figure 101 Friction reduction as a function of amplitude for (a) aluminium, (b) brass, (c) copper and (d) stainless steel.

Kumar concluded that ultrasonic vibration can be used to reduce the sliding friction between interacting surfaces by a large amount in either a longitudinal or transverse direction by increasing the amplitude. Conversely, decreasing the amplitude would have the effect of increasing friction, yet simultaneously minimizing the potential formation of nano-grain colonies and persistent slip bands.

As a cautionary note, Storck[96] seemingly countered key elements of results such as these when he developed a separate analytical model designed to determine friction reduction using ultrasonic's. His theoretical approach was based on Coulomb's friction law and it sought to describe macroscopic friction reduction observed in ultrasonic applications. Counter to many other research results on this topic, Storck's work noted that the widespread practice of adopting the coefficient of friction affect of ultrasonics was a consequence of poor kinematical modelling and should not be attributed to miraculous unknown "high frequency friction mechanisms".

8.2. TEM Results Discussion

The current body of research using TEM to analyze ultrasonic welds can essentially be segmented into two distinct eras, pre-DBFIB, and post-DBFIB. As there are relatively few DBFIB machines currently available, the research community is currently in a transitional phase with regard to its use. As noted earlier, the use of a DBFIB device allows the unprecedented power to accurately isolate a sample from the ultrasonic interface due to its ability to extract a small (~20μm x 5 μm x <1 μm) TEM specimen from a known location (ie. the actual interface). Previously, attempts to isolate the interface proved highly challenging and cast into question the value of

many earlier TEM electron micrographs and the conclusions that were often drawn from them.

The TEM electron micrographs that were gathered during this research were critical in confirming the decrease in sub-grain size at and around the UC interface that was observed in the ion beam induced secondary electron micrographs. Additionally, several of the higher magnification TEM electron micrographs showed highly directional persistent slip bands (PSB) that were similar to previous Bauschinger test sample results, another key tenant of the hypothesis. Within the UC process, these PSB's are likely to occur along the initial preferred dislocation paths, that due to the overall rolling motion within the UC process, may also correlate to the known 35 degree roll strain path effect. Or, as discussed earlier, they may also be oriented in the <110> direction of slip in the aluminium fcc lattice structure along the close packed {111} planes. Figure 90 shows an excellent example of directional PSB's identified during this research.

The TEM electron micrographs were also useful in providing the highest quality micrographs of the three interlaminar regions within the UC laminate. It is important to note that the DBFIB-etch results showed that the nano-grain region can occur in many places near the interface and thus these three regions do not necessarily progress one after the other, rather, they are general region types to provide an additional characterization perspective. The following general region types were identified during the TEM sessions (shown in Figure 86).

- Region 1: ~ 5.0×10^{-3} μm
    - Oxide rich interface along the original bond interface.
- Region 2: 5.0×10^{-3} μm to 5.0×10^{-1} μm
    - Nanoscale sub-grain region with a general sub-grain size of 2.0×10^{-2}

μm – 3.0 x10^{-2} μm.

- Region 3: 0.5 μm to 35μm
    - Gradient sub-grain region of plastically deformed sub-grains of size: 0.1 μm to 2μm

8.2.1. Bauschinger Sample Stored Energy Correlation

The TEM electron microscopy results also showed similarity to previous work that explored the effect of dislocation structure on torsional cyclic Bauschinger tests on annealed steel[97]. Due to the rolling forces involved in the UC process it could be argued that the dynamic straining effect is somewhat torsional in nature. This similarity is due to the fact that every ultrasonic cycle is creating a two dimensional strain path due to the lateral amplitude forces and the perpendicular rolling forces. Figure 102 shows the dislocation structure of an annealed steel sample prior to the application of torsion Bauschinger cycles. Note that in this sample there were very few dislocations and no observable sub-grain boundaries (implying sub-grain size of much larger than 10 μm given the scale of this micrograph.

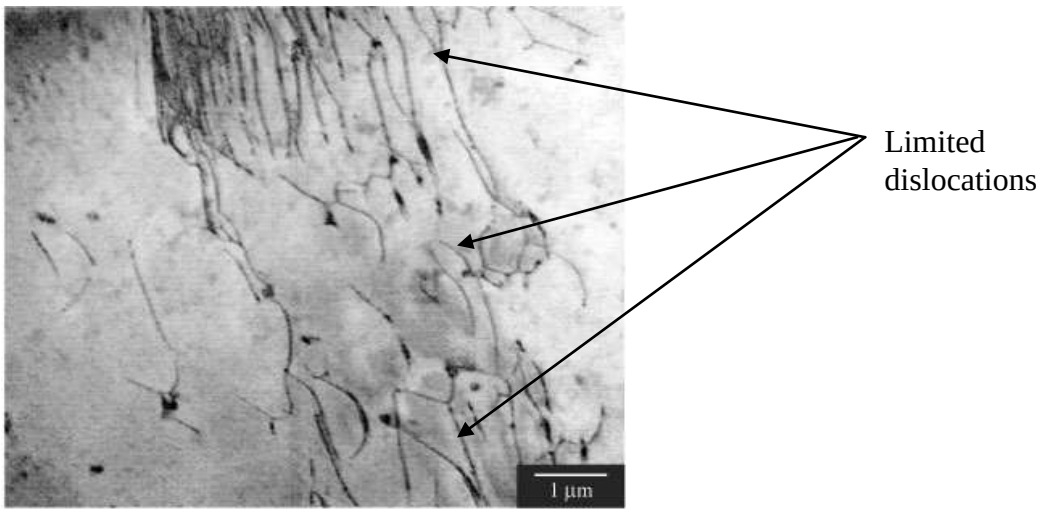

Figure 102 TEM electron micrograph of annealed steel[97] prior to cyclic Bauschinger tests. Note the absence of any grain boundaries at this magnification.

The complex sub-structure that formed from only 10 torsion cycles in Figure 103 shows similarity to that observed in the UC samples. In this micrograph there are dozens of new sub-grains that have formed in addition to a high concentration of dislocations. This supports the idea that the Bauschinger Effect is present within the UC process and implies that its effect can be observed in far fewer cycles (10) than the common process settings of over 400 within UC. Further understanding this dynamic may lead to significant reductions in UC processing time, critical to its expanded use within industry.

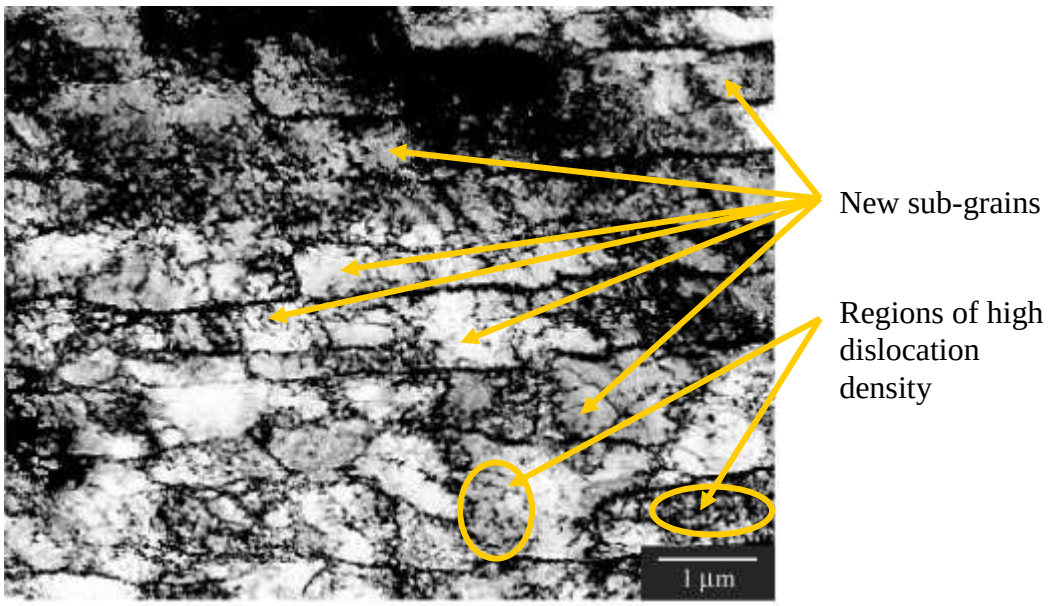

Figure 103 TEM electron micrograph of annealed steel submitted only to cyclic torsion (11.2% strain per cycle, 10 cycles).[97]

8.2.2. Transient Grain Refinement and Lattice Realignment Theory

One potential explanation for the sub-grain refinement in UC could be tied to a transient grain refinement and lattice realignment phenomena. This theory, put forth by the author, would suggest that after each of the sonically timed motions/strain, an ever increasing number of small-sub grains form and reorient, allowing for an ever

increasing volume fraction of lattice alignments that favour the propagation of persistent slip bands further into the material. The potential for such behaviour is made clearer when one considers the number of unique strain cycles that the UC process induces in a very short period of time. The number of cycles and the effective dwell time in which they occur is calculated as follows:

UC Frequency	= 20kHz
Estimated Contact Zone	= 750 μm
Sonotrode velocity	= 30 mm/s
ξ = Cycles per contact zone	= cycle rate * contact zone area
cycle rate	= (20,000 cycles/s)/((30mm/s)*(1mm/1000 μm))
	= .667 cycles/μm
ξ	= (.667 cycles/μm) * (750 μm) ~ 500 cycles
Elapsed Time	= 500 cycles / (20,000 cycles/s)
	= .025 s = 25 ms

Thus a typical UC interface region will experience 500 unique cycles in only 25 ms. As a result, those materials with many slip planes such as fcc materials, would potentially see near instantaneous sub-grain reductions and nano-level realignments favouring further plastic deformation and dislocation transport. Conversely, materials that have far fewer active slip planes such as hexagonal close packed, would resist such sub-grain formation and realignment. This would also result in a highly transient stacking fault energy value, perhaps reducing it significantly.

Further supporting this concept are studies that have shown the effect grain orientations have on the friction and wear behaviour of materials in general[98]. For these studies, an automated orientation imaging analysis system was used to identify orientations of grains in polycrystalline specimens and then micro-friction tests were carried out using a Triboscope, a combination of nano-mechanical probe and atomic force microscope with an electrochemical cell. The micro-friction tests indicated a

significant dependence of friction coefficient on crystallographic direction and orientation of grains, and thus if there exists an ultrasonically induced preferential grain realignment then the dynamic contact conditions would quickly be altered.

Supporting this idea further was Bateni[98], who conducted additional micro friction tests along different crystallographic directions inside different grains. These and similar results have shown that the coefficient of friction for individual grains not only depends on crystallographic orientation[99], but that the coefficient of friction for higher atomic density planes is lower than that for lower atomic density planes[100]. In the case of fcc crystals, that would mean that the plane of high crystallographic friction would exist in parallel along the close-packed {111} planes, where slip and shear takes place most often. Therefore, if the UC process reorients the sub-grain structure in such a way that the active slip direction is dominantly parallel or perpendicular to the direction of sliding, the friction coefficient would either significantly decrease or increase respectively.

8.2.3. Nano-grain "stepped" Transition Region

An additional area of great interest notable in the TEM micrographs (and supported by the high magnification SEM micrographs) is the apparent "stepped" regional transition that occurs between the nano-grain region and the much larger sub-grain region noted as Region 3. This same phenomena was also observed in and around all of the nano-grain regions within the ion beam induced secondary electron micrographs. Such a distinct transitional affect would seem to point to the existence of a preferred energy state within the aluminium sub-grain structure that once exceeded, "transforms" near instantly to the nano state at which point the dislocation transport is likely to progress easier through the grain boundaries themselves than

through the actual grains. This would correlate with the previously discussed reverse Hall Petch relationship. Another way to consider this would be that the material possesses a sub-grain "breaking point" where it "jumps" from an average of 3.0 x 10^{-1} μm to 2.0 μm size all the way down to a ~ 2.0 x 10^{-2} μm size with few transitional sub-grains in between. Figure 89 shows the stepped transition region at higher magnification.

During the final stages of experimentation several additional micrographs were obtained to provide additional views of this stepped region by combining a DBFIB-etched pit, with high resolution SEM electron microscopy. A sample of one of these micrographs is presented in Figure 104. The transition area is extremely clear in this micrograph and the "boundary" continued for over 10 μm, generally following the line of the actual weld interface. This area was probably in direct contact to the sonotrode during the deposition of that specific layer, resulting in an enormous amount of cold work and sub-grain refinement.

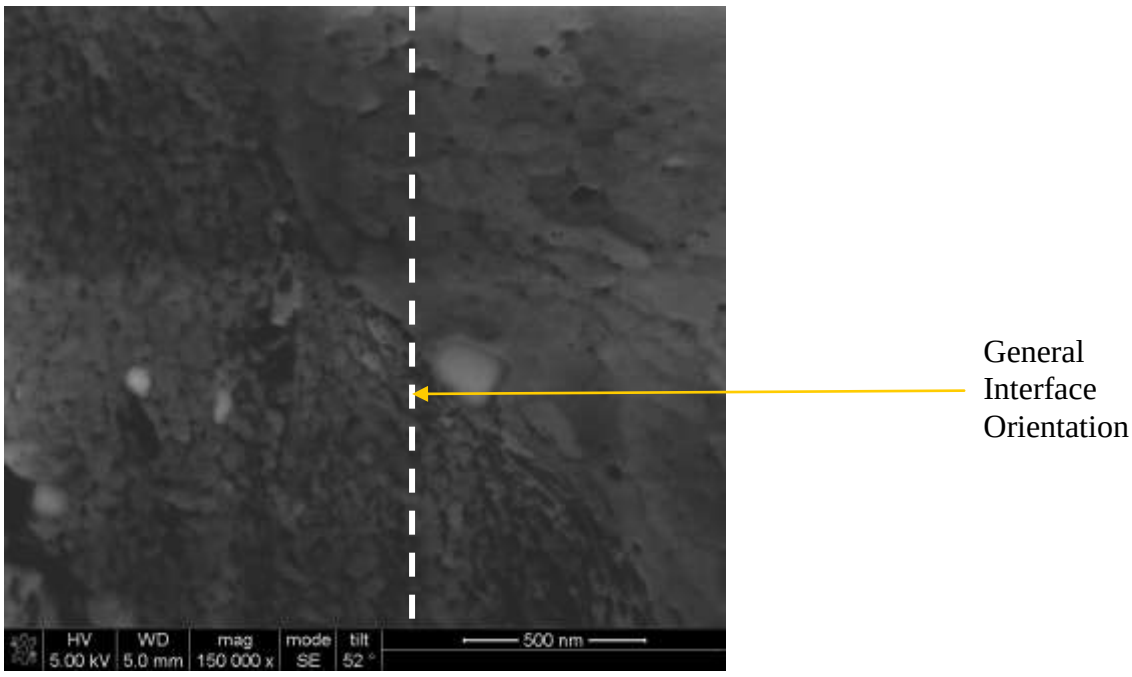

Figure 104 SEM electron micrograph of nano-grain transition region near the interface of a UC weld. These nano-grains were likely caused by the direct work of the sonotrode to this foils surface during the previous layers deposition.

8.3. New UC Micromechanics Model

Upon analysis of the research results it is apparent that there is indeed a significant decrease in sub-grain size within a UC processed additive manufacturing laminate, supporting the core of the author's hypothesis. Specifically, the previously reported connection between the stored energy of cold work and the Bauschinger Effect[101], and the resultant strong suggestion of an increased stored energy in UC samples, provides an initial correlation. This is shown through both an analysis of the decrease in sub-grain size (both due to significant sonotrode effects and more mild interlaminar interactions), and is supported by evidence of increased dislocation density and persistent slip bands. As a result, a new, more accurate description of the UC process is proposed. Of particular importance is the novel discovery and documentation of nano-grained regions that seem to primarily be caused by the direct sonotrode contact during each layer deposition and may influence subsequent layer depositions. The primary stages of this proposed updated micromechanics model is as follows.

1. During each foil layer deposition, the direct work caused between the sonotrode and the top of the foil to be deposited is significant and results in large amounts of plastic deformation, nano-grain formation and generally reduced sub-grain size. This heavily cold worked surface and resulting DAZ then becomes the substrate surface for subsequent layers.
2. Upon initial contact between the bottom of the new foil layer and the top of the previous deposition, the substrate asperities at the interface (residual effects of the prior sonotrode contact) experience massive amounts of plastic deformation during the initial cycles and collapse onto the substrate. This local geometry is shown in Figure 105.

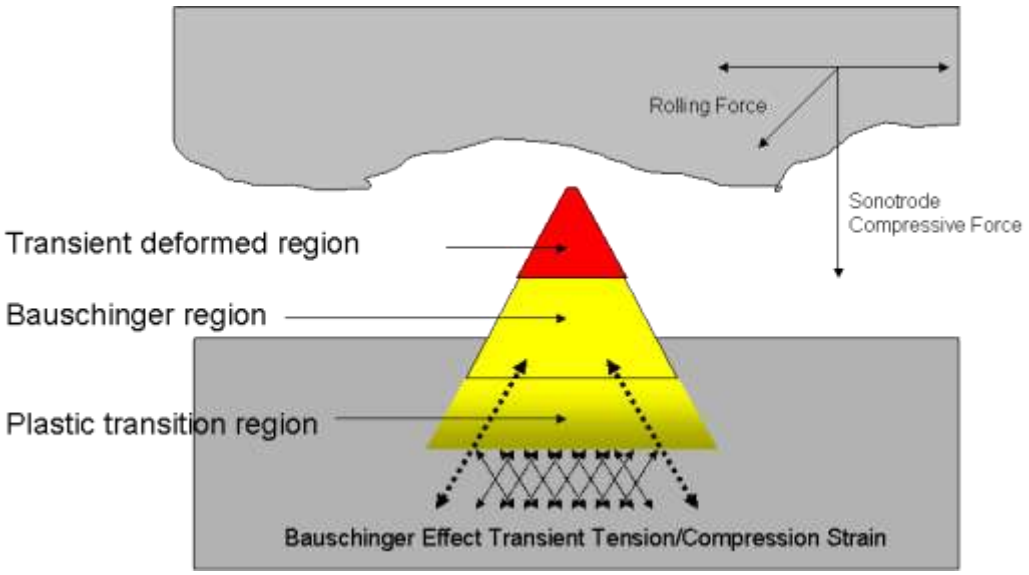

Figure 105: Multi-axial stress/strain state due to transient asperity geometry.

3. Oxide layers are minimally disrupted during this time and local adhesion is initiated. This adhesion subsequently establishes initial preferred persistent slip bands at and below the interface and a cyclic "tugging" within the material begins. Nano-grain colonies immediately form (or are re-activated if already present from the sonotrode work) at various high strain regions once the energy required to transport a dislocation through a sub-grain becomes less than that to bypass the newly formed nano-scale sub-grain boundary itself.
4. Particles such as manganese in the aluminium 3003 alloy family near the interface become high concentration areas of sub-grain refinement as a likely result of dense dislocation pile ups (Figure 106). Such "obstructions" may limit the depth of cyclic softening as the dislocations are not able to deeply penetrate the regions beneath them. Similar effects would be experienced in known difficult to weld alloys such as precipitation hardened 6000 series alloys[102].

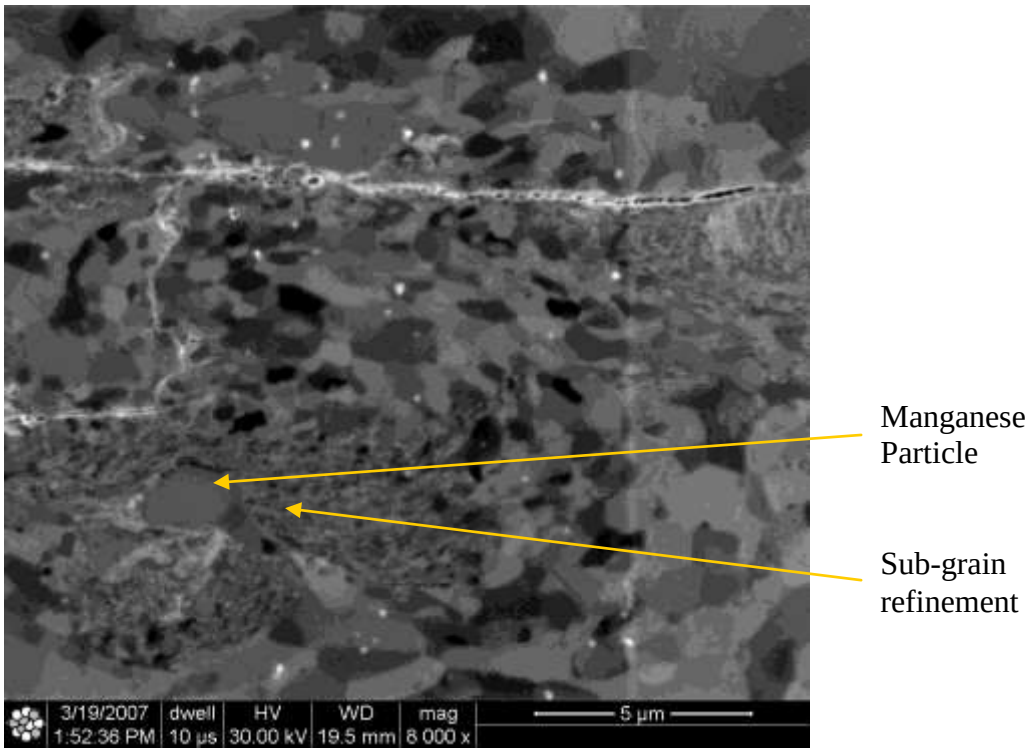

Figure 106 Ion beam induced secondary electron micrograph of 3003 T0 sample showing decrease in sub-grain size in and around Manganese particle.

5. Concurrent to this, the asperity geometry continues to change, resulting in the formation of new regions in which severe plastic deformation is occurring, promoting the rapid nucleation of nano-structured material and simultaneous morphology change of existing sub-grains, penetrating deep within the material. As the local material becomes more compliant through Bauschinger-like cyclic softening effects, this continual process of slip band development and nano-grain formation "hotspots" continue to expand.

Figure 107 shows a general representation of the proposed ability of the UC process to initiate and expand nano-grain formation and local softening and plastic deformation and represents a critical update to that proposed within the hypothesis. Note that the nano-grain formation is more pronounced on the top of the substrate foil due to both their likely pre-existence and their potential re-activation.

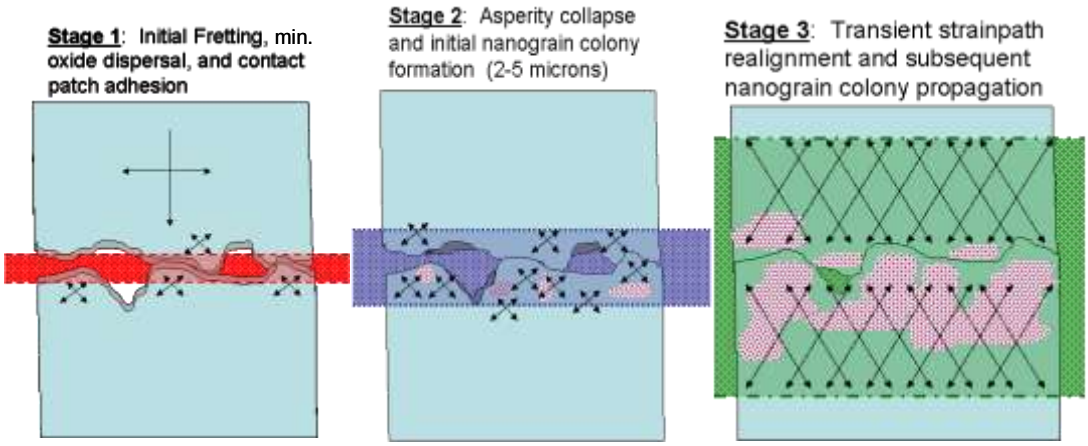

Figure 107: Three stage representation of UC induced nano-grain formation.

The suggested mechanism presented above, indicates why sonotrode surface texture and general consolidation parameters are so influential in the creation of a UC weld. The topology of surface asperities directly affects the tri-axial state of stress and strain at the interface and likely drives the amount of material that experiences severe plastic deformation. This plastic deformation is necessary for both the disruption of surface oxide barriers as well as to enable the propagation of regional softening necessary for the filling of interlaminar voids. Further, speed and amplitude significantly affect the total number of cycles a given volume of material experiences during the deposition stage, possibly creating a tension between additive manufacturing cycle time and interlaminar bond quality.

8.4. Langendecker and Bauschinger Correlation

It is most interesting to postulate that within the context of ultrasonic welding, the earlier noted “Langendecker Effect”, and the emphasised “Bauschinger Effect”, may in actuality be the same Effect. Langendecker observed the phenomena of ultrasonic (or cyclic) softening at a macro level while Bauschinger observed cyclic softening at a micro level. The author has now correlated, in the most introductory of ways, the

micro level Bauschinger and the macro level Langendecker effects, suggesting they are perhaps one and the same. Figure 108 shows common graphical representations of both of these effects side by side to help illustrate the point.

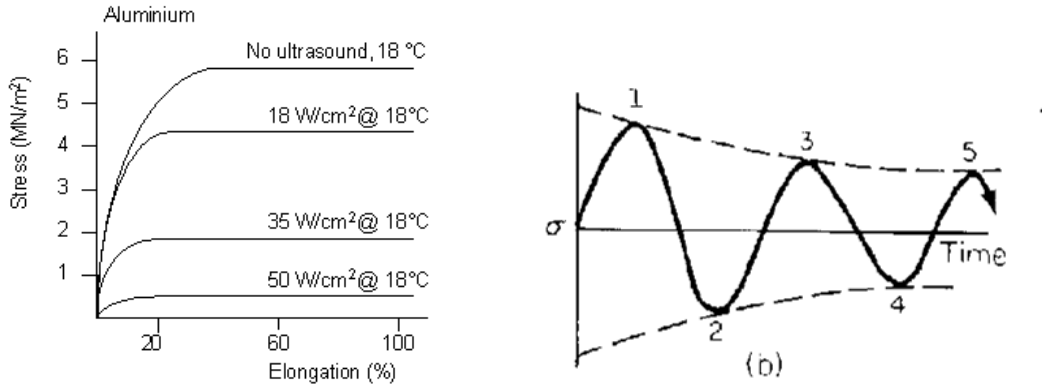

Figure 108 Langendecker Effect (left) showing an increase in material compliance under the influence of ultrasonic energy, Bauschinger Effect (right) showing similar increase.

Langendecker documented an increase in material compliance when a sample is under the influence of ultrasonics, which as has been discussed, is similar in nature to a high frequency cyclic strain process. Bauschinger showed how material compliance was increased during cyclic strain. Therefore, both Effects are in essence documenting a common phenomena related to cyclic strain in metals, one with a focus on ultrasonic frequencies, and the other generally focused on subsonic frequencies, however, with similar net results.

8.5. Summary of New Ultrasonic Joining Insights

The results of this research have shed significant clarification on many longstanding theories related to ultrasonic welding as it pertains to the UC process and the affect of ultrasonics on materials in general. While there is a great deal of additional study that will need to be conducted to fully validate certain elements of these results, the

following comments seek to provide some general concluding discussion and guidance for future researchers.

8.5.1. Interlaminar Amplitude Loss

The amplitude, or relative distance of motion at the interface is likely far less than the actual amplitude of the sonotrode itself. This can be considered an "amplitude efficiency" or "amplitude loss" value related to the amplitude transmission quality through the foil. Clearly this figure is driven by many factors but the contact mechanics and resultant slip between the sonotrode and the top of the foil are likely the key drivers. The challenge for UC practitioners to increase the amplitude efficiency relates to the negative effects of using rough, higher coupling sonotrode textures that may lead to greater interlaminar void volumes.

8.5.2. Surface Oxide Persistence

The idea of ultrasonic welding, at least in the case of UC, breaking up and displacing surface oxides leading to direct metal to metal contact is shown to be largely inaccurate for the material in this study. Whether this is due to the pre-hardening of the substrate surface through the sonotrode cold-work on the prior layer (and subsequent resistance to bonding), lack of friction/adhesion within the interlaminar region, or whether simply a matter of low amplitude transmission to the interface is unknown. The author suggests that the cause is most likely a combination of the latter two.

8.5.3. Effect of Interlaminar Texture

Where texture geometry exists that encourages significant interlaminar contact stresses and subsequent adhesion, the UBE appears to flourish. This probably occurs through massive amounts of near instantaneous dislocation propagation and localized softening that once initiated, rapidly expands. This would potentially explain the phenomena related to the encasing of fibres as the contact area and contact stress within the interlaminar region would be quite high in these cases as the softer matrix material quickly expands its area of contact with the much harder fibre element. It may also explain the difficulty in increasing fibre density due to a general reduction in surface area that would be in direct contact within the system (ie. the new foil would have a low contact area as it would be touching numerous hard fibre peaks only).

While contact efficiency seems to progress well in the case of soft materials in contact with harder materials in a UC laminate, when all of the layers are the same material the driving factor appears to be the mating texture. Specifically, rough to rough textures seem to initiate the highest degree of plastic flow within a UC bond. Thus, the effect of the transfer of the sonotrode texture to each deposited foil rises to a position of special significance for most UC applications. Recent studies carried out by Solidica, Inc.[31] show that this effect is highly influenced by the material being deposited and thus difficult to predict for different material systems. In these experiments, the surface transfer was shown to be drastically different when different foil materials were used as shown in Figure 109. For example, the sonotrode transfers nearly 100% of its surface texture to aluminium as aluminium's modulus and yield strength are very low as compared to the relatively hard titanium 6-4 sonotrode material. Conversely, when a hard titanium foil is being deposited by the same sonotrode, it transfers very little of its texture to the foil.

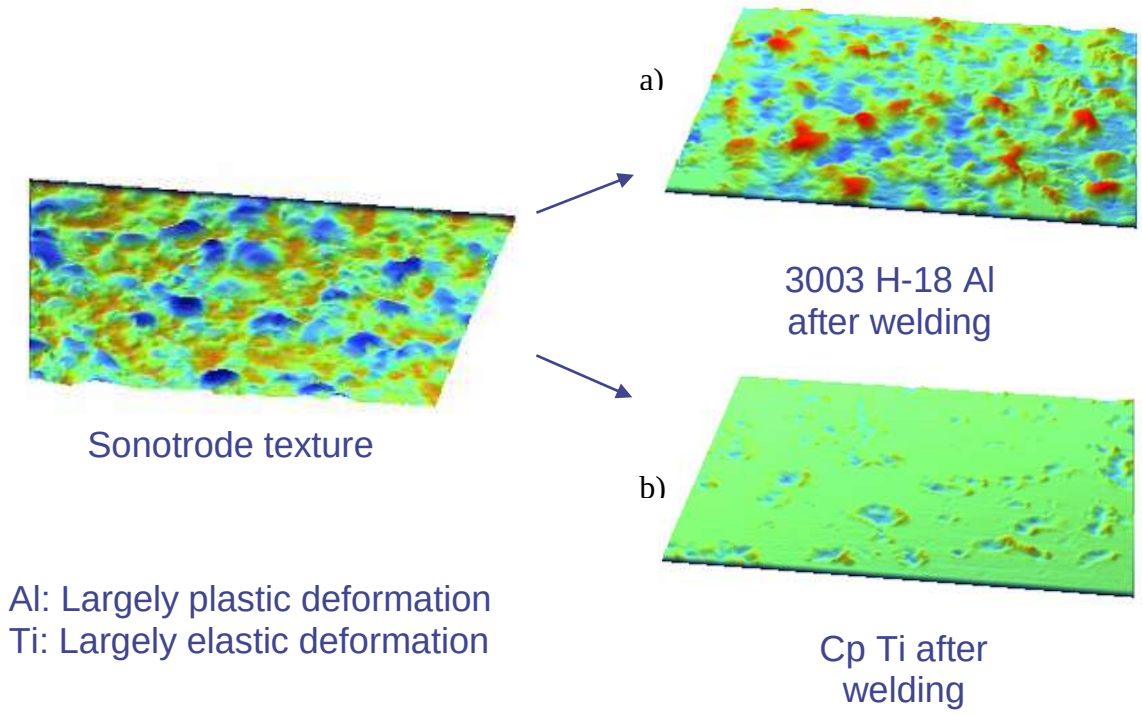

Figure 109 Three dimensional scans of the residual texture on deposited foil (right) following the transfer of the sonotrode texture to a) aluminium 3003 H-18 foil and b) commercially pure titanium foil.[31]

Care must be taken with regard to sonotrode texture selection as it is possible to create such an imprint on the top of the foil that when subsequent layers are deposited there is insufficient contact. As has been discussed in this research a lack of contact results in the UBE being unable to activate and local softening, necessary to fill voids in the interlaminar region, does not progress. Figure 110 highlights this idea from one of the samples produced from the relatively course LE sonotrode from Section 7.1.4.

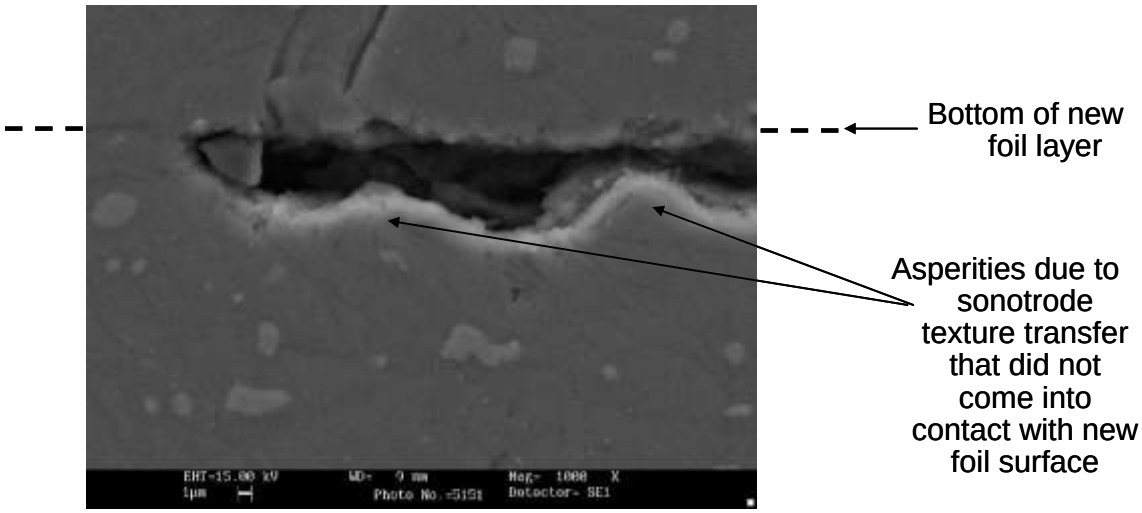

Figure 110 SEM electron micrograph of residual void in an aluminium laminate where there was not sufficient plastic flow to fill the defect left by the transferred texture of the LE sonotrode.

8.5.4. Solid State Process Clarification

There was no clear evidence of localized melting within the UC samples. For many years there have been two competing theories related to the idea of melting during ultrasonic welding. Many maintained that thermal effects defined the ultrasonic welding process and there was local recrystallisation, precipitation, phase transformation and diffusion[103]. Others countered that the process was truly solid state and that most of the work was done through a combination of deformation and shearing forces and not melting[104]. It would seem to be clear at this point that if melting were to occur at the interface that it would at least partially consume and recrystallise the small grains that have been documented to survive the process.

9. Conclusion

This research has presented microscopic evidence of dislocation propagation and sub-grain refinement in 3003-T0 aluminium undergoing high frequency fully reversed loading conditions during the Ultrasonic Consolidation process. Dual Beam Focused Ion Beam etching techniques and Transmission Electron Microscopy were used to characterize sub-grain morphology and dislocation structure in regions that were subjected to high levels of multi-axial ultrasonic micro-strain and resultant plastic deformation. This Deformation Affected Zone (DAZ) is characterized by regions of reduced sub-grain sizes that form a gradual transition into larger equiaxed, grains well below the interface.

The observed DAZ was highlighted by the presence of newly identified nano-grain regions, probably formed as a result of high intensity fields of ultrasonic cyclic work similar in nature to the Bauschinger Effect, which can be thought of as an Ultrasonic Bauschinger Effect (UBE). These nano-grained regions, or colonies, were observed in the material as far away from the interface as 10μm, emphasizing the significant penetration of the UBE. While much of the nano-grain formation is believed to occur as a result of the direct contact between the sonotrode and the top of each new deposited foil layer, these cold work effects may also influence the ability of subsequent layers to successfully bond. For example, the sonotrode induced fine grain structure may serve as a catalyst to achieving interlaminar plastic flow due to a reverse Hall Petch effect that would allow rapid dislocation transport via the re-activation of the pre-existing network of nano-grain boundaries.

The sonotrode additionally appears to contribute to the dislocation propagation and sub-grain refinement in the UC laminate. This occurs through the transference of the sonotrode texture onto the deposited foil that in turn influences the magnitude of

the laminate DAZ. In cases where the interface was generally rough, the sub-grain refinement and penetration of the DAZ was at a maximum. Such regions were also characterized by frequent nano-grain colony formations. In cases of relatively smooth interface profiles, there was far less sub-grain refinement and there were virtually no observed nano-grain regions present.

The results have also shed further light on several longstanding yet sparsely documented theories concerning ultrasonic welding in general. Paramount among these insights is that, at least in the case of the UC samples in this research, it was apparent that the oxide layer (long thought to be fractured and dispersed at the interface during the UC process) was in fact unbroken nearly throughout the interlaminar region. The persistence of the oxide is perhaps a key driver of the reduction in tensile strength of a UC fabricated part in the short transverse direction. One likely contributing factor to the oxides persistence may be due to the significant dissipation of energy between the sonotrode and the top of the foil, leading to low interlaminar amplitude efficiency. Eliminating the oxides through sonotrode texture engineering can now be more readily explored in light of the characterization methods and grain effect insights that have been presented in this research.

A cyclic softening, Bauschinger-like Effect, or UBE, does indeed appear to occur during the UC process. Understanding how to engineer and control the surface textures to maximize the UBE and the resultant DAZ holds the key to future advances in the field of UC. Such advances are needed to both improve UC laminate bond strengths necessary for future direct additive manufacturing applications; as well as to promote interlaminar plastic flow critical in exploiting the growing field of UC-based fibre embedding.

10. Future Research

Following is a discussion of future research proposed by the author. It is important to note that the field of ultrasonic welding in general, and UC in particular, is still arguably in its infancy from a fundamental understanding perspective.

1. Recent papers have shown that the Bauschinger Effect can be increased under increased strain rates and decreased temperature[105]. This would point to experimenting with higher amplitudes and decreased temperature of the UC system.
2. A previous low cycle, axial load fatigue study was carried out on 2S, 24S, 56S and 63S aluminium alloys[106]. The results showed that the Bauschinger effect in 2S commercial pure aluminium was small, yet became larger in its alloys. In precipitation hardening alloys, the Bauschinger effect changed, depending on the ageing conditions and was largest in the over-aged specimens. Thus future studies could explore the affect on UC bond quality when using precipitation hardened alloys and compare the stored energy and general sub-grain morphology differences with that of cold workable alloys. Additionally in this same study it was observed that the dislocation structure of cyclic strained pure aluminium is almost independent of the cycle number. This would imply that perhaps under the right conditions, the speed of the UC process could be significantly increased and should be explored further.
3. Future research could reproduce the experiments carried out during this work to other metals, specifically exploring the difference between hcp materials such as titanium with common bcc materials such as steel.
4. The experiments carried out within this work could be expanded to look at a much wider variety of interfacial textures and/or sonotrode textures. While it

is not desirable from a commercial standpoint to engineer the surface of each layer in an additive manufacturing process such as UC, the right interface texture may allow for faster rolling times while also promoting superior bond strength.

5. The basic experiments of this work could be repeated in conjunction with isolating and carefully modifying all key process variables including:
    a. Rolling speed
    b. Amplitude
    c. Power
    d. Sonotrode normal force
6. Finally, the role of dislocation formation and propagation within a UC weld provides additional clarification to earlier theories related to the idea of acoustic superposition. The acoustic superposition effect was described to be a general mechanism that occurs during the application of ultrasound to materials to reduce the load and friction of a system[107,15]. Dawson et al (1970) thought the effect of superposition accounted for the majority of cases in which a reduction in load or increased strain rate over the values predicted were observed. Eaves et al (1975) describe an experiment during tensile and bending tests where a significant reduction in the load required to bend polycrystalline samples of copper and steel was observed following the application of short pulses of ultrasonic vibration. While it is not specifically clear as to the magnitude of any influence of the acoustic superposition effect, work by Dawson et al which noted that acoustic energy was preferentially absorbed at dislocation sites would seem to point to the fact that any acoustic effect may have amplified and or accelerated the cyclic dislocation

propagation in the samples within this study. Now that the nature and extent of the dislocation propagation has become clarified within a UC weld, these earlier ideas could be revisited.

Special Insert – Johnson, K., Higginson, R., Dickens, P., Gupta, A., White, D., "Formation of Nano-grains During Biaxial High Frequency Fully Reversed Loading", ASM International, MS&T published paper, (2007)

References

[1] Mazumder, J., Choi, J., Nagarthnam, K., Koch, J., and Hetzner, D. "The direct metal deposition of H13 tool steel for 3-D components," JOM 49(5), (1997), p. 55

[2] Fessler, J.R., Merz, R., Nickel, A.H., Prinz, F.B., and Weiss, L.E., "Laser deposition of metals for shape deposition manufacturing," Proc. Solid Freeform Fabrication Symp., Austin, Tex., (1996), p. 117

[3] Doyle, T.E., "Shape melting technology," Natl. Conf. on Rapid Prototyping, Dayton, OH, (1990), p. 55

[4] Dickens, P. M., Pridham, M.S., Cobb, R. C., Gibson, I., and Dixon, G., "Rapid prototyping using 3-D welding," Proc. Solid Freeform Fabrication Symp., Austin, Tex., (1992), p. 280

[5] Dave, V. R., Matz, J.E., and Eagar, T.W., "Electron beam solid freeform fabrication of metal parts," Proc. Solid Freeform Fabrication Symp., Austin, Tex., (1995), p. 64

[6] Kovacevic, R., and Kmecko, I., "SFF based on controlled gas metal arc welding," Proc. NSF Manuf. Grantees Conf., Vancouver, Canada, (2000)

[7] Greaves, T., "Steel and Aluminum Laminate Tooling for Molding Applications," SME Publication #TP04PUB222, (2004)

[8] Manetsberger, K., Shen, J., Steinberger, J., "Method and device for selective laser sintering", US Patent 6858816, (2005)

[9] Bredt, J., Anderson, T. "Method of Three Dimensional Printing", US Patent 5902441, (1999)

[10] White, D. R., Object consolidation employing friction joining, United States Patent 6,457,629, October 1, (2002)

[11] Key to Metals Database, "Solid State Bonding," www.key-to-nonferrous.com, (2006)

[12] Beyer, R., "Historical sketches I. The acoustical contributions of Karl Rudolph," The Journal of the Acoustical Society of America, Vol. 104, Iss. 3, (1998), p. 1797

[13] Frederick, J., "Ultrasonic Engineering," John Wiley & Sons, Inc., London, (1965), p. 165

[14] Welding Handbook, 4th edition, Section 3, American Welding Society, New York, (1964)

[15] Eaves, A., "Review of the application of Ultrasonic vibration to deforming metals," Ultrasonic, Vol. 13, Iss. No.4, (1975), p. 162

[16] Langenecker, B., "Effects of Ultrasound on Deformation Characteristics of Metals," IEEE Transactions on Sonics and Ultrasonics, SU-13 (1966), No. 1

[17] Langenecker, B., "Ultrasonic Treatment of Specimens in the Electron Microscope," Review of scientific instruments, Vol. 37, (1966), p. 103

[18] Kovsh, S.V., Kotko, V.A., Polotskiy, I.G., Prokopenko, G.I., Trefilov, V.I., Firstov, S.A. "Effect of cyclic deformation on the dislocation structure and mechanical properties of molybdenum," Physics of Metals and Metallography, Vol. 35 (1973), p. 74

[19] Chevalier, J.L., Gibbons, D.F., Leonard, L., J "High Frequency Fatigue in Aluminum," Applied Physics Vol. 43, Iss. 1 (1972), p. 73

[20] Joshi, K., "The Formation of Ultrasonic Bonds Between Metals," Welding Journal, Vol. 50, No. 12, (1971), p. 840

[21] Happ, M. G., "Fracture and Recovery During the Creep of Commercially Pure Al," M.S. Dissertation, Dept. of Met., MIT (1956)

[22] Joshi, K. C., "Steady State Creep Behavior of High Purity Polycrystalline Lead," No. 62, Wash. State U. (1965)

[23] Hayes, G.A. and Shyne, J. C., "The Influence of Ultrasonic Energy on Kinetic Processes in Solids," IEEE Transactions on Sonics and Ultrasonics, Vol. 16, Iss. 2, (1969), p. 68

[24] Mason, W. P., "Physical Acoustics and the Properties of Solids," D. Van Nostrand Co., Princeton, N.J., (1958), p. 263

[25] Rhines, F. M., "Study of Changes Occurring in Metal Structure During Ultrasonic Welding," Summary Report, Met. Res. Lab., U. of Florida (1962), p. 82

[26] Krzanowski, J.E., "A transmission electron microscopy study of ultrasonic wire bonding", IEEE Transactions on Components, Hybrids, and Manufacturing Technology, Houston, TX, Vol. 13, Iss. 1, March (1990), p. 176

[27] Allameh, S.M., Mercer, C., Popoola, D., Soboyejo, W.O., "Microstructural Characterization of Ultrasonically Welded Aluminum", Journal of Engineering Materials and Technology, Vol. 127, No. 1, January, (2005), p. 65

[28] Brodyanski, A., Born, C., Kopnarski, M., "Nm-scale resolution studies of the bond interface between ultrasonically welded Al-alloys by an analytical TEM: a path to comprehend bonding phenomena?" Applied Surface Science, Vol. 252, Iss. 1, (2005), p. 94

[29] Solidica, Inc., "Internal Report: Support Material Phase 1 Final Report", (2005)

[30] Solidica, Inc., "RPG Final Report to US Navy", confidential customer report, (2005)

[31] Solidica, Inc., "Effects of Ti/Al Laminates", confidential customer report, (2006)

[32] Kong, C.Y., Soar, R.C., Dickens, P.M., "Characterisation of aluminium alloy 6061 for the ultrasonic consolidation process," Materials Science and Engineering A363 (2003) p. 99

[33] Kong, C.Y., Soar, R.C., Dickens, P.M., "Optimum process parameters for ultrasonic consolidation of 3003 aluminium," Journal of Materials Processing Technology 146 (2004) p. 181

[34] Daniels, H., "Ultrasonic Welding," Ultrasonics, Vol. 3, Iss. 4, (1965), p. 190

[35] Dieter, G. E., "Mechanical Metallurgy," McGraw-Hill, New York, (1986), ISBN 0070168938, p. 77

[36] Berk-Tek Optical Fiber Cable Specification for 62.5/125 Fiber, Fuquay-Varina, NC, USA

[37] Solidica, Inc., "Internal Report: Metal Matrix Composite Final Report", (2005)

[38] Kong, C.Y., Soar, R.C., Dickens, P.M., "Ultrasonic consolidation for embedding SMA fibres within aluminium matrices," Composite Structures 66 (2004) p. 421

[39] Solidica, Inc., "Internal Report: Final Report to US Department of Energy", (2006)

[40] Rabinowicz, E. "Friction and Wear of Materials," Second Edition, John Wiley and Sons, New York New York, (1995), ISBN 0471830844

[41] Hansson, I., Tholen, A., "Plasticity due to superimposed macrosonic and static strains," Ultrasonics, Vol. 16, Iss. 3, (1978), p. 57

[42] Cottrell, A.H., "Dislocations and Plastic Flow in Crystals", Oxford, Clarendon Press, (1953)

[43] Gelder, J., "Animations for Introductory Chemistry", PhD. Thesis, Oklahoma State University, (1994)

[44] Warren, B. E. and Warekois, E. P., "Stacking faults in cold worked alpha brass", Acta Metallurgica, Vol. 3, (1955), p. 473

[45] Murr, L. E., "Interfacial Phenomena in Metals and Alloys," Addison-Wesley, Reading, Mass., (1975), ISBN 0201048841

[46] Weertman, J.R., "Mechanical Behavior of Nanocrystalline Metals: processing, properties and applications", Kock, C.C. (ed.), William Andrews Publishing, Norwich, NY, (2002), ISBN 0815514514, p. 397

[47] Masumura, R. A., Acta Mater. "Yield stress of fine grained materials," Scripta Materialia, Vol. 46, Iss. 13, (1998), p. 4527

[48] Solidica, Inc., "Internal Report: Effect of nanograined material on UC fabrication", (2005)

[49] Bannantine, J.A., Comer, J.J., Handrock, J.L., "Fundamentals of Metal Fatigue Analysis," Prentice Hall, Englewood Cliffs, NJ, (1990), ISBN 013340191X, p. 273

[50] Rolfe, S.T., Haak, R.P., Gross, J.H., "Effect of State-of-Stress and Yield Criterion of the Bauschinger Effect," Trans. American Society of Mechanical Engineers, Vol. 90, No. 3 (1968), p. 403

[51] Polakowski, N.H., "Bauschinger effect and multiaxial yield behavior of stress-reversed mild steel", American Society of Test. Mater. Proc., Vol. 63, (1963), p. 535

[52] Edwards, E. H., Washburn, J., and Parker, E. R. Trans., "The stress-strain characteristics of 111 oriented aluminum single crystals deformed in torsion", AIME, Vol. 197, (1953), p. 1526

[53] Stoltz, R.E. and Pelloux, R.M., "The Bauschinger Effect in Precipitation Strengthened Aluminum Alloys," Metall Trans A **7** (1976), p. 1295

[54] Sowerby, R., Uko, D.K. and Tomita, Y., "A Review of Certain Aspects of the Bauschingher Effect in Metals," Materials Science Engineering, Vol. 41, No. 1, (1979), p. 43

[55] Bate, P.S. and Wilson, D.V. "Analysis of the Bauschinger Effect," Acta Metall**,** Vol. 34, No. 6 (1986), p. 1097

[56] Hasegawa, T., Yakou, T. and Kocks, U.F., "Forward and reverse rearrangements of dislocations in tangled walls," Material Science and Engineering, Vol. 81 (1986), p. 189

[57] Pedersen, O.B., Brown, L.M. and Stobbs, W.M., "The Bauschinger Effect in Copper," Acta Metallurgica, Vol. 29, Iss. 11 (1981), p. 1843

[58] Margolin, H., Hazaveh, F. and Yaguchi, H., "The Grain Boundary Contribution to the Bauschinger Effect," Scripta Metallurgica, Vol. 12, Iss. 12 (1978), p. 1141

[59] Ono, N., Tsuchikawa, T. and Nishimura, S., Intergranular Constraint and the Bauschinger Effect," Material Science and Engineering, Vol. 59, Iss. 2 (1983), p. 223

[60] Aran, A., Demirkol, M. and Karabulut, A., "Bauschinger Effect in Precipitation-Strengthened Aluminium Alloy 2024," Materials Science and Engineering, Vol. 89, (1987), p. l35

[61] Atkinson, J.D., Brown, L.M. and Stobbs, W.M., "Work-hardening of Copper-silica EM Dash 4. The Bauschinger Effect and Plastic Relaxation," Philos Mag, Vol. 30, Iss. 6, (1974), p. 1247

[62] Brown, L.M. and Stobbs, W.M., "The work-hardening of copper-silica. I. A model based on internal stresses, with no plastic relaxation," Philosophical Magazine, Vol. 23, Iss. 185, (1971), p. 1185

[63] Rauch, E.F., Gracio, J.J., Barlat, F., Lopes, A.B, Ferreira Duarte, J., "Hardening behavior and structural evolution upon strain reversal of aluminum alloys," Scripta Materialia, Vol. 46, Iss. 12, (2002), p. 881

[64] Barlat, F., Ferreira Duarte, J.M., Gracio, J.J., Lopes, A.B. and Rauch, E.F., "Plastic flow for non-monotonic loading conditions of an aluminum alloy sheet sample," *Int. J. Plasticity* 19 (2003), p. 1215

[65] Orowan, E., "Internal Stresses and Fatigue in Metals," Elsevier Publishing Company, New York, (1959)

[66] Espinosa, H.D., Panico, M., Berbenni, S., Schwarz, K.W., "Discrete dislocation dynamics simulations to interpret plasticity size and surface effects in freestanding FCC thin films," International Journal of Plasticity, Vol. 22, (2006), p. 2091

[67] Correa, C.S., Aguilar, M.T.P., Monteiro, W.A., Cetlin, P. R., "Superficial and structural aspects of the cyclic strain softening in 6063 aluminum alloy bars," Journal of Materials Processing Technology, Vol. 142, Iss. 2, (2003), p. 362

[68] J. R. Cowan, R.L. Higginson, W.B. Hutchinson, P.S. Bate, Materials Science and Technology, Iss. 11, (1996), p. 1104

[69] C.M. Sellars, Q. Zhu, Proceedings of the Twentieth Riso International Symposium on Materials Science, Deformation-induced Microstructures: Analysis and Relation to Properties, Riso National Laboratory, Roskilde, Denmark, (1999), p. 167

[70] Mollica, F., Rajagopal, K., Srinivasa, A., "The inelastic behavior of metals subject to loading reversal", International Journal of Plasticity, 17, (2001), p. 1119

[71] Rhines, F. M., "Study of Changes Occurring in Metal Structure During Ultrasonic Welding," Summary Report TP82—162, Met. Res. Lab., U. of Florida (1962)

[72] Frisch, J., Pfaelzer, P.F. Chang, U.I., "Ultrasonic welding of metals in vacuum," 11th MTDR Conference held at the University of Manchester, 14-18 Sept., (1970), Pergamon Press, (1970)

[73] Weare N.E., Antonevich JN. "Fundamental studies of ultrasonic welding," Welding Journal, Vol. 39, Iss. 8, (1960), p. 331s

[74] Bowden, F.D. "A review of the friction of solids," Wear, Vol. 1, Iss. 4, (1957), p. 333

[75] Higginson, R.L., Pinna, C., Beynon, J.H., Wynne, B.P., "Effect of roll pass schedule on through thickness texture development in Al-Mn alloy," Materials Science and Technology, Vol. 19, (2003), p. 477

[76] Higginson, R.L., Sellars, C.M., Materials Science and Technology," The effect of strain path reversal during hot rolling on austenitic stainless steel", (2002), p. 338

[77] Donald K. Cohen, Paul J. Caber, Chris P. Brophy, Rough Surface Profiler and Method. United States Patent, 5,133,601, Jul 28, (1992)

[78] Higginson, R.L., Sellars, C.M., "Worked Examples in Quantitative Metallography", Maney Publishing, ISBN 1-902653-80-7, (2003), p. 36

[79] Riben, A.R., Sherman, S.l., Land, W. V., Geisler, R., "Microbonds for hybrid microcircuits," Physicas of Failure in Electronics, Vol. 5, (1967), p. 534

[80] Petch, N.J., "The cleavage strength of polycrystals", J. Iron Steel Institute, 174, (1953), p. 25

[81] Hall, E. O., "The deformation and ageing of mild steel: III Discussion of Results," Processing Physics Society B, 64, (1951), p. 747

[82] Schiotz, J., Jacobsen, K.W., "A maximum in the strength of nanocrystalline copper." Science, 301 (2003), p. 1357

[83] Flood, G., "Ultrasonic energy welds copper to aluminium", Welding Journal ; Vol. 76 ; Iss. 1 ; (1997), p. 43

[84] Siegert, K., Ulmer, J., "Superimposing ultrasonic waves on the dies in tube and wire drawing", Transactions of ASME: Journal of Engineering Materials and Technology, Vol. 123 (2001), p. 517

[85] Jimma, T., Kasuga, Y., Iwaki, N., Miyazawa, O., Mori, E., Ito, K., "An application of ultrasonic vibration to the deep drawing process", Journal of Material Processing Technology, Vol. 80-81 (1998), p. 406

[86] Kristoffy, I., "Metal forming with vibrated tools", Transactions of ASME: Journal of Engineering for Industry, (1969), p. 1168

[87] Siegert, K., Ulmer, J., "Influencing the friction in metal forming process by superimposing ultrasonic waves", Annals of CIRP**,** Vol. 50, (2001), p. 195

[88] Onikura, H., Ohnishi, O., Feng, J., Kanda, T., Morita, T., "Effect of ultrasonic vibration on machining accuracy in microdrilling", Journal of JSPE, Vol. 62, Iss. 5, (1996), p. 676

[89] Takeyama, H., Kato, S., "Burrless drilling by means of ultrasonic vibrations", Annals of CIRP**,** Vol. 40, Iss. 1, (1991), p. 83

[90] Egashira, K., Mizutani, K., "Ultrasonic vibration drilling of microholes in glass", Annals of CIRP, Vol. 51, Iss. 1, (2002), p. 339

[91] Webber, H., Herberger, J., Pilz, R., "Turning of glass ceramics with ultrasonically vibrated tools", Annals of CIRP**,** Vol. 33, Iss. 1, (1984), p. 85

[92] Takeyama, H., Iijima, N., "Machinability of glass fibre reinforced plastics and application of ultrasonic machining", Annals of CIRP**,** Vol. 37, Iss. 1, (1988), p. 93

[93] Kim, D.U., Lee, E.S., "A study of ultrasonic vibration cutting of carbon fibre reinforced plastics", Journal of Material Processing Technology**,** Vol. 43**,** (1994), p. 259

[94] Schey, A.J.. "Tribology in metalworking; friction, lubrication and wear", American Society for Metals, Metals Park, OH, (1984), ISBN 0871701553, p. 93

[95] Kumar, V. C., Hutchings, I. M., "Reduction of the sliding friction of metals by the application of longitudinal or transverse ultrasonic vibration", Tribology International Vol. 37, Iss. 10, (2004), p. 833

[96] Storck H, Littmann W, Wallaschek J, Mracek M., "The effect of friction reduction in presence of ultrasonic vibrations and its relevance to traveling wave ultrasonic motors" Heinz Nixdorf Institut, University of Paderborn, Germany, Iss. 40, (2002), p. 379

[97] Aguilar, M., Correa, E., Monteiro, W., Cetlin, P., "The effect of cyclic torsion on the dislocation structure of drawn mild steel," Materials Research, Vol. 9, No. 3, (2006)

[98] Bateni, M., "The Effect of Grain Orientation on Micro Frictional of Medium Carbon Steel," Materials Science Forum, Vol. 495-497, (2005), p. 203

[99] Buckley, D.H. “Surface Effects In Adhesion, Friction, Wear, and Lubrication” Elsevier Scientific Publication, Amsterdam, The Netherlands, (1981), ISBN 9513858499

[100] Buckley, D.H. “Friction, Wear, and Lubrication in Vacuum”, NASA SP-277, (1970)

[101] Benzerga, A.A., Brechet, Y., Needleman, A., Van der Giessen, E., “The stored energy of cold work: Predictions from discrete dislocation plasticity”, Acta Materialia 53 (2005), p. 4765

[102] Solidica, Inc., “Office of Naval Research Final Report”, (2005)

[103] Tsujino, S. Ihara, Y. Harada, K. Kasahara, Sakamaki, N. “Characteristics of coated copper wire specimens using high frequency ultrasonic complex vibration welding equipments”, Ultrasonics, Vol. 42, Iss. 1-9, (2004), p.121

[104] Harthoorn, J. L., “Ultrasonic Metal Welding,” Ph.D. Dissertation, Technical College Eindhoven, Netherlands, (1978)

[105] Thakur, A., Vecchio, K., Nemat-Nasser, S., “Bauschinger Effect in Haynes 230 Alloy: Influence of Strain Rate and Temperature”, Metallurgical Transaction A, Vol. 27A, No. 7, (1996), p. 1739

[106] Horiuchi, R., Saito, S., Kishi, T., “Bulletin of the Institute of Space and Aeronautical Science, University of Tokyo,” Japan Aerospace Exploration Agency, Vol.6, No.3B, ISSN:05638100, (1970) p. 748

[107] Dawson, G.R., Winsper, C.E., Sansome, D.H., “Application of High and Low Frequency Oscillations to the Plastic Deformation of Metals – A Complete Appraisal of the Development and Potential,” Metal Forming, Vol. 37, No. 9, (1970), p. 254